STUDY OF STRUCTURAL, ELECTRICAL AND MAGNETOELECTRIC PROPERTIES OF POLYCRYSTALLINE $Bi_{1-x}Gd_xFe_{0.9}Cr_{0.1}O_3$

A dissertation submitted to the Department of Physics, Bangladesh University of Engineering and Technology, Dhaka in fulfillment of the requirement for the degree of Master of Science (M. Sc.) in physics

Submitted by

MD. AZMAL HOSSAIN

Student No. : 1014142508F

Session : October-2014

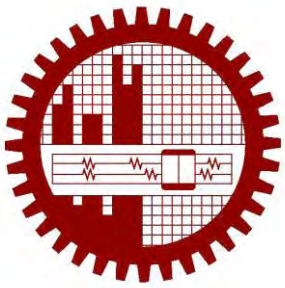

DEPARTMENT OF PHYSICS

BANGLADESH UNIVERSITY OF ENGINEERING & TECHNOLOGY

DHAKA-1000, BANGLADESH

CANDIDATE'S DECLARATION

It is hereby declared that this thesis or any part of it has not been submitted elsewhere for the award of any degree or diploma.

Md. Azmal Hossain

BANGLADESH UNIVERSITY OF ENGINEERING & TECHNOLOGY

DEPARTMENT OF PHYSICS, DHAKA 1000, BANGLADESH

CERTIFICATION OF THESIS

The thesis titled **"STUDY OF STRUCTURAL, ELECTRICAL AND MAGNETOELECTRIC PROPERTIES OF POLYCRYSTALLINE $Bi_{1-x}Gd_xFe_{0.9}Cr_{0.1}O_3$"** submitted by **MD. AZMAL HOSSAIN,** Roll No.: 1014142508F, Session: October 2014, has been accepted as satisfactory in partial fulfillment of the requirement for the degree of **Master of Science (M. Sc.) in Physics** on **31 August, 2016.**

BOARD OF EXAMINERS

1. (A. Hossain.) Chairman
   Dr. A. K. M. Akther Hossain (Supervisor)
   Professor, Department of Physics,
   BUET, Dhaka-1000, Bangladesh

2. (F. Khanam.) Member
   Mrs. Fahima Khanam (Ex- Officio)
   Head and Professor, Department of Physics,
   BUET, Dhaka-1000, Bangladesh

3. ( ) Member
   Dr. Md. Abu Hashan Bhuiyan
   Professor, Department of Physics,
   BUET, Dhaka-1000, Bangladesh.

4. ( ) Member
   Dr. Khandker Sadat Hossain (External)
   Professor, Department of Physics,
   University of Dhaka, Dhaka-1000, Bangladesh.

Dedicated To

My

Beloved Parents

CONTENTS

CHAPTER 3

SAMPLE PREPARATION AND EXPERIMENTAL TECHNIQUE

CHAPTER 4

RESULTS AND DISCUSSION

CHAPTER 5

CONCLUSIONS

List of Figures

List of Tables

Abbreviation of Symbols and Terms

ME	Magnetoelectric
BFO	$BiFeO_3$
XRD	X-ray Diffraction
FESEM	Field Emission Scanning Electron Microscope
EDX	Energy dispersive X-ray spectroscopy
$'$	Dielectric constant
$_0$	Permitivity in free space
$\tan\delta_E$	Dielectric loss
Z^*	Complex impedance
Z'	Real part of complex impedance
Z''	Imaginary part of complex impedance
σ_{ac}	AC conductivity
σ_{dc}	DC conductivity
M^*	Complex electric modulus
M'	Real part of modulus
M''	Imaginary part of modulus
$_{ME}$	Magnetoelectric coefficient
t	Tolerance factor
$\overline{E}$	Electric field
$\overline{P}$	Polarization
C	Capacitance with material
C_0	Capacitance in free space
D	Thickness
ω	Angular frequency

M	Magnetization
H	Magnetic field
M_r	Remanent magnetization
M_s	Saturation magnetization
H_c	Coercivity
μ_i^*	Complex initial permeability
$\mu_i^{'}$	Real part of complex initial permeability
$\mu_i^{''}$	Imaginary part of complex initial permeability
$\tan\delta_M$	Magnetic loss
ρ_x	X-ray density
ρ_B	Bulk density

ACKNOWLEDGEMENTS

First I would like to express my special prayer to almighty ALLAH, who has given me immeasurable opportunity and patience to complete thesis work.

With great pleasure, I wish to express my regards, profound gratitude and deep appreciation to my reverend teacher and supervisor ***Dr. A. K. M. Akther Hossain****, Professor, Department of Physics, Bangladesh University of Engineering and Technology (BUET), Dhaka, Bangladesh for his indispensable guidance, thoughtful suggestions, constant encouragement and affectionate surveillance through the entire period of my research work.*

I am extremely grateful to my respected teacher ***Prof. Fahima Khanam****, Head, Department of Physics, BUET, for providing the research facilities in the Department during the research work.*

I would like to express my gratitude to ***Prof. Dr. Md. Abu Hashan Bhuiyan, Prof. Dr. Jiban Podder, Prof. Dr. Md. Feroz Alam Khan, Prof. Dr. Md. Mostak Hossain, Prof. Dr. Afia Begum, Prof. Dr. Md. Forhad Mina, Prof. Dr. Md. Rafi Uddin, Dr. Nasreen Akter, Dr. Mohammed Abdul Basith,*** *and all other teachers of the Department of Physics, for their cooperation. Special thanks to* ***Dr. Mohammad Abu Sayem Karal*** *for valuable suggestions to complete my thesis.*

I would like to thank ***Mr. Mehedi Hasan Rizvi****, Assistant Professor, Department of Glass and Ceramic Engineering, BUET, Dhaka, Bangladesh, for giving me all sorts of supports to measure the X-Ray Diffraction analysis of my various samples.*

I am grateful to ***Dr. Md. Belal Hossen, Dr. Sajal Chandra Mazumdar, Dr. Md. Julhash Miah, Mr. Md. Kamrul Haque Bhuiyan, Mr. Kazi Khirul Kabir, Mr. Bablu Chandra Das, Mr. Md. Abdulla-Al-Momin*** *for their sincere cooperation and discussion. I want to express thanks to* ***Dr. Mohammed Nazrul Islam Khan****, PSO, Material Science Division, AECD, for his valuable advice. I also greatfully acknowledge the cooperation of all*

other researchers of Ph.D., M.Phil. and M. Sc. in the laboratory for their constant support in many ways.

I would like to acknowledge the help of the different staff members of the Department of Physics, BUET, Dhaka and any one in connection with my research.

I would acknowledge the CASR, BUET to provide financial support for this research work.

Finally, I would like to thank my brothers ***Md. Aynul Haque and Noor Mohammad*** *whose continuous inspiration, support and encouragement gave me the strength to carry on my research.*

The Author

Md. Azmal Hossain

ABSTRACT

In this research, polycrystalline $Bi_{1-x}Gd_xFe_{0.9}Cr_{0.1}O_3$ (x = 0.00, 0.05, 0.10, 0.15 and 0.20) ceramics have been synthesized by standard solid state reaction technique. The structural, microstructural, electrical, magnetic and magnetoelectric properties of various $Bi_{1-x}Gd_xFe_{0.9}Cr_{0.1}O_3$ have been studied. X-ray diffraction analysis confirmed the structural transformation from rhombohedral to orthorhombic for x = 0.10. Microstructural and quantitative analysis were performed by Field Emission Scanning Electron Microscope and Energy Dispersive X-ray spectroscopy respectively. Average grain size was found decreasing with increasing Gd content due to grain growth suppression by Gd and it was found increasing with sintering temperature. At lower frequency, dielectric constant showed dispersive behavior due to space charge polarization. Dielectric constant increased with increasing Gd content. From the impedance and AC conductivity measurements it is observed that the value of impedance decreases and AC conductivity increases with increasing frequency because of hopping of charge carriers. Impedance spectroscopy also showed that both grain and grain boundary contribution are present in the conduction mechanism and resistance is found decreasing with Gd content. The conduction phenomenon also understood from the electric modulus (M′) vs frequency graph. M′ approaches to zero in the lower frequency region and a continuous dispersion on increasing frequency may be contributed to the conduction phenomenon due to short range mobility of charge carriers. The real part of complex initial permeability (μ_i') of the samples increased with sintering temperature because of uniform grain growth. Improved magnetization was found in Gd doped $Bi_{1-x}Gd_xFe_{0.9}Cr_{0.1}O_3$ due to magnetic property of Gd. Magnetoelectric coefficient was observed to improve with Gd doping in $Bi_{1-x}Gd_xFe_{0.9}Cr_{0.}1O_3$ compositions and it also increased with increasing sintering temperature.

CHAPTER 1

INTRODUCTION AND REVIEW WORKS

1.1 Introduction

As society evolves, the need for new technology increases more rapidly than ever. So that information technology is one of the cornerstones of this evolution having seen an exponential improvement during the last half century. In recent years, the need for ever decreasing sizes of transistors and other necessary components has intensified the focus of other ways of increasing computer performance without purely reducing structural dimensions. One different way of meeting this challenge has been by using multiferroics instead of single-ferroic materials in the process. Multiferroic materials posses two or more ferroic orders simultaneously [1]. The term multiferroic was first used by Hans Schmid in 1994 [2]. Although current technologies incorporate both ferro-electric and -magnetic materials and have been for a long time, no known materials display these properties at room temperature [3]. Perovskite and related compounds are widely investigated because of their multiferroic, photocatalytic and magnetic properties which are useful for applications in capacitors, nonvolatile memory, nonlinear optics and photoelectrochemical cells [4]. One of the most promising multiferroic material is the perovskite bismuth ferrite (BFO), as it shows the coexistence of both ferroelectricity and antiferromagnetic order. But due to volatilization of bismuth and other impurities it is difficult to use in practical application [5]. Pure bismuth ferrite may be modified in several ways. An important route to modify its properties is to substitute bismuth with another cation, such as a rare-earth metal. Samarium is a rare-earth metal which differs from bismuth with its much smaller ionic radii [6].They tried to address the conductivity problem by doping other ions into both the A and B sites of the lattice, but no practical devices were obtained. Reviews of the general study of magnetoelectricity

appeared by Schmid in 1994 [2]. BFO is perhaps the only material that is both magnetic and a strong ferroelectric at room temperature [7]. As a result, it has an impact on the field of multiferroics that is comparable to that of yttrium barium copper oxide (YBCO) on superconductors, with hundreds of publications devoted to it in the past few years. In this review, the researcher tries to summarize both the basic physics and unresolved aspects of BFO, and device applications, which centered around on spintronics and memory devices that can be addressed both electrically and magnetically [8].

The ongoing search for a better way to control the phenomena of multiferroicity and the great interest in multiferroic materials is attributed to the exciting and potentially groundbreaking impact this can have on several technology aspects. Especially the ability to maintain magnetization and a dielectric polarization which can be modulated and activated by an electric field and a magnetic field, respectively, makes multiferroic materials potential in several different applications [9].

1.2 Motivation

Multiferroic have recently drawn significant attention due to their huge technological importance [10]. Natural single phase multiferroics are rare, and their ME responses are either relatively weak or occurs at temperature too low for practical applications. BFO is the most widely studied multiferroic material. But preparation of pure BFO is a challenge due to the formation of different impurity phases [11, 12]. The ferroelectricity in BFO is considered to originate primarily from displacements of the Bi^{3+} ions due to the lone $6S^2$ pair. The magnetic ordering of BFO is G-type antiferromagnetic, having a spiral modulated spin structure (SMSS) with an incommensurate long-wavelength period of 62 nm [13]. This spiral spin structure cancels the macroscopic magnetization and prevents the observation of the linear magnetoelectric effect [14]. These problems ultimately limit the use of BFO in functional applications. Many current investigations seek to suppress the spiral spin structure

in an effort to release the inherent magnetization of this canted antiferromagnet and consequently to improve its multiferroic properties. One of the easiest ways to destroy the spiral spin structure in BFO is the structural modifications or deformations introduced by cation substitutions or doping. Therefore, to perturb the spiral spin structure and to improve the multiferroic properties of BFO, investigations were carried out substituting Bi by rare-earth ions [15, 16] or alkaline-earth ions [17] and also substituting Fe by transition metal ions [18, 19]. Recent investigations also demonstrated that co-doping at Bi- and Fe-sites of BFO by ions such as La and Mn [20], La and Ti [21], Gd and Co [22], Ba and Mn [23], Dy and Cr [24] etc., respectively can significantly improve multiferroic properties of BFO for various applications. In this investigation, we have preferred this co-doping approach and have performed simultaneous minor substitution of Bi and Fe in BFO by ions such as Gd and Cr, respectively to observe their multiferroic properties. The partial substitution of Bi^{3+} with ions having the smaller ionic radius can suppress effectively the spiral spin structure of BFO [25], therefore, we have chosen Gd (ionic radius 0.938 Å) in place of Bi (ionic radius 1.03 Å) as a doping element. Also many investigations were done with Cr doping at Fe site in BFO ceramics [26, 27]. But to the best of our knowledge no reports with Gd and Cr co-doped in BFO at Bi- and Fe- sites respectively.

1.3 Objectives

Now a days multiferroic property of a material is very important for practical applications. Data can be stored in ideal multiferroics by either electric or magnetic field and thus the degrees of freedom for memory storage increases. To increase multiferroic property co-doped strategy has been adopted.

The main objectives of the present research are as follows:

- Synthesis of various $Bi_{1-x}Gd_xFe_{0.9}Cr_{0.1}O_3$ (x = 0.00, 0.05, 0.10, 0.15 and 0.20) compositions.

- Study of crystal structure (by X-ray diffraction) and hence determination of lattice parameters, density and porosity of various samples.
- Investigation of surface morphology, microstructure and compositional analysis using Field Emission Scanning Electron Microscopy (FESEM) and Energy Dispersive X-ray (EDX) spectroscopy, respectively.
- Investigation of frequency dependent dielectric properties, impedance, AC conductivity.
- Measurement of complex initial permeability, loss tangent and relative quality factor as a function of frequency.
- Measurement of magnetization as a function of magnetic field at room temperature.
- Investigation of Magnetoelectric voltage coefficient as a function of DC magnetic field at room temperature.

1.4 Review works

At the first half of the twentieth century several major studies have been done by different researchers in different parts of the world for the development of magnetic materials began in Japan by researchers Kato et al. in the 1930 and by J. Snoek of the Philips Research Laboratories in the period 1935-45 in the Netherlands. By Snoek in 1945 had laid down the basic fundamentals of the physics and technology of practical ferrite materials. In 1948, the Neel theory of ferromagnetic provided the theoretical understanding of this type of magnetic material [28].

Bhole [29] synthesized the BFO ceramics by solid state reaction method. The X-ray analysis depicts the BFO sample have rhombhohedral perovskite structure. The dielectric constant and loss as a function of temperature (30-325°C) in the frequency range 10 kHz-1MHz shows that the dielectric constant and loss increases with increasing temperature. The

room temperature dielectric measurement with frequency reveals the dielectric constant and loss decreases with increasing frequency for BFO ceramics.

Weiwei et al. [25] synthesized Gd doped BFO nanoparticles by polyol-mediated method. From the XRD pattern they observed the phase transition from a rhombohedral phase for x = 0 to an orthorhombic phase for x =0.2 and 0.3, and x = 0.1 is a mixture of both phases. Doping with Gd enhanced the ferroelectric and magnetic properties of BFO.

Uniyal and Yadav [30] synthesized Gd doped BFO and studied dielectric, magnetic and ferroelectric properties. X-ray diffraction pattern showed that $Bi_{1-x}Gd_xFeO_3$ (x=0, 0.05 and 0.1) ceramics were rhombohedral. Gd substitution reduced the antiferromagnetic Néel temperature (T_N) in $Bi_{1-x}Gd_x\ FeO_3$. Magnetic hysteresis loops at room temperature were found unsaturated and indicated the coexistence of ferroelectricity and magnetism, but the magnetic moment was found to increase with increase in Gd concentration.

Khomchenko et al. [31] prepared $Bi_{1-x}Gd_xFeO_3$ (x=0.1, 0.2, 0.3) samples by conventional solid state reaction method. They found structural phase transition within the concentrational range of $0.2<x<0.3$. Also they found spontaneous magnetization in the Gd doped BFO samples.

Lotey and Verma [32] synthesized nanoparticles $Bi_{1-x}Gd_xFeO_3$ with (x = 0, 0.04, 0.08, and 0.12) by sol–gel method. They observed structural and phase transformation from rhombohedral to orthorhombic. They achieved high energy conversion efficiency, 3.85%, for 12% Gd doped BFO and observed high resistance in the Gd doped BFO.

References

[1] Smolenskii, G. A. and Chupis, I. E., "Ferroelectromagnets", *Sov. Phys. Usp.*, Vol.25, pp. 475-493, (1982).

[2] Schmid, H., "Multi-ferroic magnetoelectric", *Ferroelectrics*, Vol. 162, pp. 317-338, 1994.

[3] Selbach, S. M., "Structure, stability and phase transitions of multiferroic $BiFeO_3$", ,Doctoral Thesis at Vol. 118, 1503-8181 (2009).

[4] Eerenstein, W., Mathur, N. D and Scott, J. F., "Multiferroic and magnetoelectric materials", *Nature*, Vol. 442, pp. 759-765, 2006.

[5] Mu$\bar{n}$oz, C. T., Rivera, J. P., Bezinges, A., Monnier, A. and Schmid, H., "Measurement of the Quadratic Magnetoelectric Effect on Single Crystalline $BiFeO_3$", *Jpn. J. Appl. Phys.*, Vol. 24, pp. 1050-1053, 1985.

[6] Haneberg, D. H. "A Finite-Size Study on Samarium-Substituted Bismuth Ferrite Multiferroic and Lead-Free Piezoelectric Materials", *Norwegian University of Science and Technology*, Vol.11, June 15, 2011.

[7] Hill, N. A., "Why Are There so Few Magnetic Ferroelectrics?", *J. Phys. Chem.*, Vol. 104, pp. 6694-6709, 2000.

[8] Catalan, G. and Scott, J. F. "Physics and Applications of Bismuth Ferrite", *Adv. Mater.*, Vol. 21,pp. 2463-2485, 2009.

[9] Drexler, E., "Nanosystems: Molecular Machinery, Manufacturing, and Computation", New York: Wiley, Doctoral Thesis, 1991.

[10] Ma, J., Hu, J., Li, Z. and Nan, C. W., "Recent progress in multiferroic magnetoelectric composites: from bulk to thin film", *Adv. Mater.*, Vol. 23, pp. 1062-1087, 2011.

[11] Kumar, M. M., Palkar, V. R., Srinivas, K., and Suyanarayana, S. V., "Ferroelectricity in a pure $BiFeO_3$ ceramic", *Appl. Phys. Lett.*, Vol. 76, pp. 2764-2766, 2000.

[12] Ramesh, R., Spaldin, N. A., "Multiferroics: progress and prospects in thin films", *Nat. Mater.*, Vol. 6, pp. 21, 2007.

[13] Fischer, P., Polomska, M., Sosnowska, I. and Szymanski, M., "Temperature dependence of the crystal and magnetic structure of $BiFeO_3$", *J. Phys. C: Solid State Phys,.* Vol. 13, pp. 1931-1940, 1980.

[14] Ederer, C. and Spaldin, N. A., "Weak ferromagnetism and magnetoelectric coupling in bismuth ferrite", *Phys. Rev. B*, Vol. 71, pp. 060401(R)-4, 2005.

[15] Yuan, G. L., Wing, S., Liu, J. M. and Liu, Z. G., "Structural transformation and ferroelectromagnetic behavior in single-phase $Bi_{1-x}Nd_xFeO_3$ multiferroic ceramics", *Appl. Phys. Lett.*, Vol. 89, pp. 052905, 2006.

[16] Khomchenko, V. A., Paixao, J. A., Costa, B. F. O., Karpinsky, D. V., Kholkin, A. L., Troyanchuk, I. O., Shvartsman, V. V., Borisov, P. and Kleeman, W., "Structural, ferroelectric and magnetic properties of $Bi_{0.85}Sm_{0.15}FeO_3$ perovskite", *Cryst. Res. Technol.*, Vol. 46, pp. 238-242, 2011.

[17] Khomchenko, V. A. and Kiselev, D. A., "Synthesis and multiferroic properties of $Bi_{0.8}A_{0.2}FeO_3$ (A=Ca, Sr, Pb) ceramics", *Appl. Phys. Lett.*, Vol. 90, pp. 242901, 2007.

[18] Xu, Q. Y., Zai, H. F., Wu, D., Qiu, T. and Xu, M. X., "The magnetic properties of $Bi(Fe_{0.95}Co_{0.05})O_3$ ceramics", *Appl. Phys. Lett.*, Vol. 95, pp. 112510, 2009.

[19] Chang, F. G., Zhang, N., Yang, F.,Wang, S. X. and Song, G. L., "Effect of Cr substitution on the structure and electrical properties of $BiFeO_3$ ceramics", *J. Phy. D: Appl.* Phys., Vol. 40, pp. 7799-7803, 2007.

[20] Anjum, G., Kumar, R., Mollah, S., Shukla, D. K., Kumar, S. and Lee, C. G., "Structural, dielectric, and magnetic properties of $La_{0.8}Bi_{0.2}Fe_{1-x}Mn_xO_3$ ($0.0 \leq x \leq 0.4$) multiferroics*", J. App. Phys.*, Vol. 107, pp. 103916, 2010.

[21] Agarwal, R. A., Ashima, S. S. and Ahlawat, N., "Structural transformation and improved dielectric and magnetic properties in Ti-substituted $Bi_{0.8}La_{0.2}FeO_3$ Multiferroics", *J. Phys. D: Appl. Phys.*, Vol. 45, pp. 165001, 2012.

[22] Lin, S. G., Hui, Z. X., Jian, S., Gang, Y. H, Xing, W. T and Gao, C. F., "Effects of Gd and Co doping on the electrical and ferromagnetism properties of $BiFeO_3$ ceramics", *Acta Phys. Sin*, Vol. 61, pp. 177501, 2012.

[23] Rout, J. and Choudhary, R. N. P., "Structural transformation and multiferroic properties of Ba-Mn co-doped $BiFeO_3$", *Phys. Lett. A*, Vol. 380, pp. 288–292, 2016.

[24] Mao, W., Wang, X., Chu, L., Zhu, Y., Wang, Q., Zhang, J., Yang, J., Li, X. and Huang, W, "Simultaneous enhancement of magnetic and ferroelectric properties in Dy and Cr co-doped $BiFeO_3$ nanoparticles", *Phys. Chem. Chem. Phys.*, Vol. 18, pp. 6399-6405, 2016.

[25] Weiwei, H., Chen, Y., Yuan, H., Li, G., Qiao, Y., Qin, Y. and Feng, S., "Structure, Magnetic, and Ferroelectric Properties of $Bi_{1-x}Gd_xFeO_3$ Nanoparticles", *J. Phys. Chem. C*, Vol. 115, pp. 8869–8875, 2011.

[26] Chang, F., Na Zhang, N., Yang, F., Wang, S. X., and Song, G., "Effect of Cr substitution on the structure and electrical properties of $BiFeO_3$ ceramics," *J. Phys. D: Appl. Phys.*, Vol. 40, pp. 7799-7803, 2007.

[27] Li, J. B., Rao, G. H., Liang, J. K., Liu, Y. H., Luo, J. and Chen, J. R., "Magnetic properties of $Bi(Fe_{1-x}Cr_x)O_3$ synthesized by a combustion method," *Appl. Phys. Lett.*, Vol. 90, pp. 162513, 2007.

[28] Mahmood, L. S., "Preparation of $Co_{1-x}Zn_xFe_2O_4$ Nano ferrite and Study of Its Electrical and Structural Properties", University of Diyala, 2012.

[29] Bhole, C. P., "Ferroelectric and Dielectric Investigations of Bismuth Ferrite ($BiFeO_3$) Nanoceramics", *Scholars Research Library Archives of Applied Science Research*, Vol. 3, pp. 384-389, 2011.

[30] Uniyal, P. and Yadav, K.L., "Study of dielectric, magnetic and ferroelectric properties in $Bi_{1-x}Gd_xFeO_3$," *Mater. Lett.*, Vol. 62, pp. 2858–2861, 2008.

[31] Khomchenko, V. A., Kiselev, D. A., Bdikin, I. K., Shvartsman, V. V., Borisov, P., Kleemann, W., Vieira, J. M. and Kholkin, A. L., "Crystal structure and multiferroic properties of Gd-substituted $BiFeO_3$," *Appl. Phys. Lett.*, Vol. 93, pp. 262905 , 2008.

[32] Lotey, G. S. and Verma, N.K., "Gd-doped $BiFeO_3$ nanoparticles – A novel material for highly efficient dye-sensitized solar cells", *Chem. Phys. Lett.*, Vol. 574, pp. 71–77, 2013.

CHAPTER 2

THEORITICAL BACKGROUND

2.1 Multiferroics

Typical multiferroic belongs to the group of the perovskite transition metal oxides such as $TbMnO_3$, YMn_2O_5 and $LuFe_2O_4$. Other examples are the bismuth compounds BFO and $BiMnO_3$, and non-oxides such as $BaNiF_4$ [1]. Bismuth iron oxides or bismuth ferrites (BFO) is one of the most interesting iron-containing perovskites due to their unique multifunctional properties which are of high technological and fundamental importance [2]. The attempts to combine ferromagnetic and ferroelectric properties into one phase started in the 1960s. Although ferromagnetism or ferroelectricity can be found in numerous systems, the multiferroic materials, which show simultaneously magnetic and electric ordering in a single phase, are relatively rare. The coupling between magnetic and electric properties gives rise to additional phenomena. It can result in magnetoelectric effects in which the magnetization can be tuned by an applied electric field and vice versa. This kind of material has a large application potential for new devices.

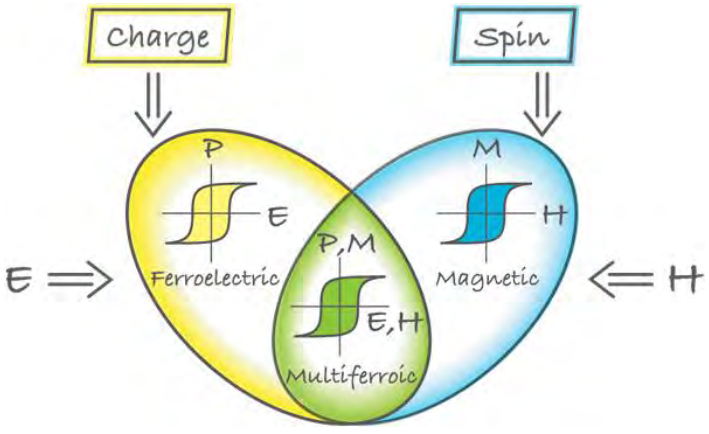

Fig. 2.1 Schematic illustration of multiferroics [4].

The coexistence of ferroelectricity and ferromagnetism and their coupling with elasticity provide an extra degree of freedom in the design of new functional sensors and multi-state memory devices [3].

The schematic diagram of multiferroicity is shown in Fig. 2.1. In figure, the left portion shows ferroelectric and the right portion shows ferromagnetic property, and the intersection of ferroelectric and ferromagnetic represents multiferroic property. The materials which have coexistence of ferroelectric and magnetic orders are called Multiferroics.

2.2 Types of Multiferroics

According to the materials constituents, multiferroic materials can be divided into two types:

(i) Single phase and

(ii) Composite

A single phase multiferroic material is one that possesses at least two of the ferroic properties, such as ferroelectricity, ferromagnetism or ferroelasticity. Natural single phase multiferroic compounds are rare, and their magnetoelectric responses are either relatively weak or occurs at temperature too low for practical applications.

The ME effect in composite material is known as a product property [5, 6], which results from the cross interaction between different orderings of the two phases in the composite. Neither the piezoelectric nor magnetic phase has the ME effect, but composites of these two phases have remarkable ME effect.

Single phase multiferroics can be classified are two groups:

(i) Type-I multiferroics

(ii) Type-II multiferroics

2.2.1 Type-I multiferroics

Type-I multiferroics are those materials in which ferroelectricity and magnetism have different sources; usually they show large polarization values and ferroelectricity appears at much higher temperature than magnetism. This difference in transition temperature reveals that both orders involve different energy scales and mechanisms, which provokes the occurrence of weak magnetoelectric coupling. BFO is the example of type-I multiferroic.

2.2.2 Type-II multiferroics

Type-II multiferroic is novel class of multiferroics in which ferroelectricity exists only in a magnetically ordered state and caused by a particular type of magnetism. Type-II multiferroics divided into two groups: those in which ferroelectricity is caused by a particular type of magnetic spiral and those in which ferroelectricity appears even for collinear magnetic structures. $TbMnO_3$, $HbMnO_3$ are the examples of type-II multiferroic.

2.3 Perovskite Structure

The perovskite structure type is one of the most frequently encountered in solid-state inorganic chemistry. The general formula for perovskite structure is ABO_3. Perovskite take their name from the calcium titanium oxide ($CaTiO_3$) compound, which was first discovered in the Ural Mountains of Russia by Gustav Rose in 1839. In the ideal cubic unit cell, 12-coordinated A- site cations sit on the corners of the cube, octahedral O ions on the faces, and the B ion is in the center of the octahedral cage. Due to the flexibility of the corner-sharing octahedra, the perovskite structure can be easily distorted to accommodate a wide range of valence states on both the A- and B- sites by expanding, contracting the lattice or by rotating the bond angles. The resulting symmetry of distorted perovskite could be tetragonal, orthorhombic, rhombohedral or monoclinic [7]. For such perovskite structures the tolerance

factor "t" was introduced by Goldschmidt [8]. And the relationship between "t" and the ionic radii r_A, r_B and r_O of A, B and O ions respectively is generally defined as:

$$t = \frac{r_A + r_O}{\sqrt{2}(r_B + r_O)} \qquad (2.1)$$

where t = 1 for the ideal cubic perovskite, but in practice there is some flexibility and the cubic structure can form with 0.9 < t < 1.0. The BX_6 octahedral can be tilted, rotated or distorted to compensate for the nonideal cation sizes and hence alter the unit cell forming a superstructure.

The tilting classification scheme by Glazer can be used to systematically characterize the resultant superstructures [9].

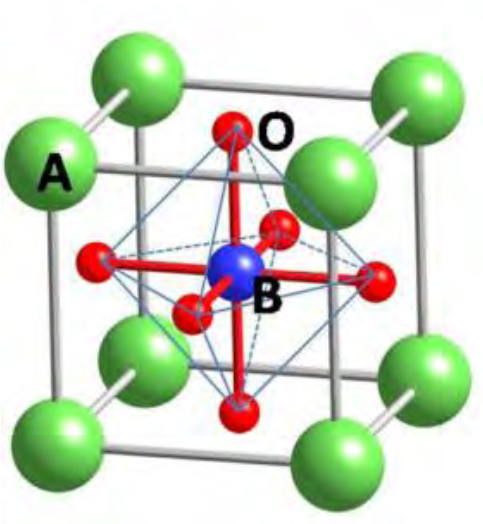

Fig. 2.2 Perovskite ABO_3 structure with A and B cations on the corner and body centre positions, respectively.

2.4 Bismuth ferrite

BFO is perhaps the only material that has both magnetic and strong ferroelectric properties at room temperature. Bismuth ferrite is probably the most well-studied Bi-based perovskite ferroelectric, due to its multiferroic properties [10]. The study of BFO, as a multiferroic material, had been started in 1958 by Smolenskii and colleagues but they were not able to grow single crystals and the polycrystalline ceramics were not useful for practical applications owing to their high conductivity [11]. Bismuth ferrite (BFO) has very high

ferroelectric curie temperature ($T_c = 1100$ K or 827 C and shows G-type antiferromagnetic having cycloidal spin structure with Néel temperature (T_N=650K or 377°C). In its ferroelectric state, BFO shows a rhombohedrally distorted pervoskite structure [12].

2.5 Magnetic properties

Ferromagnetism is the existence of a spontaneous magnetization which can be reversed by an opposite magnetic field, in the same way as electric polarization can be reversed by an electric field. All materials in nature possess general form of diamagnetic response to an applied magnetic field [14]. There are several other magnetic phenomena present in some inorganic solids caused by unpaired electrons usually located on metal cations. The different effects for a schematic are shown in Fig. 2.3 [13]. Paramagnetism (Fig. 2.3 (A)) is a state where the magnetic polarization is randomly oriented and with a positive magnetic susceptibility, meaning that the material is in a state where it is attracted to the magnetic field. Unlike ferromagnetism (Fig. 2.3 (B)), where induced magnetic moment is retained in the absence of an externally applied magnetic field, and thermal motion causes the spins to become randomly oriented, reducing the total magnetization to zero when the field is removed. In antiferromagnetism (Fig. 2.3 (C)), the overall magnetic moment is zero due to neighboring spins pointing in opposite directions, whereas ferrimagnetism (Fig. 2.3 (D)) occurs when neighboring spins are pointing in opposite directions but of unequal size.

As ferromagnets experience a phase transition from ferromagnetic to paramagnetic orientation above the Curie temperature T_c, antiferromagnets experience a phase transition from antiferromagnetic to paramagnetic above the Néel temperature T_N [15]. Each Fe^{3+} with spin up is surrounded by six nearest neighbors with spin down. Perpendicular to the polar [111] hex axis is the easy plane of magnetization ((001) hex), this can be visualized in Fig. 2.4 [16].

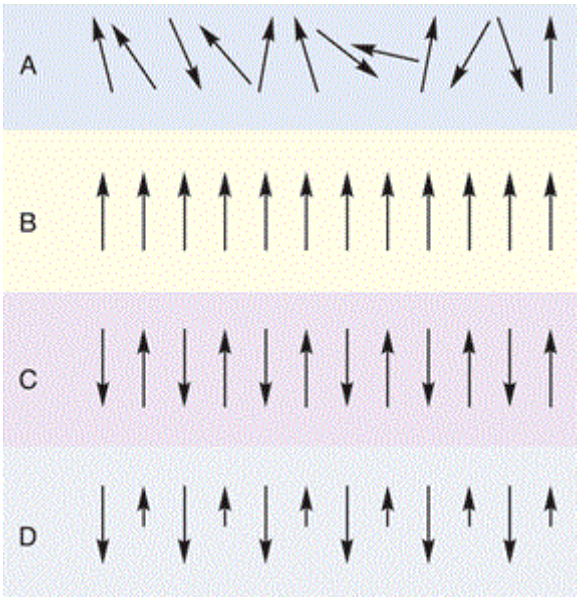

Fig. 2.3 Schematic magnetic phenomena: (A) paramagnetism; (B) ferromagnetism; (C) antiferromagnetism; (D) ferrimagnetism [13].

The reduction of the Fe-O-Fe angle from 180° caused by the tilting of the FeO_6 octahedra reduces the overlap of O and Fe orbitals. It is this tilting of the sublattices to 154-155 that yields a weak ferromagnetic moment. This is however cancelled due to an average spiral modulation [16].

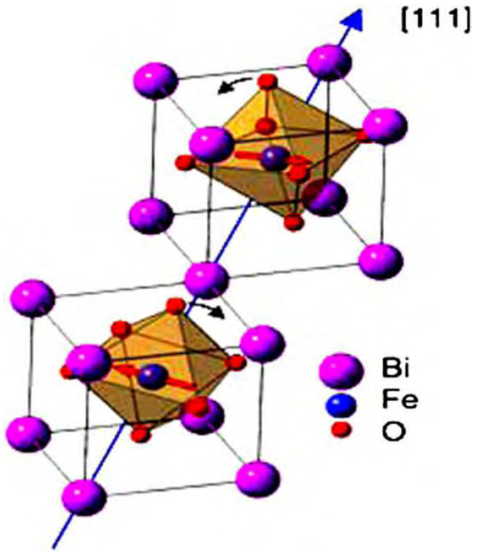

Fig. 2.4 Structure of BFO_3 Shows the tilted FeO_6 octahedra giving rise to the total weak ferromagnetic moment which in turn is cancelled due to average spiral modulation [17].

2.6 Magnetoelectric effect

Magnetoelectric (ME) effect is an important phenomenon for multiferroic materials. The induction of electric polarization by means of a magnetic field and the induction of magnetization by means of an electric field is defined as the ME effect (Fig. 2.5). The ME effect was theoretically explained by Dzyaloshinkii [18] with a prediction being made for Cr_2O_3 that was verified experimentally in this compound by Astrov [19] in late 1950s. After several years, the ME effect was observed in boracites materials ($Ni_3B_7O_{13}I$) by Schmid [1]. ME effect in perovskite compound BFO was first observed by Smolenskii and Chupis [20]. The ME effects can be linear or/and non-linear with respect to the external electric field or magnetic field. In single phase multferroics the ME effect can be due to the coupling of magnetic and electric orders as observed in some multiferroics. The ME effect in composites is the result of mechanical coupling between ferroelectric and ferromagnetic materials.

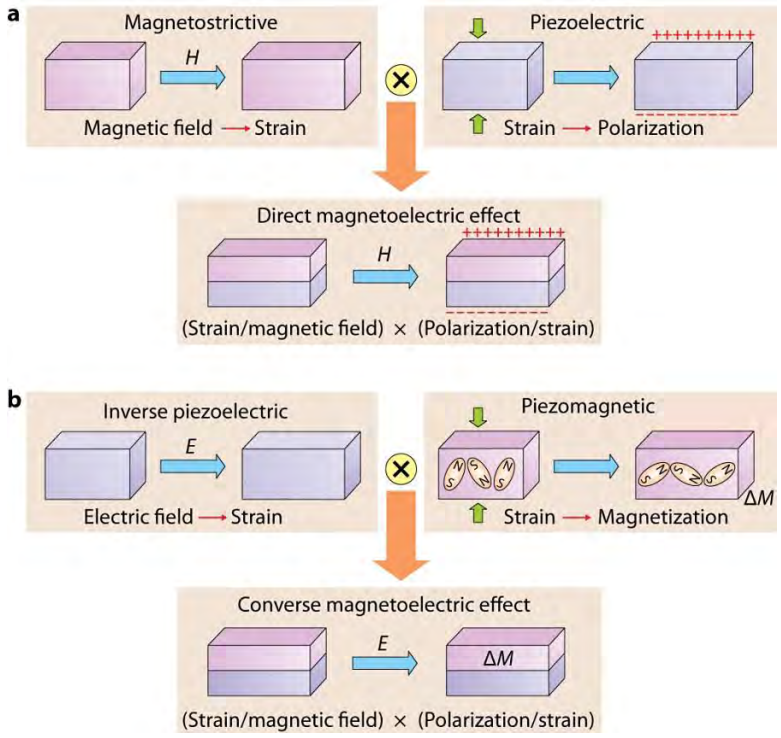

Fig. 2.5 Schematic diagram of ME effect in multiferroic materials [21].

2.7 Theory of Permeability

Permeability (μ) is defined as the proportionality constant between the magnetic field induction B and applied field intensity H:

$$B = \mu H \tag{2.2}$$

If the applied field is very low, approaching zero, the ratio is called the initial permeability (μ_i), Fig. 2.6 and is given by,

$$\mu_i = \frac{B}{H} \tag{2.3}$$

where $H \rightarrow 0$

This simple definition needs further sophistications. A magnetic material subjected to an AC magnetic field can be written as

$$H = H_0 e^{i\ t} \tag{2.4}$$

It is observed that the magnetic flux density B lag behind H. This is caused due to the presence of various losses and is thus expressed as

$$B = B_0 e^{i(\ t-\delta)} \tag{2.5}$$

Here δ is the phase angle that marks the delay of B with respect to H. The permeability is then given by

$$\mu = \frac{B}{H} = \frac{B_0 e^{i(\ t-\delta)}}{H_0 e^{i\ t}} = \frac{B_0 e^{-i\delta}}{H_0} = \frac{B_0}{H_0}\cos\delta - i\frac{B_0}{H_0}\sin\delta = \mu' - i\mu'' \tag{2.6}$$

where $\mu' = \frac{B_0}{H_0}\cos\delta$ (2.7)

and $\mu'' = \frac{B_0}{H_0}\sin\delta$ (2.8)

The real part (μ') of complex initial permeability (μ) represents the component of B which is in phase with H, so it corresponds to the normal permeability. If there are no losses, it should have $\mu=\mu'$. The imaginary part (μ'') corresponds to that of B, which is delayed by

phase angle 90 from H [22, 23]. The presence of such a component requires a supply of energy to maintain the alternating magnetization, regardless of the origin of delay.

The ratio of μ'' and μ' gives,

$$\frac{\mu''}{\mu'} = \frac{\frac{B_0}{H_0}\sin\delta}{\frac{B_0}{H_0}\cos\delta} = \tan\delta_M \qquad (2.9)$$

This $\tan\delta_M$ is called magnetic loss factor.

The quality factor is defined as the reciprocal of this loss factor, i.e,

$$\text{Quality factor, } Q = \frac{1}{\tan\delta_M} \qquad (2.10)$$

$$\text{And the relative quality factor, } RQF = \frac{\mu'}{\tan\delta_M} \qquad (2.11)$$

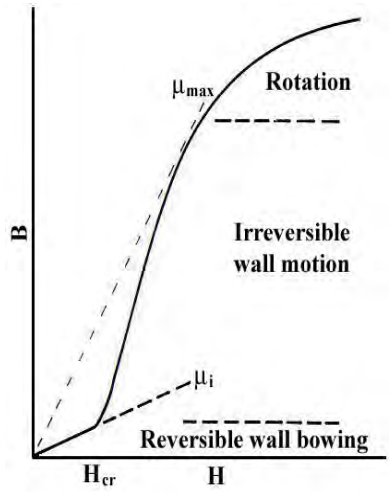

Fig. 2.6 Schematic magnetization curve showing the important parameter:initial permeability, μ_i.(the slope of the curve at low fields) and the main magnetization mechanism in each magnetization range.

The curves that show the variation of both μ' and μ'' with frequency are called the magnetic spectrum or permeability spectrum of the materials [22]. The variation of permeability with frequency is referred to as dispersion. The measurement of complex permeability gives us valuable information about the nature of domain wall and their movements. In dynamic measurements the eddy current loss is very important. This occurs due to the irreversible domain wall movements. The permeability of a ferromagnetic

substance is the combined effect of the wall permeability and rotational permeability mechanisms.

2.8 Mechanism of Permeability

The mechanisms of permeability can be explained as follows: A demagnetized magnetic material is divided into number of Weiss domains separated by Bloch walls. In each domain all the magnetic moments are oriented in parallel and the magnetization has its saturation value M_s. In the walls the magnetization direction changes gradually from the direction of magnetization in one domain to that in the next. The equilibrium positions of the walls results from the interactions with the magnetization in neighboring domains and from the influence of pores; crystal boundaries and chemical inhomogeneities which tend to favour certain wall positions.

2.9 M-H hysteresis loop

The relationship between field streangth (H) and magnetization (M) is not linear in ferromagnetic materials. If a magnet is demagnetized (H=M=0) and the relationship between H and M is plotted for increasing levels of field strength, M follows the initial magnetization curve. This curve increases rapidly at first and then approaches an asymptote called magnetic saturation. If the magnetic field is now reduced monotocally, M follows a different curve. At zero field streangth, the magnetization is offset from the origin by an amount called the remanence. If the M-H relationship is plotted for all streangths of applied magnetic field the result is a hysteresis loop (Fig. 2.7). The lack of retraceability of the magnetization curve is the property called hysteresis and it is related to the existence of magnetic domains in the material. Once the magnetic domains are reoriented, it takes some energy to turn them back again. This property of ferromagnetic materials is useful as a magnetic memory. Technical terms are defined by the hysteresis loop is shown in Fig. 2.7. Remanent magnetization (M_r) is

the magnetization left behind in a ferromagnetic material after an external magnetic field is dropped to zero from saturation. The coercivity (H_c) is usually defined as the reverse field H that reduces the magnetization M to zero, starting from saturation.

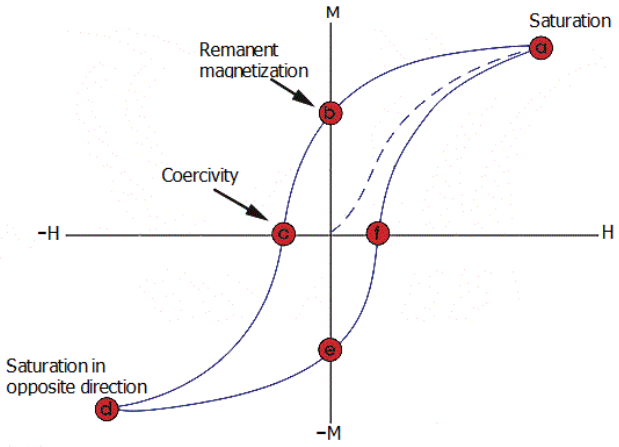

Fig. 2.7 M-H curve showing different technical terms.

2.10 Electrical Properties

The investigations into electrical properties are essential for their use in various applications as dielectric behavior and conductivity measurement; i.e. (dielectric constant, dielectric loss factor and ac conductivity) as a function of frequency.

2.10.1 Dielectric properties

A material is classified as “dielectric” if it has the ability to store energy when an external electric field is applied. These properties are not constant; they can change with frequency, temperature, orientation, mixture, and pressure and molecule structure of the material. For most solids, there is no net separation of positive and negative charges; that there is no net dipole moment. The molecules of solids are arranged in such a way that the unit cell of the crystal has no net dipole moment. If such a solid is placed in electric field then the field is induced in the solid which opposes the applied electric field. This field arises from the two sources, a distortion of the electron cloud of the atoms or molecules and a slight movement of the atoms themselves. The average dipole moment per unit volume induced in

the solid is the electrical polarization and is proportional to the applied electric field. The polarizability (α) of the dielectric is defined by [24]:

$$P = \quad E \qquad (2.12)$$

where, p is the dipole moment induced by local electric field, E.

Polarization can be divided into four categories, each having a distinct mechanism based on the type of dipole moment which is established [24]:

$$= \quad _e + \quad _i + \quad _d + \quad _s \qquad (2.13)$$

where, $_e$ is electric polarization, $_i$ is an ionic polarization, $_d$ is dipolar polarization and $_s$ is space charge polarization.

2.10.1.1 Electric polarization

Electric polarization is the slight relative shift of positive and negative electric charge in opposite directions within an insulator, or dielectric, induced by an external electric field. Polarization occurs when an electric field distorts the negative cloud of electrons around positive atomic nuclei in a direction opposite the field. This slight separation of charge makes one side of the atom somewhat positive and the opposite side somewhat negative. In some materials whose molecules are permanently polarized by chemical forces, such as water molecules, some of the polarization is caused by molecules rotating into the same alignment under the influence of the electric field.

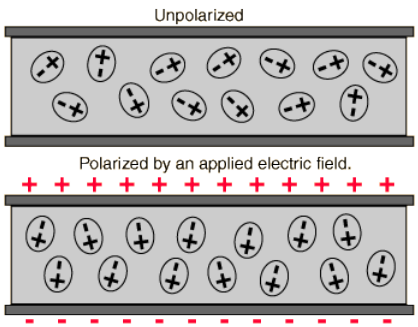

Fig. 2.8 Schematic illustration of electronic polarization.

2.10.1.2 Ionic polarization

An ionic crystal would possess polarization even in the absence of an electric field, since each ion pair constitutes an electric dipole. But this is not so, because the lattice symmetry ensures that these dipoles cancel each other everywhere. Actually the polarization in ionic crystals arises on account of the fact that the ions are displaced from their equilibrium positions by the force of the applied electric field.

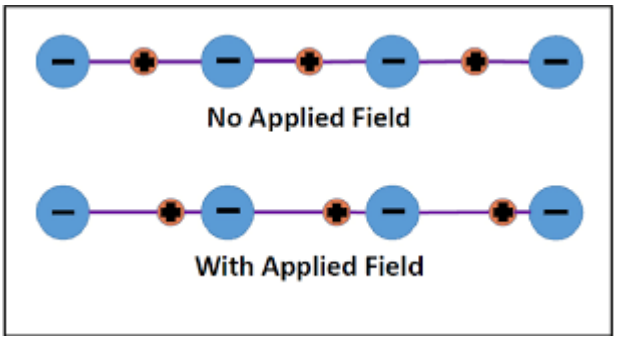

Fig. 2.9 Schematic illustration of ionic polarization.

2.10.1.3 Orientational Polarization

Permanent dipole moment in a material gives rise to orientational polarization. In the absence of an electric field, the dipole moment is canceled out by thermal agitation, therefore, net zero dipole moment per molecule is formed. Else there is no dipole moment even if the material is dipolar. When an electric field is applied the molecule begins to rotate and aligns with the field, causing a net average dipole moment per molecule.

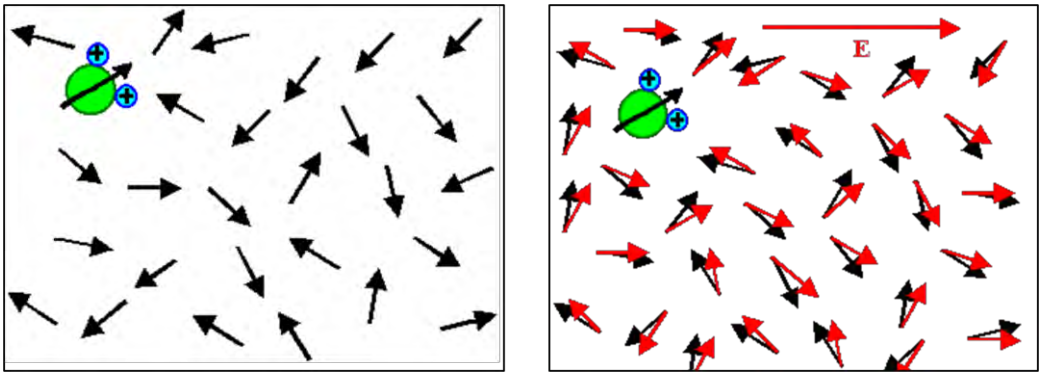

Fig. 2.10 Schematic illustration of orientational polarization.

2.10.1.4 Interfacial Polarization

This occurs when there is an accumulation of charge at an interface between two materials because of an external field. This kind polarization is also called space charge polarization. When there are two electrodes connected to a dielectric material instead of affecting bound positive and negative charges i.e. ionic and covalent bonded structures, interfacial polarization also affects free charges. This makes it different from orientational and ionic polarization. Interfacial polarization is usually observed in amorphous or polycrystalline solids. The electric field will cause a charge imbalance mobile charges in the dielectric will migrate over maintain charge neutrality. This then causes interfacial polarization. Space charge polarizability occurs in materials that are not perfect dielectrics but in which some long range charge migration may occur. When such effects are appreciable, the material is better regarded as a conductor or solid electrolyte than as a dielectric [25].

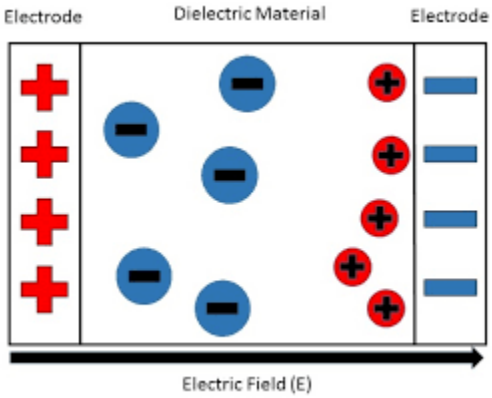

Fig. 2.11 Schematic illustration of interfacial polarization.

2.10.2 Dielectric Parameters

The dielectric constant was determined using LCR Meter Bridge. For this purpose silver paint was applied on both sides of the pellets to make good contacts with conducting wires. It is defined as the ratio of the charge that would be stored with free space to that stored with the material in question as the dielectric. Capacitance of the pellets was

determined from the LCR meter and then dielectric constant was calculated using the formula [26]:

$$' = \frac{C}{C_0} \tag{2.14}$$

C is the capacitance of the material and C_0 is the capacitance of free space, and

$$C_0 = {}_0\frac{A}{d} \tag{2.15}$$

Where ε_0 is the permittivity of the free space and has a value of ($8.854\times10\text{-}12$ Fm^{-1}).

The equation (2.14) becomes:

$$' = \frac{Cd}{{}_0A} \tag{2.16}$$

Where d is the thickness of the pellet in meters, A is the crosssectional area of the flat surface of the pellet [26].

When a dielectric is subjected to the ac voltage, the electrical energy is absorbed by the material and is dissipated in the form of heat. The dissipation is called dielectric loss. When the applied frequency is in the same range as the relaxation time, resonance occurs. Fig. 2.8 show the phase relationship between current and voltage, so the current lead the voltage by (90- δ), where δ is called the loss angle and $tan\delta_E$ is the electrical loss due to resonance and called as tangent loss, and the loss tangent can be expressed as [27]:

$$\tan\delta_E = \frac{''}{'} \tag{2.17}$$

where, ε' and ε" are real and imaginary part of relative permittivity

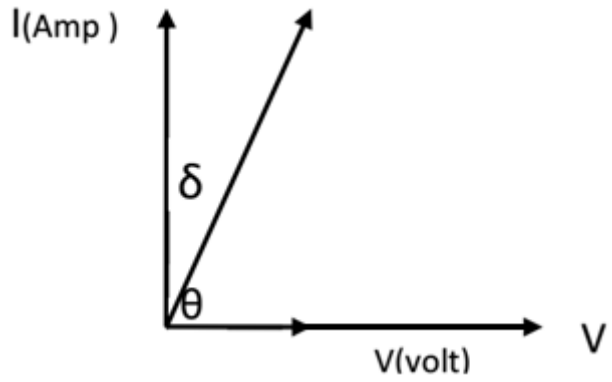

Fig. 2.12 Phase diagram between current and voltage [28].

The current can be resolved into two components:

1. The component in phase with the applied voltage is: $I_x = v\,\omega\varepsilon''c_0$. It gives the dielectric loss.

2. The component leading the applied voltage by 90 , is $I_y = v\,\omega\varepsilon' c_0$.

The dielectric constant depends strongly on the frequency of the alternating electric field and on the chemical structure, imperfection of the material, temperature and pressure. The AC conductivity was calculated from the values of dielectric constant and dielectric loss factor using the relation [28]:

$$_{AC} = \quad _0 \, '\tan\delta_E \qquad (2.18)$$

where $_{AC}$ is the ac conductivity and ω is the angular frequency.

2.11 Electrical Conductivity

This section deals with response of ceramics to the application of a constant electric field and the nature and magnitude of steady-state current that is proportional to a material property known as conductivity. In metal, free electrons are solely responsible for conduction. In semiconductors, the conducting species are electrons and/or electron holes. In ceramics, however, because of presence of ions, the application of electric field can induce these ions to migrate. Therefore, when dealing with conduction in ceramics, one must consider both the ionic and the electronic contributions to the overall conductivity. The

proportionality constant (σ) is the conductivity of material, which is the conductance of a cube of material of unit cross section. The unit of conductivity is Siemens per meter or S/m, where $S=\Omega^{-1}$, [29]. The electrical properties of ferrites depend on the charge transport among B-site ions.

2.12 Jonscher's power law

Electrical conductivity of solid materials as a function of frequency can generally be described as frequency independent, dc conductivity ($_{dc}$) and a strongly frequency dependent components. A typical frequency dependence of conductivity spectrum shown in the Fig 2.9 exhibits three distinguish regions; (a) low frequency dispersion, (b) an intermediate plateau and (c) an extendent dispersion at high frequency region.

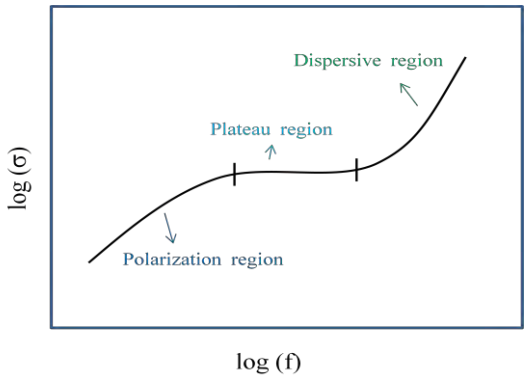

Fig. 2.13 Schematic representation of log ( ) vs log (f).

The variation of conductivity in the low frequency region is attributed to the polarization effects at the electrode and materials interface. As the frequency reduces, more and more, charge accumulation occurs at the electrode and materials interface and hence, drop in conductivity. In the intermediate frequency plateau region, conductivity is almost found to be frequency independent and is equal to $_{dc}$. In the high frequency region, the conductivity increases with the frequency and is equal to $_{AC}$. The frequency dependence of conductivity is related to a simple expression given by Jonscher's power law [30],

$$( ) = (0) + A^{\ s} \qquad (2.19)$$

where ( ) is the AC conductivity, (0) is the limiting zero frequency conductivity $_{dc}$, A is a pre-exponential constant, = 2πf is the angular frequency and 's' is the power law exponent, where 0<s<1. Both 'A' and 's' are temperature and materials dependent [30].

2.13 Impedance Spectroscopy

Impedance spectroscopy (IS) is a relatively new and powerful method of characterizing many of the electrical properties of materials and their interfaces with electronically conducting electrodes. It may be used to investigate the dynamics of bound or mobile charge in the bulk or interfacial regions of any kind of solid or liquid material: ionic, semiconducting, mixed electronic-ionic and even insulators (dielectrics). Any intrinsic property that influences the conductivity of an electrode-material system, or an external stimulus, can be studied by IS. The parameters derived from an IS spectrum fall generally into two categories: (a) those pertinent only to the material itself, such as conductivity, dielectric constant, mobilities of charges, equilibrium concentrations of the charge species, and bulk generation-recombination rates; and (b) those pertinent to an electrode-material interface, such as adsorption-reaction rate constants, capacitance of the interface region, and diffusion coefficient of neutral species in the electrode itself.

The electrical impedance is the measure of the opposition that a circuit presents to a current when a voltage is applied. The term impedance was coined by Oliver Heaviside in July 1886 [31]. Arthur E. Kennelly was the first to represent impedance with complex numbers [32]. In quantitative terms, it is the complex ratio of the voltage to the current in an alternating current (AC) circuit. Impedance extends the concept of resistance to AC circuits, and possesses both magnitude and phase, unlike resistance, which has only magnitude. When a circuit is driven with direct current (DC), there is no distinction between impedance and resistance; the latter can be thought of as impedance with zero phase angle. It is necessary to

introduce the concept of impedance in AC circuits because there are two additional impeding mechanisms to be taken into account besides the normal resistance of DC circuits: the induction of voltages in conductors self-induced by the magnetic fields of currents (inductance), and the electrostatic storage of charge induced by voltages between conductors (capacitance). The impedance caused by these two effects is collectively referred to as reactance and forms the imaginary part of complex impedance whereas resistance forms the real part. The symbol for impedance is usually Z.

Impedance is defined as the frequency domain ratio of the voltage to the current [33]. In other words, it is the voltage–current ratio for a single complex exponential at a particular frequency ω. In general, impedance will be a complex number, with the same units as resistance, for which the SI unit is the ohm (Ω). For a sinusoidal current or voltage input, the polar form of the complex impedance relates the amplitude and phase of the voltage and current. Ohm's law (Eq. 2.19) defines resistance in terms of the ratio between input voltage V and output current I:

$$R = \frac{V}{I} \qquad (2.20)$$

While this is well-known relationship, its use is limited to only one circuit element-the ideal resistor. An ideal resistor follows Ohm's law at all current, voltage, and ac frequency levels. Impedance is more general concept than either pure resistance or capacitance, as it takes the phase differences between the input voltage and output current into account. Like resistance, impedance is the ratio between voltage and current, demonstrating the ability of a circuit to resist the flow of electrical current, represented by the "real impedance" term, but it also reflects the ability of a circuit to store electrical energy, reflected in the "imaginary impedance" term. Impedance can be defined as a complex resistance encountered when current flows through a circuit composed of various resistors, capacitors, and inductors. This

definition is applied to both direct current (DC) and alternating current (AC). The voltage signal V(t), expressed as a function of time t, has the form:

$$V(t) = V_A \sin(\ t) \tag{2.21}$$

In a linear system, the response current signal I(t) is shifted in phase (φ) and has a different amplitude, I_A:

$$I(t) = I_A \sin(\ t + \varphi) \tag{2.22}$$

Now the complex impedance Z* is the ratio of input voltage V(t) and output current I(t):

$$Z^* = \frac{V(t)}{I(t)} = \frac{V_A \sin(\ t)}{I_A \sin(\ t+\varphi)} = Z_A \frac{\sin(\ t)}{\sin(\ t+\varphi)} \tag{2.23}$$

Using Euler's relationship:

$$\exp(j\ ) = \cos\varphi + j \sin\varphi \tag{2.24}$$

it is possible to express the impedance as a complex function. The potential V(t) is described as:

$$V(t) = V_A e^{j\ t} \tag{2.25}$$

And the current response as:

$$I(t) = I_A e^{j\ t - j\varphi} \tag{2.26}$$

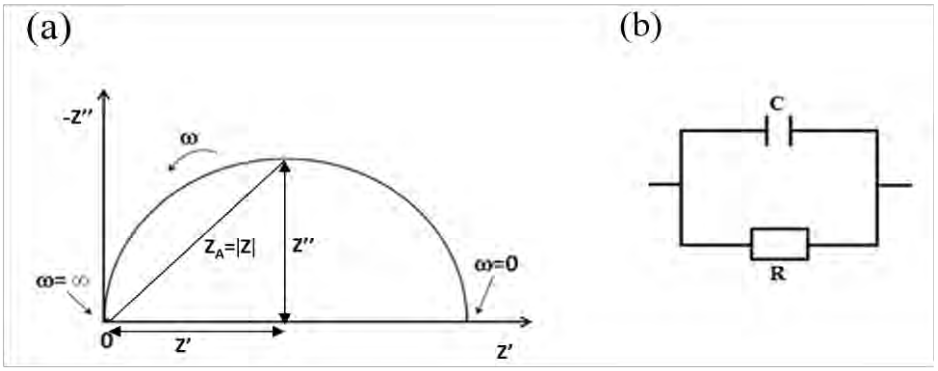

Fig. 2.14 Impedance data representation: Complex impedance plot.

The impedance is then represented as a complex number that can also be expressed in complex mathematics as a combination of "real" or in phase (Z') and "imaginary" or out of phase (Z'') parts (Fig. 2.10):

$$Z^* = \frac{V}{I} = Z_A e^{j} = Z_A \cos\varphi + j \sin\varphi = Z' + jZ'' \qquad (2.27)$$

References

[1] Schmid, H., "Multi-ferroic magnetoelectric", Ferroelectrics, Vol.162, pp. 317-338, 1994.

[2] N. A. Hill, "Why Are There so Few Magnetic Ferroelectrics", *J. Phys. Chem. B*, Vol. 104 (29), pp. 6694–6709, 2000.

[3] Tae-Jin Park, "Multifunctional Iron-Based Metal Oxide Nanostructured Materials: Synthesis, Characterization, and Properties" State University of New York At Stony Brook", Vol. 204 pp. 3334925, 2007.

[4] Spaldin, N. A. and Fiebig, M., "The Renaissance of magnetoelectric multiferroics", *Science*, Vol. 309, pp. 391-392, 2005.

[5] Suchetelene, J. V., "Product properties: Anew application of composite materials", *PhilipsRes. Rep.*, Vol. 27, pp. 28-37, 1972.

[6] Newnham, R. E., Skinner, D. P. and Cross, L. E., "Connectivity and piezoelectric-pyroelectric composites", *Mater. Res. Bull.*, Vol. 13, pp. 525-536, 1978.

[7] Goldschmidt, V. M., Vidensk, S. N. and Oslo, A. I., "Geochmical Distrbution Laws of the Elements.VIII. Reserches on the Structure and Propeties of Crystals", *Mat. Nat.*, Vol. 8, pp. 7-156, 1926.

[8] Glazer, A. M., "The Classification of Tilted Octahedra in Perovskites", *Acta. Cryst.*, Vol. B28, pp. 3384- 3392, 1972.

[9] Rabe, K., Dawber, M., Lichtensteiger, C., Ahn, C. H. and Triscone, J. M., "Modern Physics of Ferroelectrics: Essential Background", Verlag Berlin Heidelberg, *Topics Appl. Physics*, Vol. 105, pp. 1–30, 2007.

[10] Shetty, S., Palkar, V. R. and Pinto, R., "Size Effect Study in Magnetoelectric $BiFeO_3$ System", *J. Phys.*, Vol. 58, pp. 1027–1030, 2002.

[11] Achenbach, G. D. "The Atomic Structure of $BiFeO_3$", *J. Am. Ceram. Soc.*, Vol. 50, pp. 437, 1967.

[12] Honig, J.M. and Rao, C.N.R., *Preparation and Characterization of Materials*, Academic Press, New York, pp. 249-266, 1981.

[13] Kubel, F. and Schmid, H., "Structure of a Ferroelectric and Ferroelastic Monodomain Crystal of the Perovskite $BiFeO_3$", *Acta Crystallogr., Sect. B: Struct. Sci*, Vol. B46, pp 698-702, 1990.

[14] Goodenough, J. B., "Theory of the Role of Covalence in the Perovskite-Type Manganites [La, M(II)]MnO_3", *Phys. Rev.*, Vol. 100, pp. 564-573, 1955.

[15] Faqir, H., Chiba, H., Kikuchi, M., Syono, Y., Mansori, M., Satre, P. and Sebaoun, A., "High-Temperature XRD and DTA Studies of $BiMnO_3$ Perovskite", *J. Solid State Chem*., Vol. 142, pp.113-119, 1999.

[16] Sort, J., Surmach, S., Munoz, J. S. and Baro, M. D., "Improving the Energy Product of Hard Magnetic Materials", *Phys. Rev. B*, Vol. 65, pp. 174420, 2002.

[17] Park, J. H., Woodward, P. M. and Parise, J. B., "Predictive Modeling and High Pressure-High-Temperature Synthesis of Perovskites Containing Monovalent Silver", *Chem. Mater.*, Vol. 10, pp. 3092-3100, 1998.

[18] Dzyaloshinkii, I. E., "On the magneto-electrical effects in antiferromagnets", *Zh. Eksp. Teor. Fiz.*, Vol. 37, pp. 881-882, 1959 [Sov. Phys. JETP, Vol. 10, pp. 628-629, 1959].

[19] Astrov, D. N., "The magnetoelectric effect in antiferromagnetics", *Zh. Eksp. Teor. Fiz.*, Vol. 38, pp. 984-985, 1960 [Sov. Phys. JETP, Vol. 11, pp. 708-709,1960].

[20] Smolenskii, G. A. and Chupis, I. E., "Ferro-electromagnets", *Usp. Fiz. Nauk.*, Vol. 137, pp. 415-448, 1982.

[21] Wang, Y., Hu, J., Lin, Y. and Nan, C. W., "Multiferroic magnetoelectric composite nanostructures", *NPG Asia Mater.*, Vol. 2, pp. , 61–68, 2010.

[22] Wahab, M. A., *Solid State Physics: Structure and Properties of Materials*, Narosa Publishing House, New Delhi, 1999.

[23] Kittel, C., *Introduction to Solid State Physics*, 7th edition, Jhon Wiley & Sons, Inc., Singapore, 1996.

[24] Chikasumi, S., *Book of Physics of Magnetism,* Published by John Wiley and Sons, 554 pages, 1964.

[25] Kasap, S. O., *Principles of electronic materials and devices*, Published by Tata McGaw-Hill Education Pvt. Ltd., ISBN 10: 0070648204 / ISBN 13: 9780070648203, 2007.

[26] Rao, K. H., Raju, S. B., Aggarwal, K. and Mendiratta, R. G., "Effect of Cr Impurity on the dc Resistivity of Mn-Zn ferrites", *J. Appl. Phys.*, Vol. 52, pp. 1376, 1981.

[27] Wahab, M. A., "The effect of residual strains on the progressive damage Modelling of Environmentally Degraded Adhesive Joints", *J. Adhes. Sci. Technol.*,Vol.19, pp. 525-547, 2005.

[28] Eerenstein, W, Mathur, N. D and Scott, J. F., "Multiferroic and Magnetoelectric Materials", *Nature*, Vol. 442, pp. 759-765, 2006.

[29] Spaldin, N. A., *Magnetic Materials Fundamentals and Applications*, Cambridge University Press, 2003.

[30] Joncher, A. K., "The universal dielectric response", *Nature*, Vol. 267, pp. 673-679, 1977.

[31] Heaviside, O., *Electrical Papers*, Cambridge University Press, 1982.

[32] Kennelly, A. E., "The Impedances, Angular Velocities and Frequencies of Oscillating-Current Circuits", *Proceeding of the Institute of Radio Engineers*, Vol. 4, pp. 47-78, 1916.

[33] Alexander, C. K. and Sadiku, N. O., *Fundamentals of Electric Circuits*, McGraw-Hill, (3rd, revised ed.), pp. 387–389, 2006.

CHAPTER 3

SAMPLE PREPARATION AND EXPERIMENTAL TECHNIQUES

In this chapter, basic experimental methods of sample preparation and characterization techniques are discussed. A short description of the apparatus used in the measurements also given.

3.1 Sample Preparation

3.1.1 Preparation techniques

Due to the wide range of applications, bismuth ferrite has been synthesized using different methods. Some of the methods are given below:

- Solid state reaction method
- Sol-gel method
- Thin film method
- Combustion method
- Melt quenched or glass ceramic method
- Organic precursors
- Spray drying
- Freeze drying

To prepare my sample I used standard solid state reaction method. In this method, calcination, sintering, annealing etc. are responsible for the properties of the materials.

3.1.2 Solid State Reaction Method

Solid state reaction method is a conventional way to synthesis materials mainly due to its simplicity, practical effectiveness, and the low cost. The diffusion between ions is the principle mechanism of solid state reaction. Standard process for solid state reaction are as following: First, high purity reagents, such as metallic oxides, are weighted stoichiometrically in a agate mortar. Second, those powders are well ground in order to reduce the volume of

particles and to make the mixture become homogeneous. Third, the mixture is calcined and/or sintered at high temperature to allow the cations being distributed uniformly. After going through the above three steps, the new material is formed. According to this principle mechanism, the quality of sample prepared by solid state reaction technique is influenced significantly by the uniformities of composition, particle sizes, and size distributions. Consequently, the crucible factors of solid state reaction method are the properties of reagents, the uniformity of the mixture, the heating / cooling rate of sintering temperature, and sintering time etc. However, little alumina of alumina crucible may participate in the reaction during the calcination which results in multiphase and no stoichiometric compositions.

3.1.3 Synthesis of samples for the present research

$Bi_{1-x}Gd_xFe_{0.9}Cr_{0.1}O_3$ ceramics with x=0.00, 0.05, 0.10, 0.15 and 0.20 were prepared by standard solid state reaction method. High purity of Bi_2O_3, Fe_2O_3, Gd_2O_3 and Cr_2O_3 are used for $Bi_{1-x}Gd_xFe_{0.9}Cr_{0.1}O_3$. The raw materials are mixed in stoichiometric amount. The raw materials are weighed separately by using an electronic digital analytical balance, weight being shown by LED display and then well mixed and grinded in an agate mortar for 3 hours using acetone as mixing medium. The grinded powder thus poured into a alumina crucible and placed in the furnace for calcinations purpose.

3.1.4 Calcination schedule

The grinded powders were calcined in air at a temperature of 800 °C for 1 hour to remove the unwanted oxides present in the chemicals. After 1 hour it was cooled to room temperature (furnace cooling). When room temperature was attained the chunk was regrinded again.

3.1.5 Pellets and rings

To make a pellet 1g and toroidal shaped ring 0.9g powders of $Bi_{1-x}Gd_xFe_{0.9}Cr_{0.1}O_3$ are taken. The polyvinyl alcohol (PVA) was mixed as a binder. Finally powders are pressed into pellet and ring using a uniaxial press.

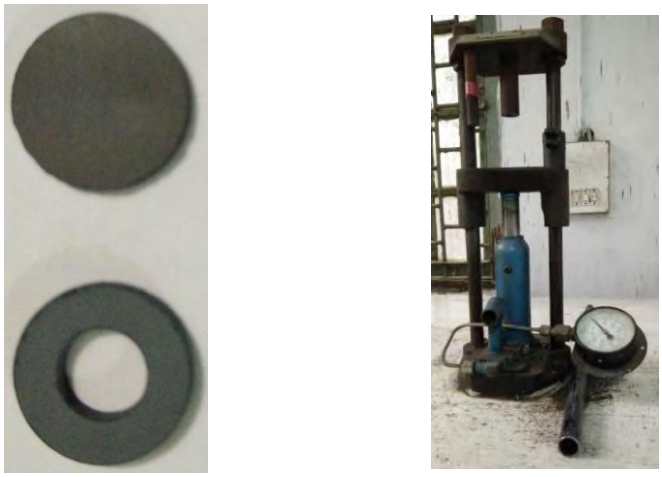

Fig. 3.1 (a) Disks and toroid shaped samples and (b) Uniaxial press machine.

3.1.6 Sintering

The pellets and rings were placed in boat and inserted into the furnace for sintering. Sintering was done at 825, 850 and 875 °C for 4 hours. The temperature rate was 10°C/min for heating and 5°C/min for cooling. The pellets and rings were then polished to have a smooth faces and both were ready to measurements.

The flow chart of sample preparation process is shown below:

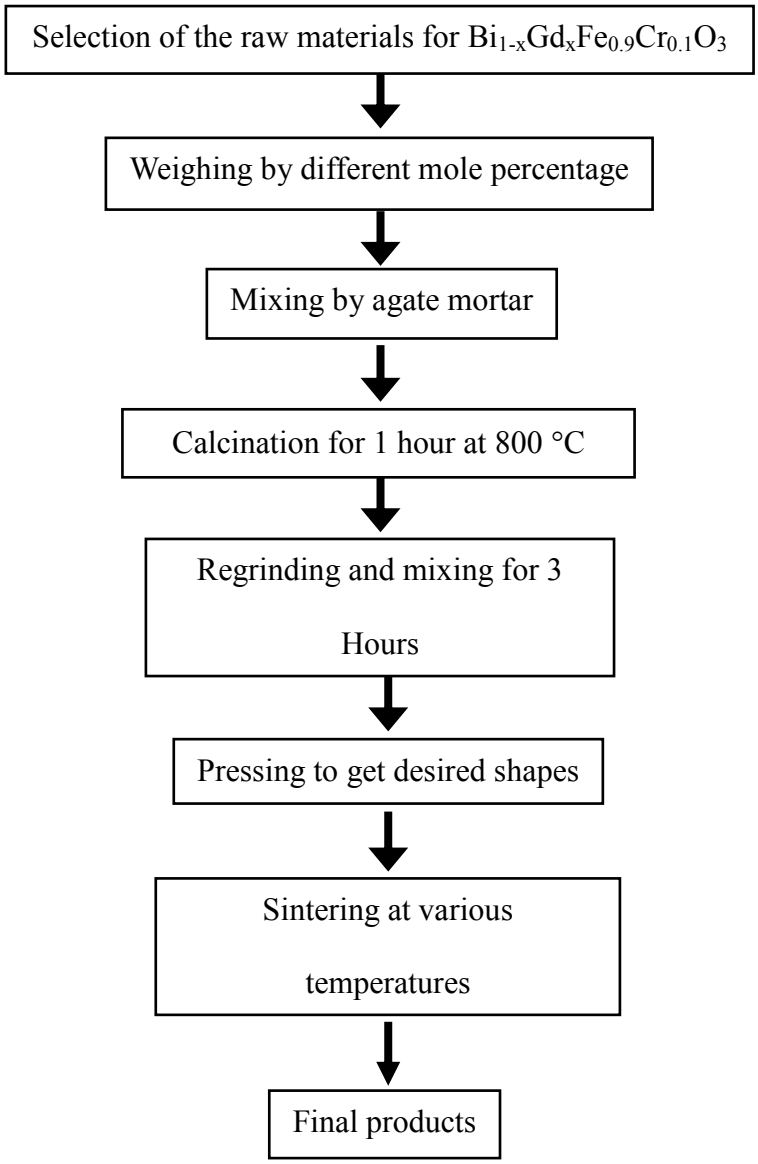

3.2 Experimental techniques

3.2.1 X-ray diffraction

The XRD technique is commonly utilized in the analytical characterization to gain crystallographic information of crystals. The main function of an XRD instrument is used to determine the phase structure, crystallographic structure and the chemical composition. Since each material possesses its own unique XRD spectra, hence qualitative and quantitative analysis can be conveniently carried out by comparing the obtained sample XRD pattern to the standard database. A wealth of information, such as lattice parameters and the particle size can also be extracted.

The phase analysis of the synthesized samples was performed using an advanced X-Ray Diffractometer model-Philips PANalytical X'PERT-PRO (Cu-Kα as a target and incident wavelength λ = 1.540598 Å radiation). The XRD is a versatile, non-destructive materials analysis method that provides detailed information about the crystallographic and microstructure of all types of natural and synthetic materials. Bragg reflection is a coherent elasting scattering in which the energy of the X-ray is not changed on reflection. If a beam of monochromatic radiation of wavelength λ is incident on a periodic crystal plane at an angle θ and is diffracted at the same angle as shown in Fig.3.1, the Bragg's diffraction condition for X-rays is given by,

$$2d \sin\theta = n\lambda \qquad (3.1)$$

where n is an integer, λ is the wavelength of the X-ray, d is the distance between the planes and θ is the angle between the incident beam and crystal plane.

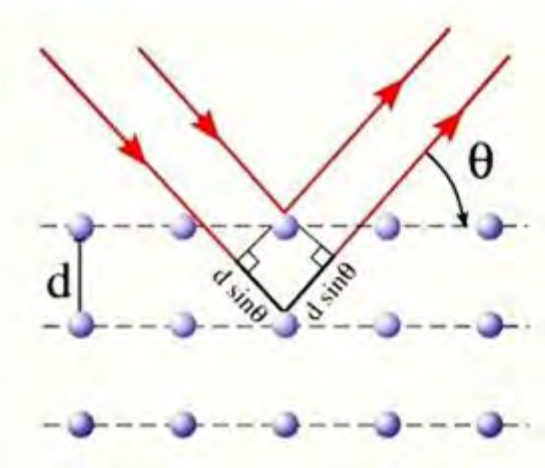

Fig. 3.2 Bragg's diffraction for X-ray.

The lattice parameter for each peak of each sample was calculated by using the formula for orthorhombic structure,

$$\frac{1}{d_{hkl}^2} = \frac{h^2}{a^2} + \frac{k^2}{b^2} + \frac{l^2}{c^2}$$

where h, k, l are the miller indices [1] of the crystal planes. A, b, c are the lattice parameters.

3.2.2 Lattice constant, density and porosity calculation

The synthesized compositions showed rhombohedral and orthorhombic structures, so the lattice parameters of the samples were calculated by using the following relations:

$$\frac{1}{d_{hkl}^2} = \frac{4}{3}\left(\frac{h^2+hk+k^2}{a^2}\right) + \frac{l^2}{c^2} \qquad (3.2)$$

$$\frac{1}{d_{hkl}^2} = \frac{h^2}{a^2} + \frac{k^2}{b^2} + \frac{l^2}{c^2} \qquad (3.3)$$

Where h, k and l are the Miller indices of the crystal planes.

The theoretical density, ρ_x was calculated using the following expression:

$$\rho_x = \frac{nM}{VN_A} \qquad (3.4)$$

Where n is the number of atom per unit cell, M is the molar mass of the sample, N_A is the Avogadro's number (6.022×10^{23}) and V is the volume of the unit cell.

The bulk density ρ_B was calculated using the relation:

$$\rho_B = \frac{m}{r^2 t} \quad (3.5)$$

Where m is the mass, r is the radius and t is the thickness of the pellet. The porosity of the samples were calculated using the formula,

$$P(\%) = \frac{(\rho_x - \rho_B)}{\rho_x} \times 100\% \quad (3.6)$$

3.2.3 Microstructural investigation

The microstructural study of the studied samples was performed in order to have an insight of the grain structures. The samples of different compositions and sintered at different temperatures were chosen for this purpose. The samples were visualized under a high-resolution optical microscope and then photographed. Average grain sizes (grain diameter) of the samples were determined from optical micrographs by linear intercept technique [2]. To do this, several random horizontal and vertical lines were drawn on the micrographs. Therefore, we counted the number of grains intersected and measured the length of the grains along the line traversed. Finally the average grain size was calculated.

3.2.4 Scanning electron microscope

The scanning electron microscope (SEM) uses a focused beam of high-energy electrons to generate a variety of signals at the surface of solid specimens. The signals that derive from electron sample interactions reveal information about the sample including external morphology (texture), chemical composition, and crystalline structure and orientation of materials making up the sample. In most applications, data are collected over a selected area of the surface of the sample, and a 2-dimensional image is generated that displays spatial variations in these properties. Areas ranging from approximately 1 cm to 5 microns in width can be imaged in a scanning mode using conventional SEM techniques

(magnification ranging from 20X to approximately 30,000X, spatial resolution of 50 to 100 nm). The SEM is also capable of performing analyses of selected point locations on the sample, this approach is especially useful in qualitatively or semi-quantitatively determining chemical compositions [3].

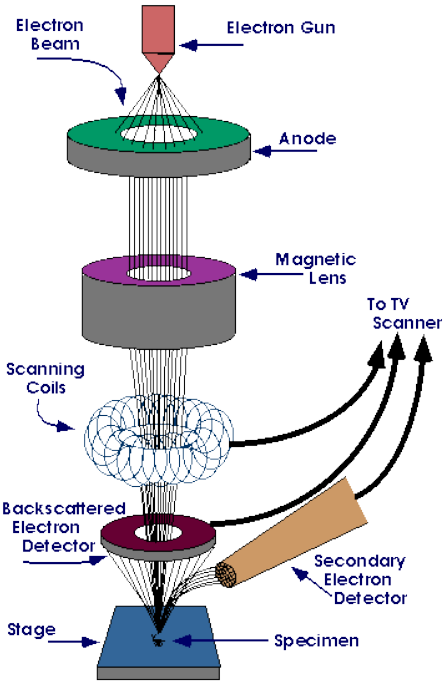

Fig. 3.3 Schematic diagram of Scanning Electron Microscope.

The surface morphology of the synthesized samples was analyzed by field emission scanning electron microscope (FESEM, JEOL JSM 7600F).

Fig. 3.4 Field emission scanning electron microscope.

3.2.5 Energy dispersive X-ray spectroscopy

Energy dispersive X-ray spectroscopy (EDX) is an analytical technique used for the elemental analysis or chemical characterization of a sample. It is one of the variants of X-ray fluorescence spectroscopy, which relies on the investigation of a sample through interactions between electromagnetic radiation and matter, analyzing X-rays that are characteristics of an element's atomic structure to be identified uniquely from one another.

An EDX is comprised of three basic components, the X-ray detector, the pulse processor and the analyzer that must be designed to work together to achieve optimum results. In practice, the X-ray detector first detects and converts X-rays into electronic signals. Then the pulse processor measures the electronic signals to determine the energy of each X-ray detected. Finally, the analyzer displays and interprets the X-ray data.

In the present work, compositional analyses were performed by using the EDX system attached with the FESEM (JEOL JSM 7600F).

3.3 Dielectric properties

3.3.1 Dielectric constant and dielectric loss

The dielectric properties, AC conductivity etc were measured using Wayne Kerr Impedance Analyzer 6500B series (shown in Fig.3.4). Measurements of dielectric properties normally involve the measurements of the change in capacitance and loss of a capacitor in presence of the dielectric materials. The behavior of a capacitance can now be described as: we assume an ideal loss less air capacitor of capacitance C_0. On insertion of a dielectric material in air space the capacitance are changed. The dielectric constant (ε'), loss tangent ($tan\delta_E$) and electrical properties measurements on disk shaped specimens were carried out at room temperature on all the samples in the high frequency range.

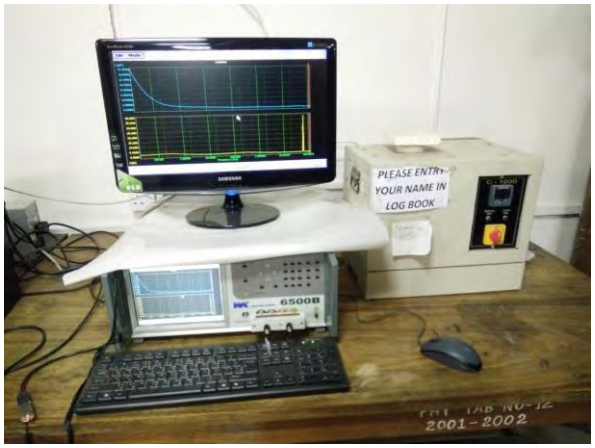

Fig. 3.5 Wayne Kerr Impedance Analyzer (Model No. 6500B) in experimental solid state physics laboratory, Department of Physics, BUET.

In order to measure dielectric properties, the pellet shaped samples were polished properly to remove roughness or contamination of any other oxides on the surface during sintering and samples were painted with conducting silver paste on both sides to ensure good electrical contacts. The dielectric parameters wre calculated using the following relations [4]:

$$\varepsilon' = \frac{C}{C_0} \tag{3.7}$$

And

$$\varepsilon'' = \varepsilon' \tan\delta_E \tag{3.8}$$

Where C is the capacitance of the dielectric materials and $C_0 = \frac{\varepsilon_0 A}{t}$ is derived geometrically. Here C_0 is the capacitance of the capacitor without the dielectric materials, ε_0 is the permittivity of free space ($\varepsilon_0 = 8.85\times10^{-12}$ Fm^{-1}) and A (= r^2) is the area of cross section of the pellet shaped sample.

3.3.2 Complex impedance spectroscopy analysis

A powerful tool to investigate the electrical properties of the complex oxides is the Complex impedance spectroscopy. AC measurements are often made with a Wheatstone-bridge-type of apparatus (impedance analyzer or LCR meter) in which the resistance R and capacitance C of the sample are measured and balanced against variable resistors and

capacitors. The impedance (Z) and the phase difference (θ) between the voltage and current are measured as a function of frequency for the given sample and the technique is called impedance spectroscopy. Then the data is analyzed by plotting the imaginary part of impedance, $Z'' = |Z|\cos\theta$ against the real part of impedance, $Z' = |Z|\sin\theta$ on a complex plane called a impedance plot. An impedance plot with linear scale is compared with the equivalent circuit proposed by brick layer model [5]. Impedance plot of a pure resistor is a point on real axis and that of a pure capacitor is a straight line coinciding with the imaginary axis. The impedance of a parallel RC combination is expressed by the following relation:

$$Z^* = Z' - jZ'' = \frac{R}{1+(\ RC)^2} - j\frac{R^2C}{1+(\ RC)^2} \qquad (3.9)$$

After simplification, one gets

$$(Z' - \frac{R}{2})^2 + (Z'')^2 = (\frac{R}{2})^2 \qquad (3.10)$$

Which represents the equation of a circle with radius $\frac{R}{2}$ and centre at $(\frac{R}{2}, 0)$. Thus a plot of Z' vs Z'' (often called Cole-Cole plot) will result in a semicircle (schematic diagram is in Fig.3.5) of radius $\frac{R}{2}$.

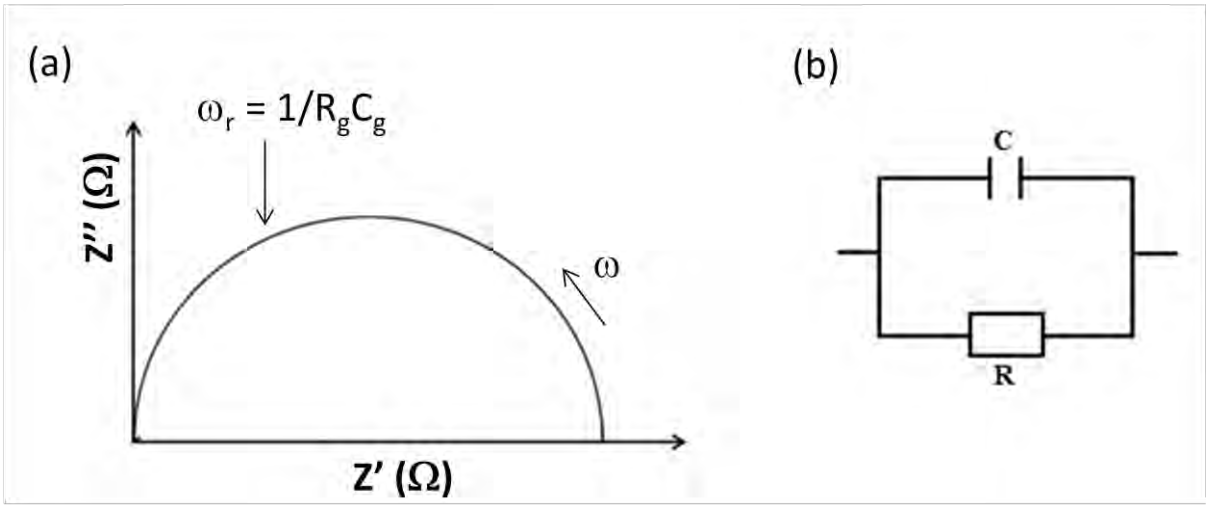

Fig. 3.6 (a) Schemetic diagram of impedance plot for a circuit of a resistor and a capacitor in parallel and (b) the corresponding equivalent circuit.

3.3.3 AC conductivity

At room temperature, the AC conductivity of the samples was determined in the frequency range 20 Hz – 10 MHz to study the mechanism of conduction. For the measurement of AC conductivity, samples were painted on both sides with silver paste to ensure good electric contacts. The AC conductivity of the sample was calculated from the dielectric data using the following relation [6]:

$$_{AC} = \varepsilon_0 \varepsilon' \tan\delta_E \quad (3.11)$$

3.4 Magnetic properties

3.4.1 Complex initial permeability measurement

We used the Wayne Kerr Impedance Analyzer 6500B series to measure permeability. The turn number of wire was 4. Self inductance L_s and quality factor Q of toroid shaped sample were directly measured from impedance analyzer with parallel connection in the frequency range of 20 Hz to 120 MHz.

Real part of permeability was calculated by using the following relation:

$$' = \frac{L_S}{L_0} \quad (3.12)$$

Where L_s is the self inductance and L_0 is the inductance of winding coil without the core. And

$$L_0 = \frac{_0 N^2 S}{\bar{d}} \quad (3.13)$$

where N = number of turns = 4, $\bar{d}$ = mean diameter = $(d_1+d_2)/2$, S = area = d×h, d = $(d_2-d_1)/2$.

Here,

d_1 = inner diameter

d_2 = outer diameter

h = thickness

Imaginary part of complex permeability was measured by using the following relation:

$$'' = \frac{'}{Q} \tag{3.14}$$

Relative quality factor (RQF) was calculated by using the formula:

$$\text{RQF} = \ '\times Q \tag{3.15}$$

And loss tangent or $tan\delta_M$ was calculated by,

$$\tan\delta_E = \frac{1}{Q} \tag{3.16}$$

3.4.2 M-H hysteresis loop measurement

M-H hysteresis loop for the synthesized samples were measured using Vibrating Sample Magnetometer (VSM) (Model no.: Micro Sense EV 9) in the Materials Science Division, Atomic Energy Centre, Dhaka. Measurement setup is shown in Fig.3.7.

Fig. 3.7 VSM machine set up at Material Science Division, Atomic Energy Centre, Dhaka.

The sample is placed inside a uniform magnetic field and it is vibrated up and down in a region surrounded by several pickup coils. The magnetic sample is thus acting as a time

varying magnetic flux, varying inside a particular region of fixed area. From Maxwell's law it is known that a time varying magnetic flux is accompanied by an electric field and the field induces a voltage in pickup coils. This alternating voltage signal is processed by a control unit system, in order to increase the signal. Therefore by detecting the induced voltage, the magnetic field dependent magnetization hysteresis curve of the material is measured.

3.4.3 Magnetoelectric coefficient

The experimental setup for the measurement of ME coefficient is shown in Fig. 3.6.

Fig. 3.8 Experimental set up for the measurement of megnetoelectric coefficient.

To measure the ME coefficient the sides of the pellet is connected with a Keithley 2000 microvoltmeter that gives the value of output voltage. The sample is then placed between two faces of an electromagnet. Here another pair of coil called Helmholtz coil is placed vertically and parallel to the faces of electromagnet. The Helmholtz coil is connected to an AC power supply and create AC magnetic field. The sides of electromagnet are connected with a DC power supply. By changing current and voltage from DC power supply

magnetic field is changed of the electromagnet and sample experience different magnetic condition. Hence output voltage is changed. ME coefficient (α_{ME}) of the present sample has been calculated using the following relation:

$$\alpha_{ME} = \left(\frac{dE}{dH}\right)H_{AC} = \frac{V_0}{h_0 d} \qquad (3.17)$$

where V_0 is the ME voltage across the sample surface and h_0 is the amplitude of the AC magnetic field and d is the thickness of the sample.

References

[1] Kittel, C., "*Introduction to solid state physics*", 7th edition, John Wiley & sons, Inc., Singapore, 1996.

[2] Hossain, A. K. M. A, "*Investigation of colossal magnetoresistance in bulk and thick film magnetites*", Ph. D. Thesis, Imperial College, London (1998).

[3] Zaky, A. A., and Hawley, R., *Dielectric Solids*, Dover, New York, 1970.

[4] Goldman, A., *Handbook of modern ferromagnetic materials*, Kulwer Acad. Pub., Boston, U.S.A., 1999.

[5] MacDonald, J. R., *Impedance spectroscopy*, Wiley-Interscience, New York, 1987.

[6] Adnan, S. B. R. S. and Mohammad, N. S., "Conductivity and dielectric studies of Li_2ZnSiO_4 ceramic electrolyte synthesized via citrate sol gel method", *Int. J. Electrochem. Sci.*, Vol. 7, pp. 9844-9858, 2012.

CHAPTER 4

RESULTS AND DISCUSSION

4.1 X-ray diffraction analysis

Fig. 4.1 shows the XRD pattern of various $Bi_{1-x}Gd_xFe_{0.9}Cr_{0.1}O_3$ samples sintered at 850°C and measured at room temperature. The structure can be indexed as a rhombohedral structure (for x = 0.00 and x = 0.05) [1, 2] and orthorhombic structure (for x = 0.10, 0.15 and 0.20) [3, 4, 5] with a large amount of impurity phases of $Bi_2Fe_4O_9$ emerging at a diffraction angle of 2θ = (28.16°–30.84°) (when x = 0.00-0.10) which also observed by Chang et al. [1]. It is observed that the impurity of $Bi_2Fe_4O_9$ is more in $Bi_{1-x}Gd_xFe_{0.9}Cr_{0.1}O_3$ when x = 0.00 and impurity gradually reduced with the increase in Gd content and only one impurity peak of $Bi_{25}FeO_{40}$ is found in the samples when x = 0.15 and 0.20 [6]. At the same time the structure changed for x = 0.10. In the first sample i.e, when x= 0.00, impurity is found more because of Cr^{3+} ions do not enter into the structure of BFO when x≥0.10 of Cr content is doped in BFO [1]. At the same time it is observed that there is another pick around 2θ = 27.74° which corresponds to the peak (201) of $Bi_{7.38}Cr_{0.62}O_{12+x}$ [1], the intensity of which also decreased with the increase in Gd content and vanishes when x = 0.15 and 0.20. Fig. 4.1(b) shows the enlarge view of (110) peak. From Fig. 4.1(b) it is seen that the XRD peaks shift toward higher angle side with increasing Gd content, but there is no indication of change in basic structure of perovskite. From the XRD pattern it is seen that the influence of Gd content in $Bi_{1-x}Gd_xFe_{0.9}Cr_{0.1}O_3$ is very significant.

Table 4.1: The lattice parameters of $Bi_{1-x}Gd_xFe_{0.9}Cr_{0.1}O_3$ compositions sintered at 850 °C.

Gd content, x	Lattice parameter (Å)		
	a (Å)	b (Å)	c (Å)
0.00	4.5973	4.5973	13.0856
0.05	4.5882	4.5882	13.0739
0.10	5.4285	5.6174	7.8044
0.15	5.4354	5.6365	7.7446
0.20	5.4157	5.6151	7.7882

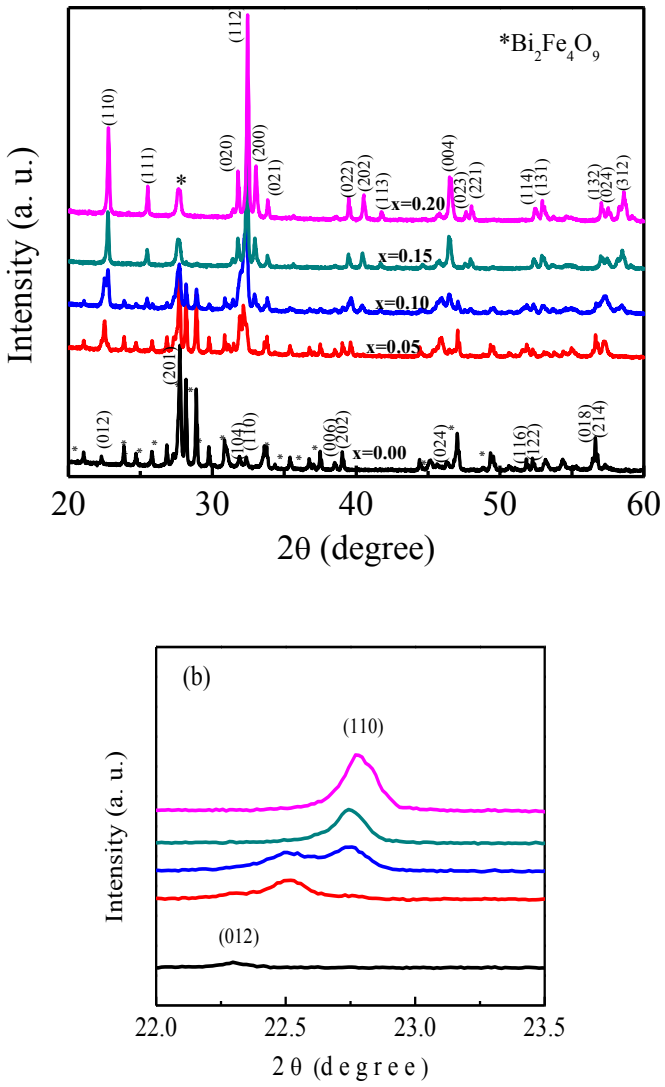

Fig. 4.1 (a) X-ray diffraction patterns of $Bi_{1-x}Gd_xFe_{0.9}Cr_{0.1}O_3$ (x= 0.00, 0.05, 0.10, 0.15 and 0.20) compositions sintered at 850 °C and (b) enlarged view of (012) peak (for x= 0.00 and 0.05) and (110) peak (for x= 0.10-0.20).

4.2 Density and porosity

The X-ray density of the composition was calculated using the relation:

$$x = \frac{nM}{N_A V} \qquad (4.1)$$

where n is the number of atoms per unit cell, M is the molecular weight of $Bi_{1-x}Gd_xFe_{0.9}Cr_{0.1}O_3$ (x = 0.00, 0.05, 0.10, 0.15 and 0.20), N_A is the Avogadro's number (6.023×10^{23}) and V is the volume of unit cell.

The bulk density was calculated using the formula:

$$_B = \frac{m}{r^2 d} \quad (4.2)$$

where m, r and d are the mass, radius and thickness of the pellet samples, respectively.

Table 4.2 X-ray density, bulk density and porosity of various $Bi_{1-x}Gd_xFe_{0.9}Cr_{0.1}O_3$ samples sintered at 850 °C.

Gd content x	$_x$ (g/cm^3)	$_B$ (g/cm^3)	P (%)
0.00	7.90	5.93	24
0.05	8.15	6.11	25
0.10	8.20	6.59	19
0.15	8.37	7.14	14
0.20	8.40	7.35	12

Fig. 4.2(a) shows the variation of bulk density, X-ray density and porosity of $Bi_{1-x}Gd_xFe_{0.9}Cr_{0.1}O_3$ compositions with x = 0.00, 0.05, 0.10, 0.15 and 0.20 sintered at 850 °C. From Fig. 4.2(a), it is seen that X-ray density ($_x$) and bulk density ($_B$) increases with the increase in Gd content but bulk density of all samples is lower than X-ray density. This may be due to the existence of some pores in the bulk samples which are formed and developed during the preparation of samples or sintering process. The density increases with the increase in Gd content because the ionic radius of Gd is smaller than Bi, this causes volume of the unit cell decreases. The porosity in ceramic samples develops from two sources: inter-granular porosity and intra-granular porosity [7]. Thus the total porosity (P) can be written as $P = P_{inter} + P_{intra}$. The bulk density ($_B$) increases with the increase in Gd content might be due to the decrease of the intragranular pores. Fig. 4.2(b) shows the variation of bulk density of the studied samples which increases with increase in sintering temperature. The maximum density (for x = 0.05, 0.10, 0.15 and 0.20) is found for the sintering temperature of 875 °C and the maximum density is found for sintering temperature of 850 °C of the sample in which x = 0.00. The density increases with sintering temperature because during the sintering process the thermal energy generates a force that drives the grain boundaries to grow over the

pores, thereby decreasing the pore volume and densify the material. At higher sintering temperature, $_B$ decreases (for x = 0.00) because the intragranular porosity is increased due to discontinuous grain growth. When the grain growth rate is high, pores may be left behind by rapidly moving grain boundaries, resulting in pores that are trapped inside the grains. The discontinuous growth of grain rises with temperature and hence contributes toward the reduction of bulk density.

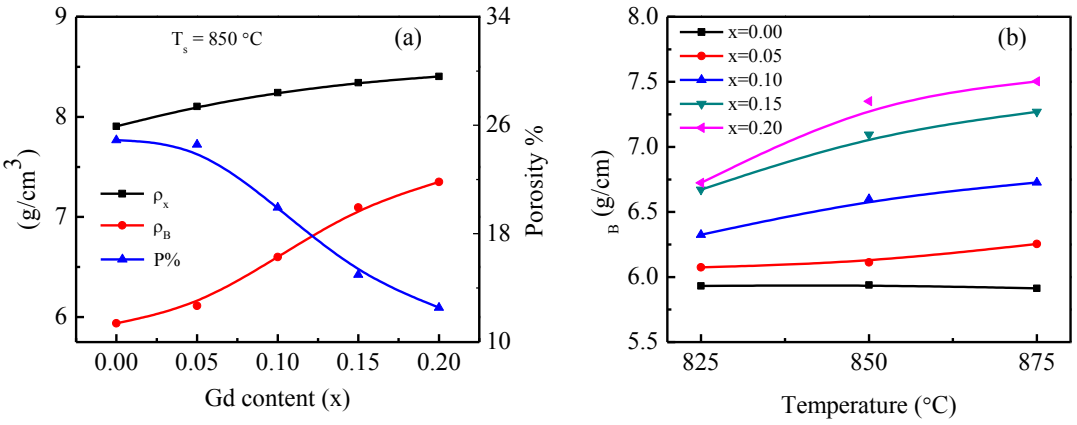

Fig. 4.2 (a) Variation of $_x$, $_B$ and porosity with Gd content and (b) variation of $_B$ with sintering temperature.

4.3 Microstructural analysis

4.3.1 Surface morphology analysis of compositions sintered at 825 °C

Microstructural features studied using Field Emission Scanning Electron Microscope (FESEM). The FESEM microstructure of the samples $Bi_xGd_{1-x}Fe_{0.9}Cr_{0.1}O_3$ (x = 0.00, 0.05, 0.10, 0.15 and 0.20) sintered at 825 °C is shown in Fig. 4.3. It is clear from the micrographs that the grain size decreased with increasing Gd content. It means that Gd doping can suppress grain growth and lead to small grain size in the materials. The grain size decreases due to smaller ionic radius of Gd^{3+} than that of Bi^{3+} [8].

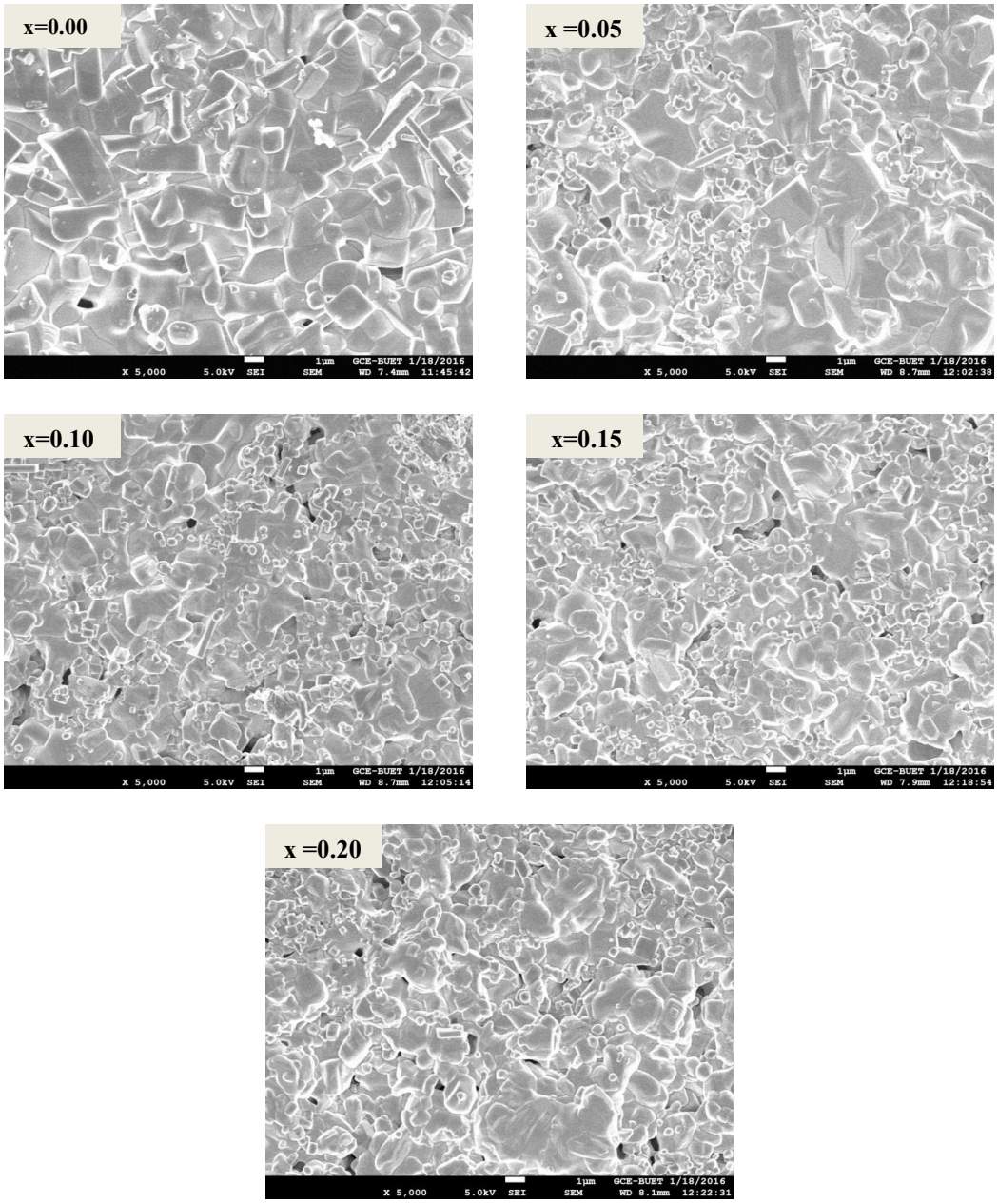

Fig. 4.3 The microstructure of various $Bi_{1-x}Gd_xFe_{0.9}Cr_{0.1}O_3$ compositions sintered at 825 °C.

The average grain size was calculated using the linear intercept technique [9]. The average grain size of various $Bi_xGd_{1-x}Fe_{0.9}Cr_{0.1}O_3$ compositions is shown in Table 4.3 sintered at 825 °C.

Table 4.3: Grain size of the compositions $Bi_xGd_{1-x}Fe_{0.9}Cr_{0.1}O_3$ sintered at 825 °C.

Gd content, x	0.00	0.05	0.10	0.15	0.20
Grain size (μm)	1.51	1.25	0.98	0.96	0.92

4.3.2 Surface morphology analysis of compositions sintered at 850 °C

The microstructure of the samples $Bi_xGd_{1-x}Fe_{0.9}Cr_{0.1}O_3$ (x = 0.00, 0.05, 0.10, 0.15 and 0.20) sintered at 850 °C is shown in Fig. 4.4. . It is seen from the micrographs that the grain size decreases with increase in Gd content. The average grain size was calculated using the linear intercept technique [9].

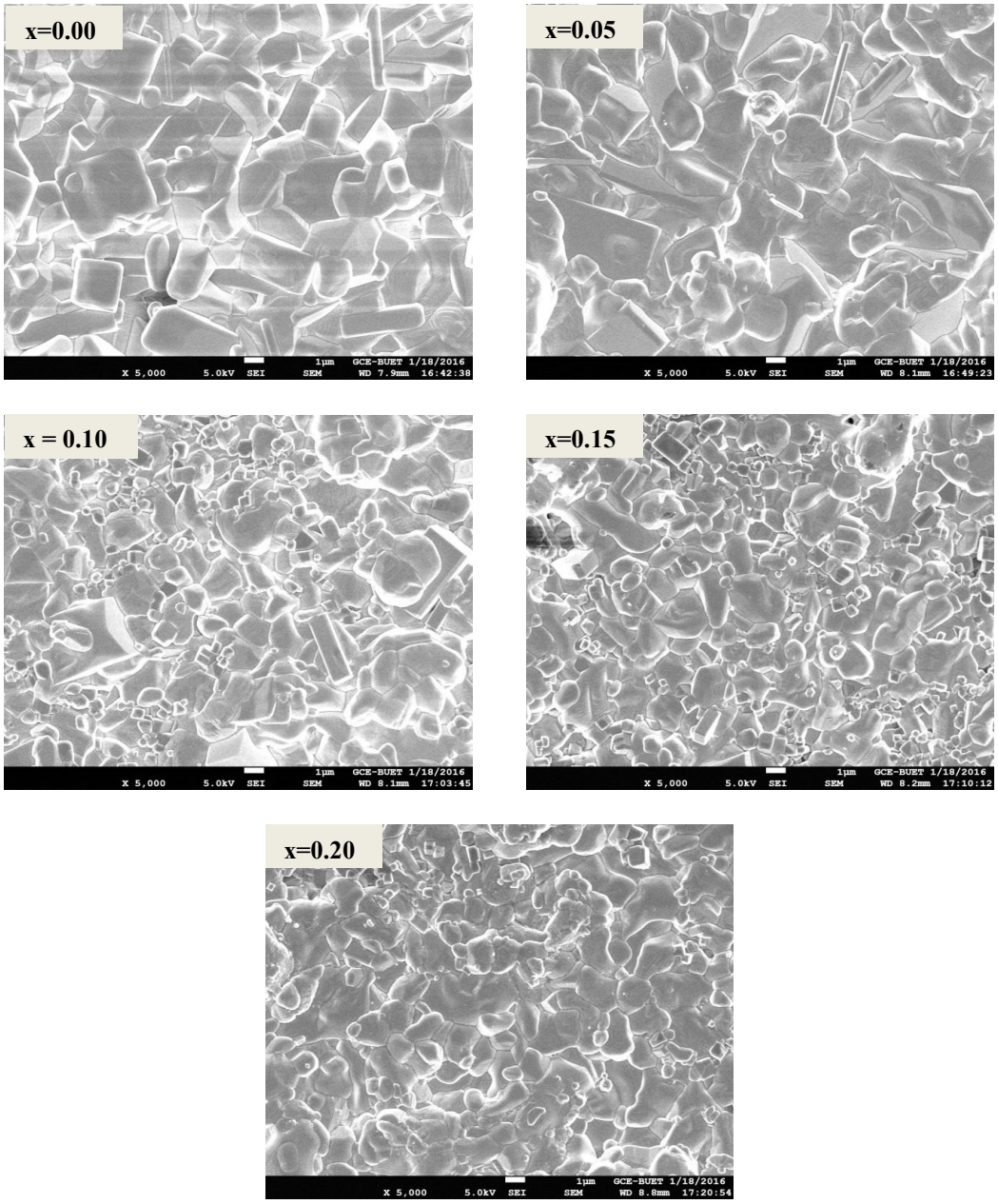

Fig. 4.4 The microstructure of various $Bi_{1-x}Gd_xFe_{0.9}Cr_{0.1}O_3$ compositions sintered at 850 °C.

The average grain size of various $Bi_xGd_{1-x}Fe_{0.9}Cr_{0.1}O_3$ compositions is shown in Table 4.4 sintered at 850 °C.

Table 4.4: Grain size of the compositions $Bi_xGd_{1-x}Fe_{0.9}Cr_{0.1}O_3$ sintered at 850 °C.

Gd content, x	0.00	0.05	0.10	0.15	0.20
Grain size (μm)	1.97	1.93	1.46	1.31	1.29

4.3.3 Surface morphology analysis of compositions sintered at 875 °C

The microstructure of the samples $Bi_xGd_{1-x}Fe_{0.9}Cr_{0.1}O_3$ (x = 0.05, 0.10, 0.15 and 0.20) sintered at 875 °C is shown in Fig. 4.5. It is clear from the micrographs that the grain size decreased with increasing Gd content may be due to the suppression of grain growth. The average grain size was calculated using the linear intercept technique [9]. The average grain size of various $Bi_xGd_{1-x}Fe_{0.9}Cr_{0.1}O_3$ compositions was shown in Table 4.5 sintered at 875°C.

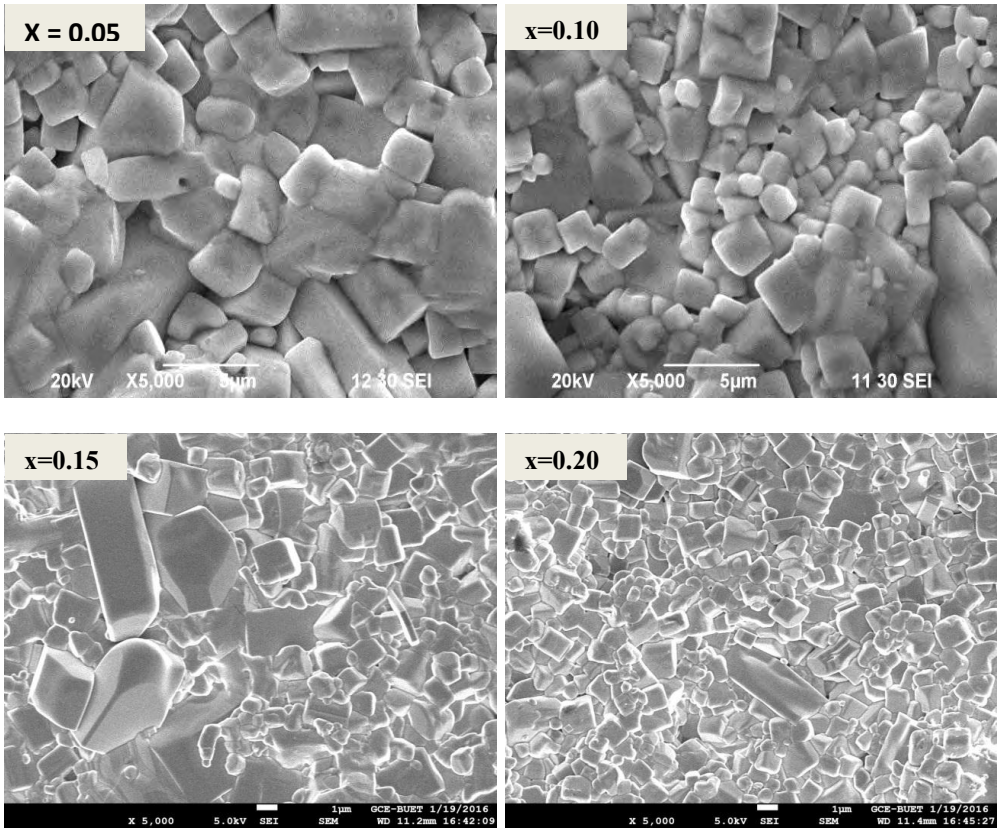

Fig. 4.5 The microstructure of various $Bi_{1-x}Gd_xFe_{0.9}Cr_{0.1}O_3$ compositions sintered at 875 °C.

Table 4.5: Grain size of the compositions $Bi_xGd_{1-x}Fe_{0.9}Cr_{0.1}O_3$ sintered at 875 °C.

Gd content, x	0.05	0.10	0.15	0.20
Grain size (μm)	2.07	1.64	1.36	0.97

4.3.4 Surface morphology with various sintering temperatures

SEM micrographs of polycrystalline $Bi_{0.85}Gd_{0.15}Fe_{0.9}Cr_{0.1}O_3$ sintered at various temperatures are shown in Fig. 4.6. It can be observed from the figure that the microstructure of the sample sintered at low temperature (825 °C) is heterogeneous where as the microstructure of the sample become homogeneous at higher sintering temperature (875 °C). It is also observed that the grain size increases with increasing sintering temperature. Further it may be noticed that the porosity of the samples sintered at 825° is predominately intergranular, whereas the porosity of the samples sintered at higher temperature is located at grain boundaries and many of the very small pores disappear through diffusion kinetics. That's why the grain size increases and the number of grain boundary decreases and consequently the porosity decreases and results in the homogeneous grain size distribution.

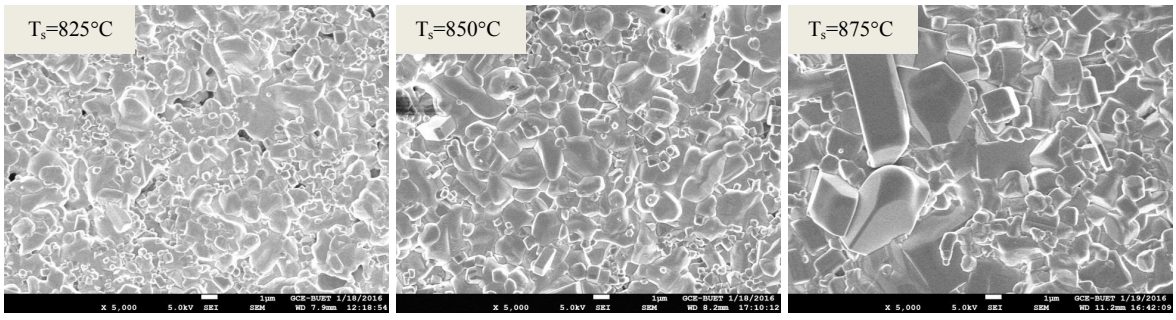

Fig. 4.6 The microstructure of $Bi_{0.85}Gd_{0.15}Fe_{0.9}Cr_{0.1}O_3$ composition sintered at various temperatures.

4.4 EDX analysis

The energy dispersive X-ray spectroscopy (EDX) of the compositions $Bi_xGd_{1-x}Fe_{0.9}Cr_{0.1}O_3$ (x = 0.00, 0.05, 0.10, 0.15 and 0.20) sintered at 850 °C is shown in Fig. 4.7-4.11. EDX analysis is used to know the amount of the starting element in the sample. The

EDX confirms the Gd doping in the composition. EDX spectroscopy also confirms the homogeneous distribution of the constituent elements.

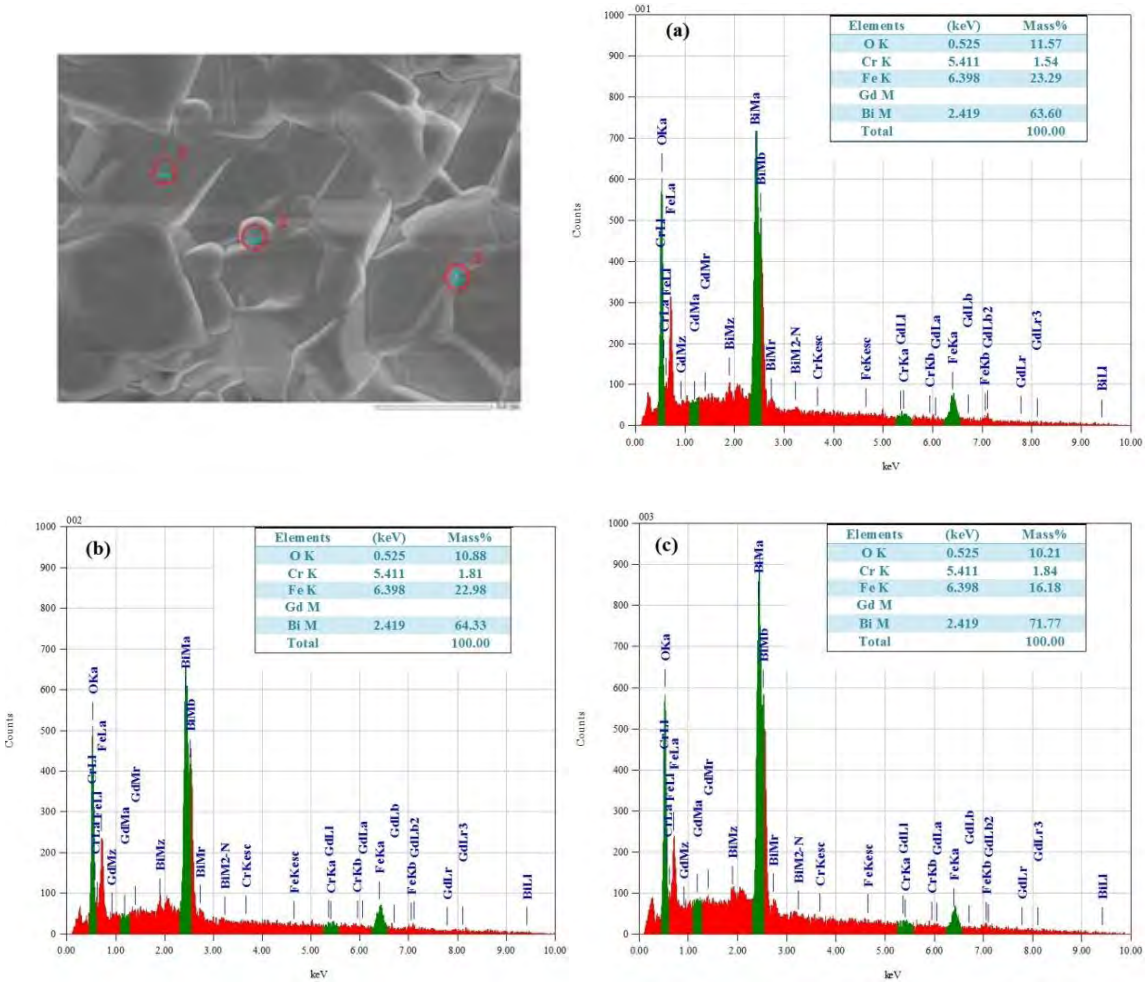

Fig. 4.7 EDX spectrum of $Bi_{1-x}Gd_xFe_{0.9}Cr_{0.1}O_3$ samples sintered at 850 °C with x = 0.00.

Table 4.6: Calculated % of mass of elements in $Bi_{1-x}Gd_xFe_{0.9}Cr_{0.1}O_3$ with x = 0.00.

Composition	Elements	Calculated % of mass
$Bi_{1-x}Gd_xFe_{0.9}Cr_{0.1}O_3$ (x = 0.00)	Bi	66.89
	Gd	0
	Fe	16.09
	Cr	1.66
	O	15.36
Total		100.00

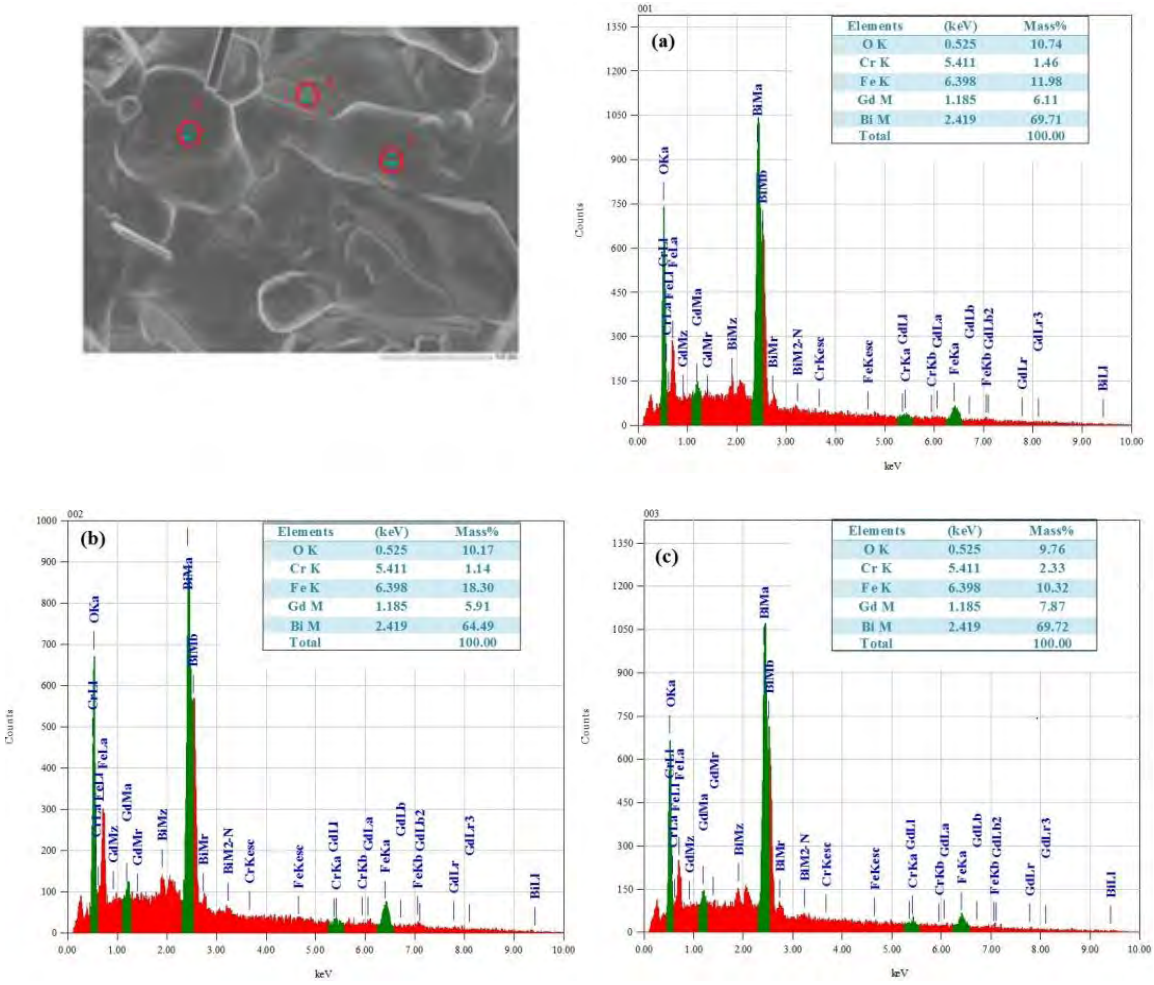

Fig. 4.8 EDX spectrum of $Bi_{1-x}Gd_xFe_{0.9}Cr_{0.1}O_3$ samples sintered at 850 °C with x = 0.05.

Table 4.7: Calculated % of mass of elements in $Bi_{1-x}Gd_xFe_{0.9}Cr_{0.1}O_3$ with x = 0.05.

Composition	Elements	Calculated % of mass
$Bi_{1-x}Gd_xFe_{0.9}Cr_{0.1}O_3$ (x = 0.05)	Bi	64.08
	Gd	2.53
	Fe	16.23
	Cr	1.67
	O	15.49
Total		100.00

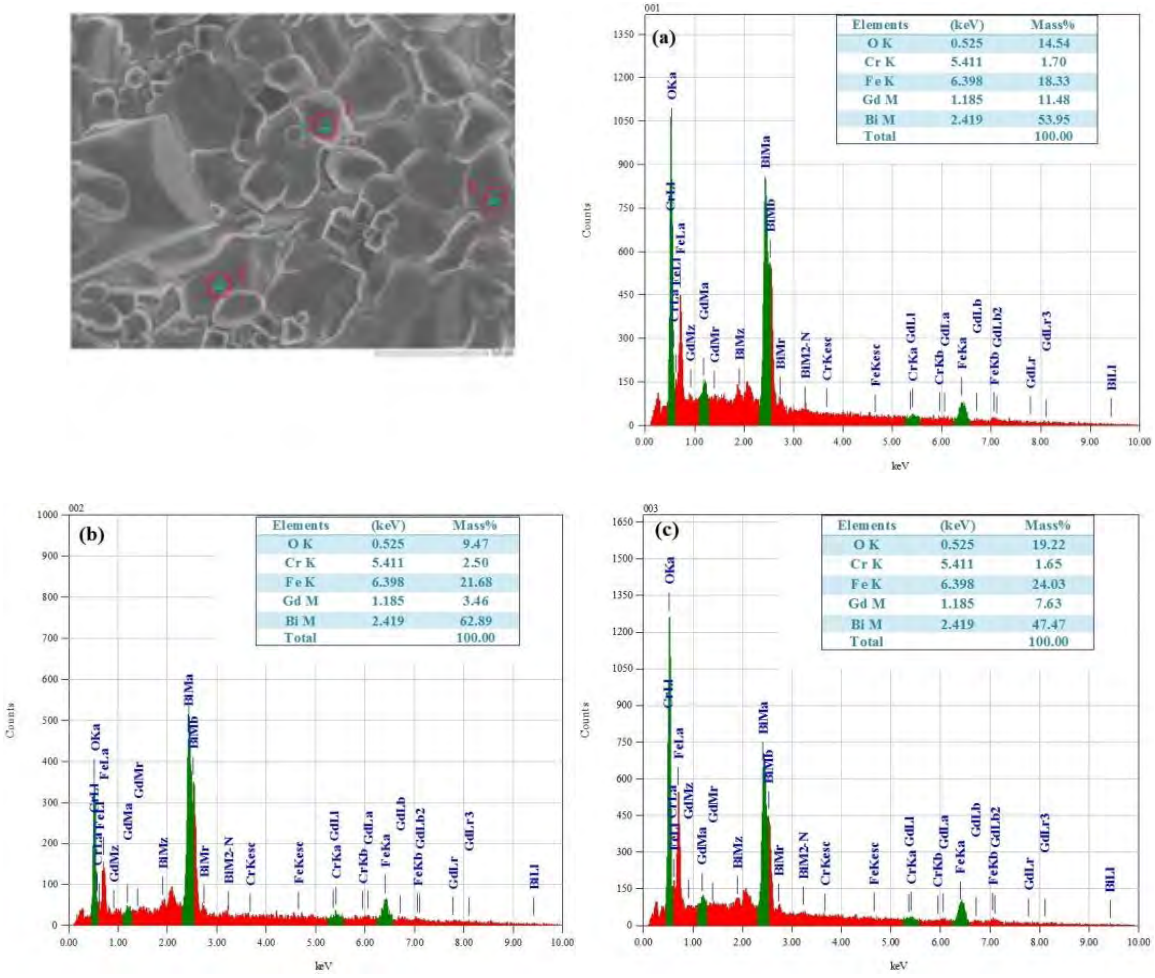

Fig. 4.9 EDX spectrum of $Bi_{1-x}Gd_xFe_{0.9}Cr_{0.1}O_3$ samples sintered at 850 °C with x = 0.10.

Table 4.8: Calculated % of mass of elements in $Bi_{1-x}Gd_xFe_{0.9}Cr_{0.1}O_3$ with x = 0.10.

Composition	Elements	Calculated % of mass
$Bi_{1-x}Gd_xFe_{0.9}Cr_{0.1}O_3$ (x = 0.10)	Bi	61.21
	Gd	5.12
	Fe	16.36
	Cr	1.69
	O	15.62
Total		100.00

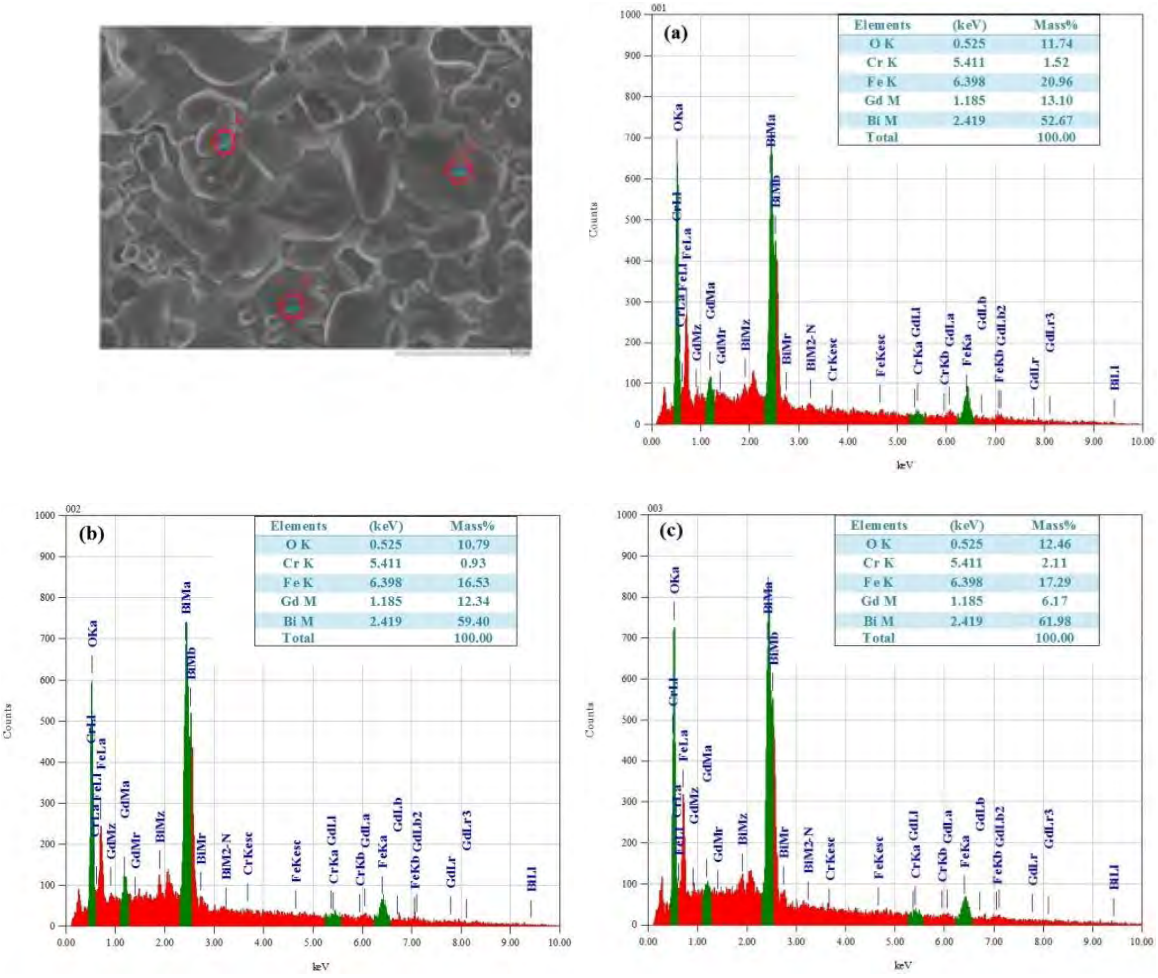

Fig. 4.10 EDX spectrum of $Bi_{1-x}Gd_xFe_{0.9}Cr_{0.1}O_3$ samples sintered at 850 °C with x = 0.15.

Table 4.9: Calculated % of mass of elements in $Bi_{1-x}Gd_xFe_{0.9}Cr_{0.1}O_3$ with x = 0.15.

Composition	Elements	Calculated % of mass
$Bi_{1-x}Gd_xFe_{0.9}Cr_{0.1}O_3$ (x = 0.15)	Bi	58.30
	Gd	7.74
	Fe	16.50
	Cr	1.71
	O	15.75
Total		100.00

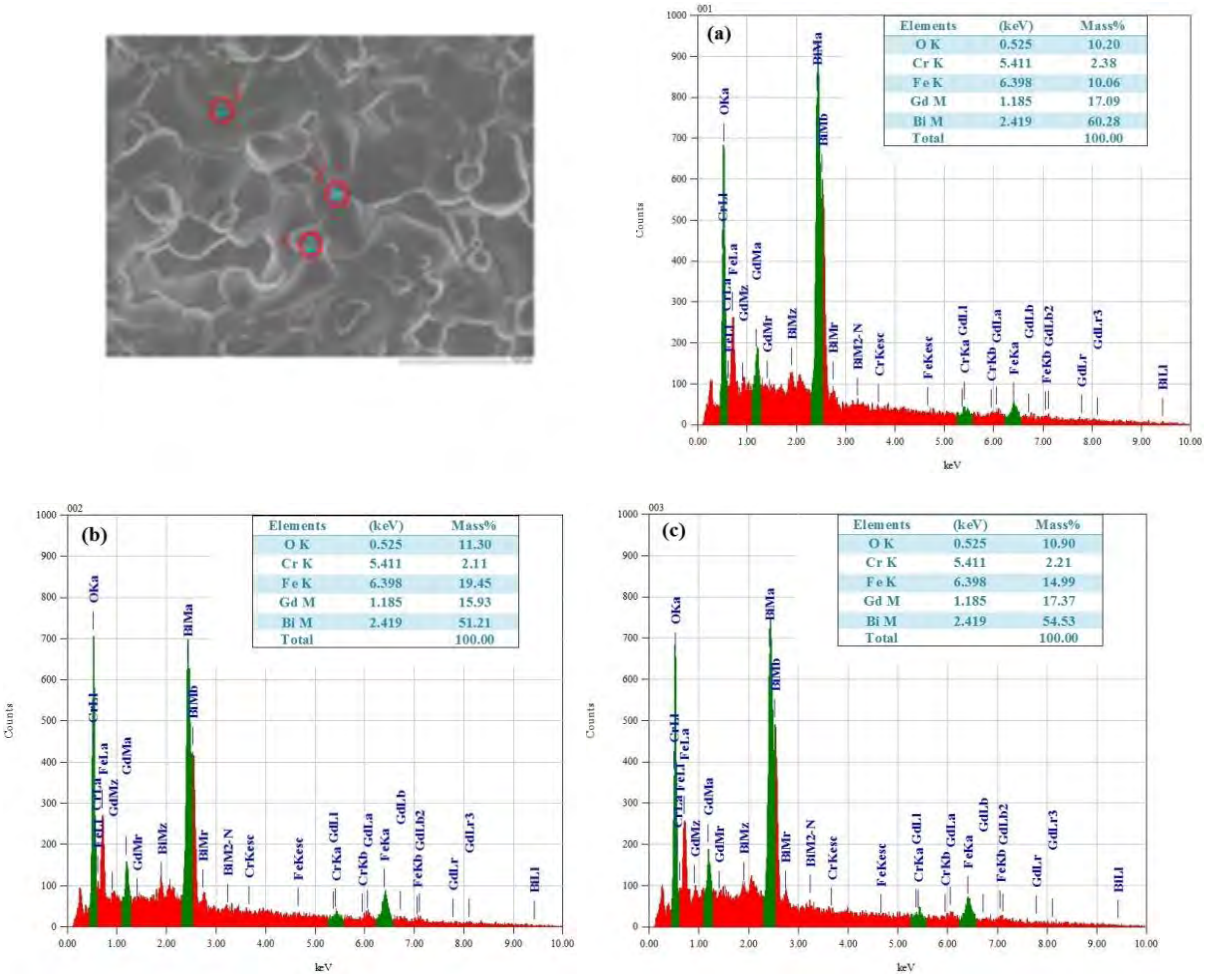

Fig. 4.11 EDX spectrum of $Bi_{1-x}Gd_xFe_{0.9}Cr_{0.1}O_3$ samples sintered at 850 °C with x = 0.20.

Table 4.10: Calculated % of mass of elements in $Bi_{1-x}Gd_xFe_{0.9}Cr_{0.1}O_3$ with x = 0.20.

Composition	Elements	Calculated % of mass
$Bi_{1-x}Gd_xFe_{0.9}Cr_{0.1}O_3$ (x = 0.20)	Bi	55.34
	Gd	10.41
	Fe	16.64
	Cr	1.72
	O	15.89
Total		100.00

Table 4.11: Bulk density ($_B$), X-ray density ($_x$), Porosity (P), percentage of constituent elements and Average grain size of $Bi_{1-x}Gd_xFe_{0.9}Cr_{0.1}O_3$ compositions.

Sintering temperature (°C)	Gd content (x)	$_B$ (g/cm^3)	$_x$ (g/cm^3)	P (%)	% of constituent elements (from EDX)					Calculated % of elements					Average grain size (μm)
					Bi	Gd	Fe	Cr	O	Bi	Gd	Fe	Cr	O	
825	0.00	5.93	7.90	24	68.57	0.00	18.81	1.73	10.88	66.89	0.00	16.09	1.66	15.36	1.51
	0.05	6.07	8.15	25	65.97	6.63	15.53	1.64	10.22	64.08	2.53	16.23	1.67	15.49	1.25
	0.10	6.32	8.20	22	60.77	7.52	16.35	1.95	13.41	61.21	5.12	16.36	1.69	15.62	0.98
	0.15	6.67	8.37	20	58.02	10.54	18.26	1.52	11.66	58.30	7.74	16.50	1.71	15.75	0.96
	0.20	6.72	8.40	19	55.34	16.80	14.83	2.23	10.80	55.34	10.41	16.64	1.72	15.89	0.92
850	0.00	5.93	7.90	24	68.57	0.00	18.81	1.73	10.88	66.89	0.00	16.09	1.66	15.36	1.97
	0.05	6.11	8.15	25	65.97	6.63	15.53	1.64	10.22	64.08	2.53	16.23	1.67	15.49	1.93
	0.10	6.59	8.20	19	60.77	7.52	16.35	1.95	13.41	61.21	5.12	16.36	1.69	15.62	1.46
	0.15	7.14	8.37	14	58.02	10.54	18.26	1.52	11.66	58.30	7.74	16.50	1.71	15.75	1.31
	0.20	7.35	8.40	12	55.34	16.80	14.83	2.23	10.80	55.34	10.41	16.64	1.72	15.89	1.29
875	0.00	5.91	7.90	25	68.57	0.00	18.81	1.73	10.88	66.89	0.00	16.09	1.66	15.36	_
	0.05	6.25	8.15	23	65.97	6.63	15.53	1.64	10.22	64.08	2.53	16.23	1.67	15.49	2.07
	0.10	6.72	8.20	17	60.77	7.52	16.35	1.95	13.41	61.21	5.12	16.36	1.69	15.62	1.64
	0.15	7.27	8.37	13	58.02	10.54	18.26	1.52	11.66	58.30	7.74	16.50	1.71	15.75	1.36
	0.20	7.50	8.40	10	55.34	16.80	14.83	2.23	10.80	55.34	10.41	16.64	1.72	15.89	0.97

4.5 Dielectric properties

4.5.1 Dielectric constant

4.5.1.1 Real part of dielectric constant

The dielectric constant was measured by using the wayne kerr Impedance analyzer (Model 6500B). The samples were painted with silver paste to ensure good electric contacts. The real part of dielectric constant (ε') was calculated by using the formula:

$$\varepsilon' = \frac{Cd}{\varepsilon_0} \qquad (4.3)$$

Where, C is the capacitance of pallet, d is the thickness of pallet, A is the cross-sectional area of the flat surface of the pallet and ε_0 is the permittivity of the free space ($\varepsilon_0 = 8.85\times10^{-12}$ F/m). The imaginary part of the dielectric constant (ε'') was calculated by using the formula:

$$\varepsilon'' = \varepsilon' tan\delta_E \qquad (4.4)$$

Where $\tan\delta_E$ is the loss tangent or the dissipation factor. Fig. 4.12 shows the frequency dependent ε' of various $Bi_{1-x}Gd_xFe_{0.9}Cr_{0.1}O_3$ compositions measured at room temperature. From Fig. 4.12, it can be seen that all the samples display a decreasing trend in ε' with frequency increasing from 100 Hz to 10 MHz. This observation can be explained by the phenomenon of dipole relaxation process, the dipoles are able to follow the frequency of the applied field at low frequencies, while they are incapable of following the frequency of the applied field at high frequencies [10]. Also at low frequency different types of polarizations (dipolar, interfacial, ionic, electric) contribute to the dielectric constant. But as the frequency increases beyond a certain limit, dipoles are not able to align themselves with the applied electric field and contribution from different polarizations ceases. Only electronic polarization has a significant contribution to the dielectric constant at higher frequency and subsequently the dielectric constant decrease. The sharp decrease in the values of ε' at lower

frequencies can be understood on the basis of Maxwell-Wagner two layer model [11] in agreement with Koop's phenomenological theory [12]. Accordingly, the dielectric structure of a material is made up of well conducting layer of grains followed by poorly conducting layer of grain boundaries. The high value of dielectric constant comes from the space charge polarization produced at the grain boundary. The polarization mechanism involves the exchange of electrons between the ions of the same element, which are present in more than one valence state and are distributed randomly over crystallographic equivalent sites. Here the exchange of electrons mainly takes place between Fe^{3+}–Fe^{2+} present at octahedral sites (B-site). During this exchange mechanism the electrons have to pass through the grains and grain boundary of the dielectric medium. Owing to high resistance of the grain boundary, the electrons accumulate at the grain boundary and produce space charge polarization. It is well known that the grain boundaries are more effective at low frequency and grains are effective at high frequency [12, 13]. Hence due to the grain boundary affect the dielectric constant decreases rapidly in the low frequency region. At high frequency the grains come into action and also the hopping of electrons cannot follow the high frequency ac field, thus resulting in a decrease in polarization. Consequently, the dielectric constant remains small and constant. The dielectric behavior of $Bi_{1-x}Gd_xFe_{0.9}Cr_{0.1}O_3$ ceramics might be understood in terms of oxygen vacancy and the displacement of Fe^{3+} ions. A charge imbalance is created due to volatilization Bi^{3+} and the reduction of Fe^{3+} during the sintering process and thus creates oxygen vacancies. These oxygen vacancies are responsible for the reduction of dielectric properties of BFO [14]. Substitution of Gd^{3+} in Bi site, imbalance of Bi^{3+} and Fe^{3+} is compensated. Hence oxygen vacancies are reduced when Gd is doped in BFO. The decrease of oxygen vacancies results in improvement of the dielectric properties. It can be seen from Fig. 4.12 that the ε' of Gd undoped sample is lower than that of the Gd-doped in the measured range of 100 Hz–10 MHz, it means that the dielectric property of $BiFe_{0.9}Cr_{0.1}O_3$

can be improved greatly after being doped with Gd in Bi site, which reaches a maximum value for x=0.20 sintered at 875 °C temperature. The dielectric constant measured at 1 MHz reaches 227 when x = 0.20, (sintered at 875 °C) which is 4.8 times as big as that of the composition $Bi_{1-x}Gd_xFe_{0.9}Cr_{0.1}O_3$ when x = 0.05.

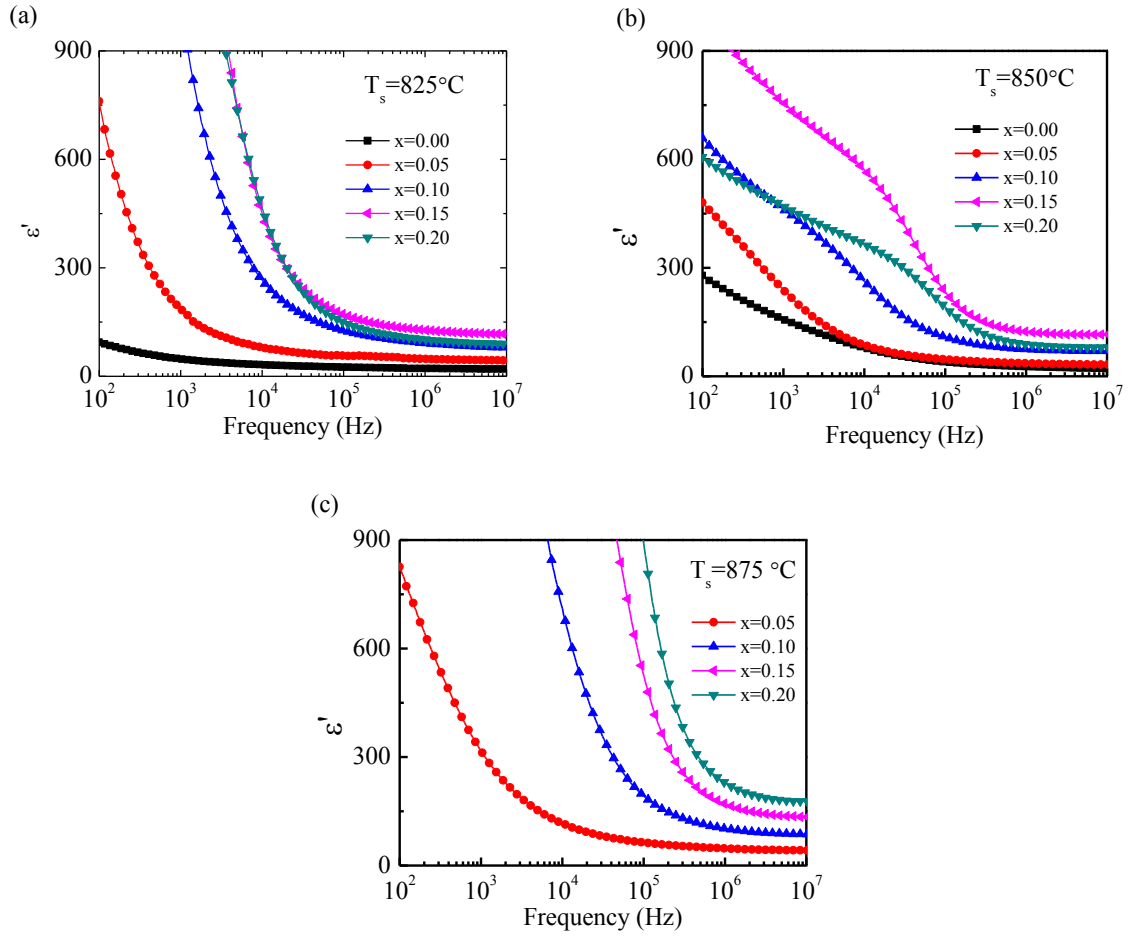

Fig. 4.12 Frequency dependent real part of complex dielectric constant of various $Bi_xGd_{1-x}Fe_{0.9}Cr_{0.1}O_3$ sintered at different temperature.

4.5.1.2 Imaginary part of dielectric constant

Fig. 4.13 shows the variation of the ε″ of the compositions $Bi_xGd_{1-x}Fe_{0.9}Cr_{0.1}O_3$ sintered at different temperatures, which shows similar behavior as dielectric constant. It is observed that the ε″ decreases with the increase in frequency and merges at higher frequencies.

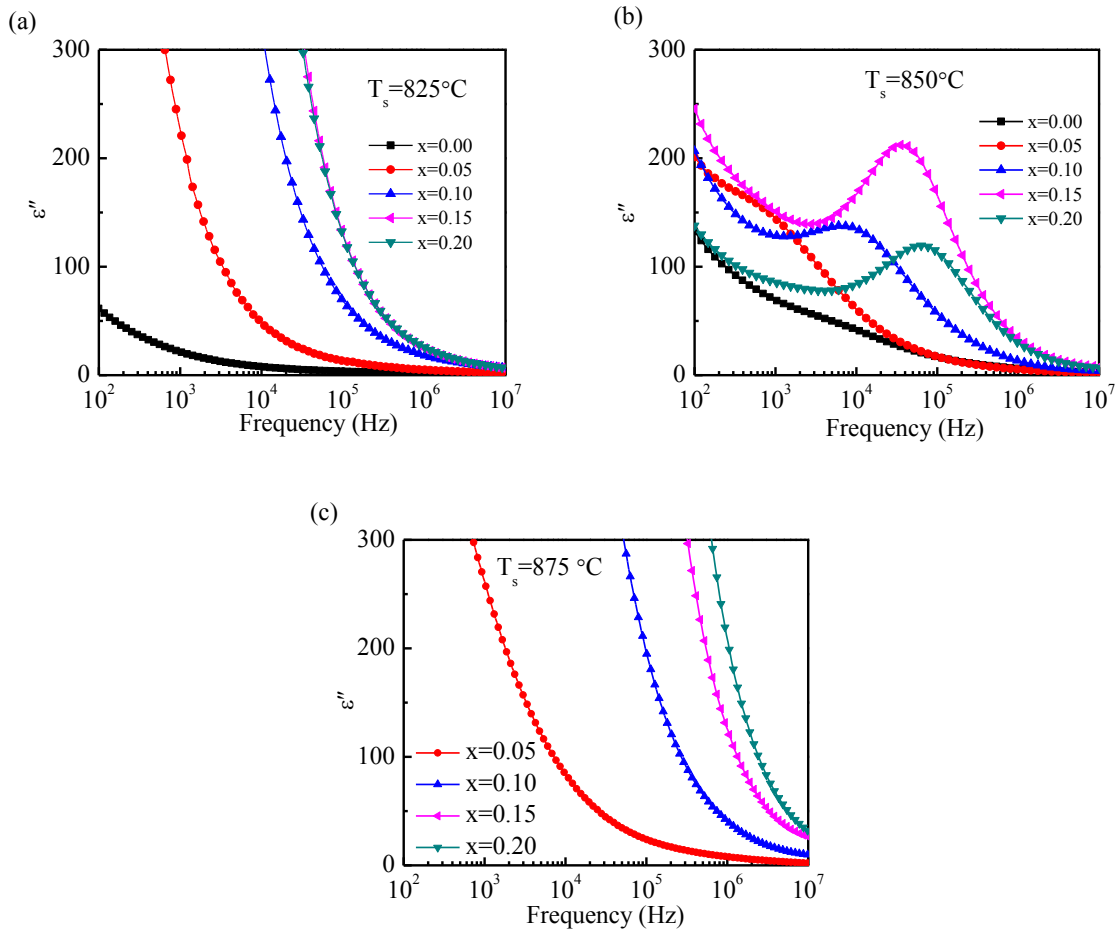

Fig. 4.13 Frequency dependent imaginary part of complex dielectric constant of various $Bi_xGd_{1-x}Fe_{0.9}Cr_{0.1}O_3$ sintered at different temperatures.

4.5.2 Dielectric loss

Fig. 4.14. shows the variation of dielectric loss of various $Bi_xGd_{1-x}Fe_{0.9}Cr_{0.1}O_3$ compositions sintered at different temperatures. From Fig. 4.14, it can be seen that for all the samples there is a pick. This pick indicates the relaxor behavior of the compositions. The width of the pick of Gd undoped sample is larger than the doped samples and at higher frequency (>10 MHz) the dielectric loss is smaller of Gd doped $Bi_{1-x}Gd_xFe_{0.9}Cr_{0.1}O_3$ than that of undoped $BiFe_{0.9}Cr_{0.1}O_3$, which means the compositions could possibly be used in practical applications such as magnetically tunable filters and oscillators. This loss factor is attributed to domain wall resonance. At high frequencies, the dielectric loss is low due to the inhibition of domain wall motion. The dielectric loss is found to be maximum in the frequency range

1 kHz–1 MHz. The maximum dielectric loss is observed when the hopping frequency of electrons between different ionic sites becomes nearly equal to the frequency of the applied field [15].

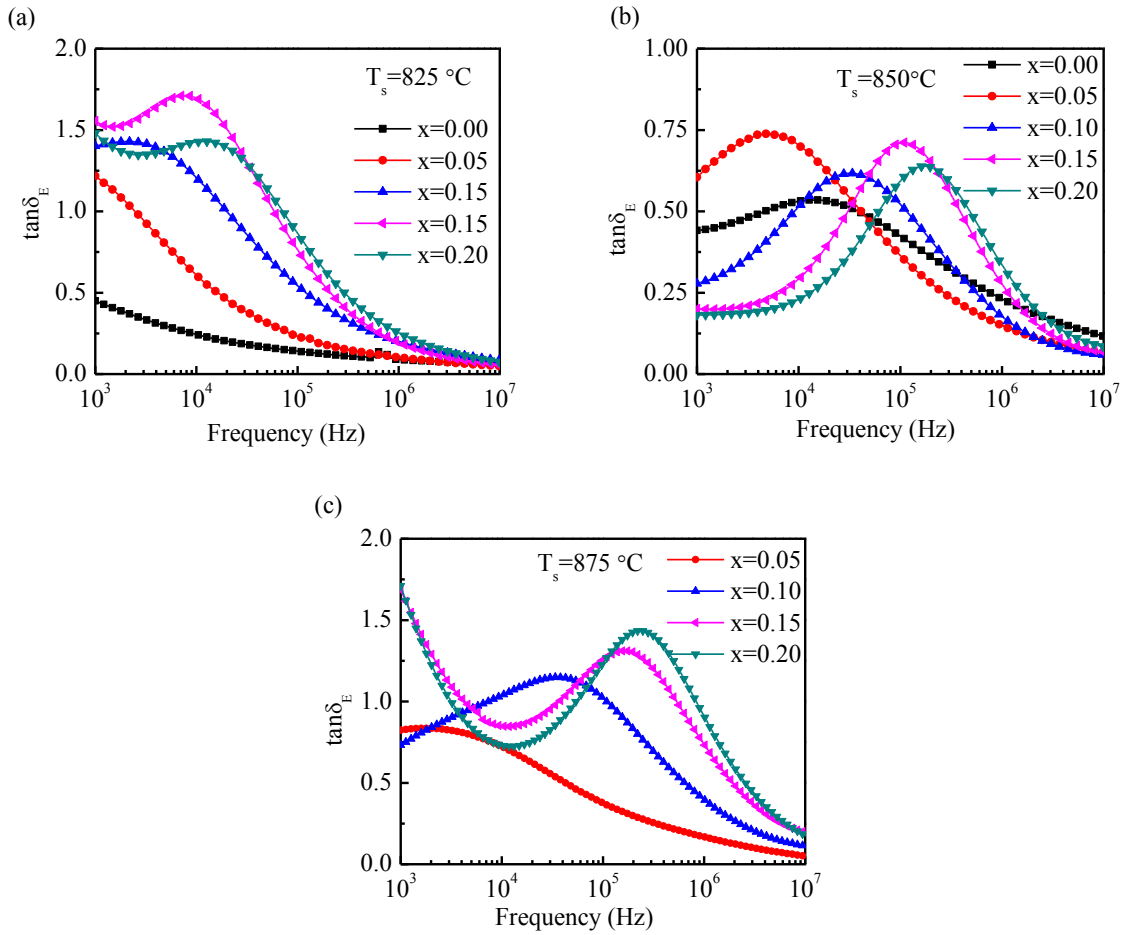

Fig. 4.14 Frequency dependent dielectric loss of various $Bi_xGd_{1-x}Fe_{0.9}Cr_{0.1}O_3$ sintered at different temperature.

4.6 Complex impedance spectra analysis

4.6.1 Real part of complex impedance

The variation of the real part (Z') of complex impedance as function of frequency for $Bi_{1-x}Gd_xFe_{0.9}Cr_{0.1}O_3$ sintered at 825, 850 and 875 °C for 4 h is shown in Fig. 4.15 (a), (b) and (c) respectively. It is observed that the value of Z' decreases with the increase in frequency. The decrease in Z' can be attributed to the increase in conduction mechanism due to hopping of electrons, which increases with increasing frequency of the applied field [16].

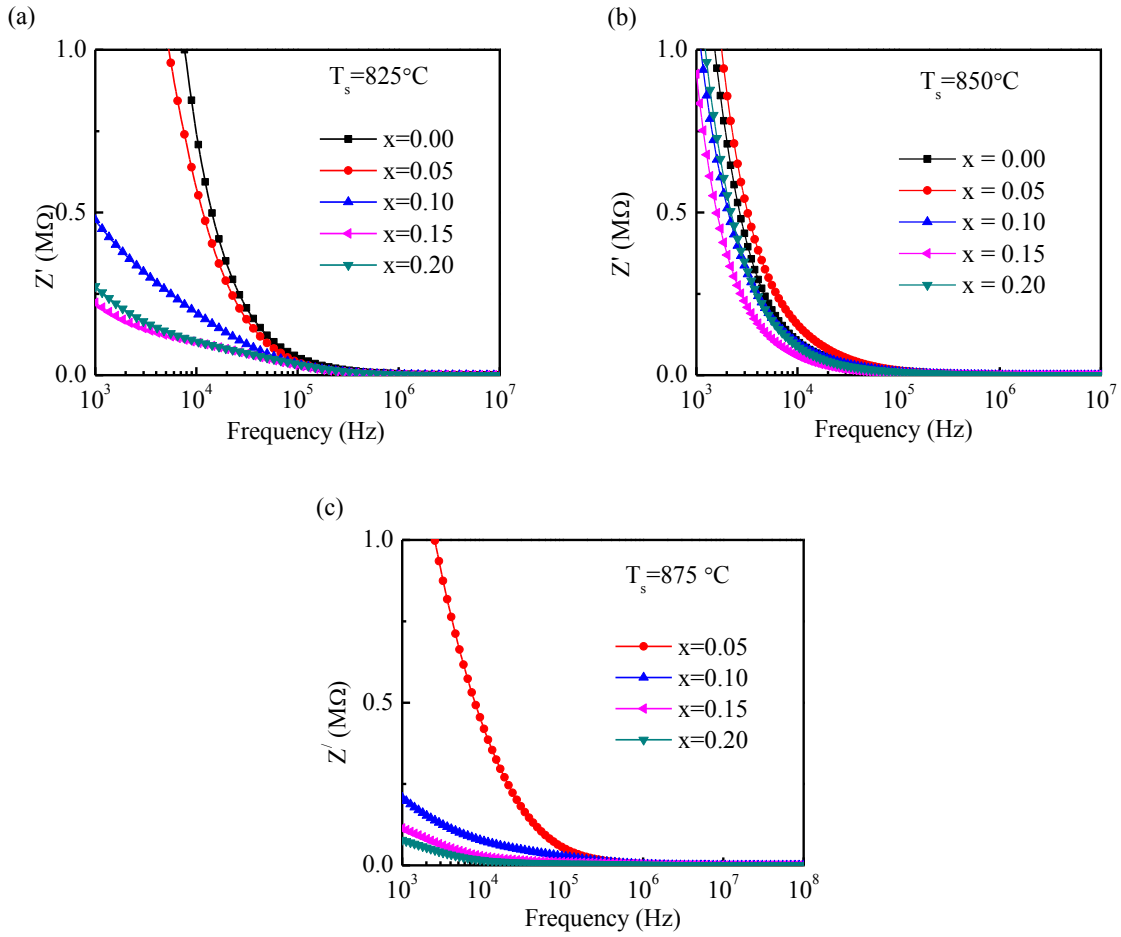

Fig. 4.15 Variation of the real part (Z') of complex impedance with frequency of $Bi_{1-x}Gd_xFe_{0.9}Cr_{0.1}O_3$ sintered at (a) 825, (b) 850 and (c) 875 °C for 4 h.

The decreasing value of Z' means that the loss in resistive property of the samples. Such a behavior is expected due to the presence of space charge polarization in a material. The merger of Z' at higher frequency is ascribed to the release of space charges. These regions are linked to the conducting behavior of charge carrier inside the material and have a very similar shape to that of ac conductivity. Also we observed that the value of impedance is higher in Gd undoped sample than the doped samples.

4.6.2 Imaginary part of complex impedance

Fig. 4.16 (a), (b) and (c) show the variation of imaginary part (Z'') of complex impedance as a function of frequency for $Bi_{1-x}Gd_xFe_{0.9}Cr_{0.1}O_3$ compositions sintered at 825,

850 and 875 °C for 4 h respectively. The dependence of Z'' with frequency (Fig. 4.16) shows similar behavior as Z'. We observed that the value of imaginary part of complex impedance is lower in the Gd doped samples compositions than the undoped sample sintered at 825 and 875 °C but higher of the compositions sintered at 850 °C.

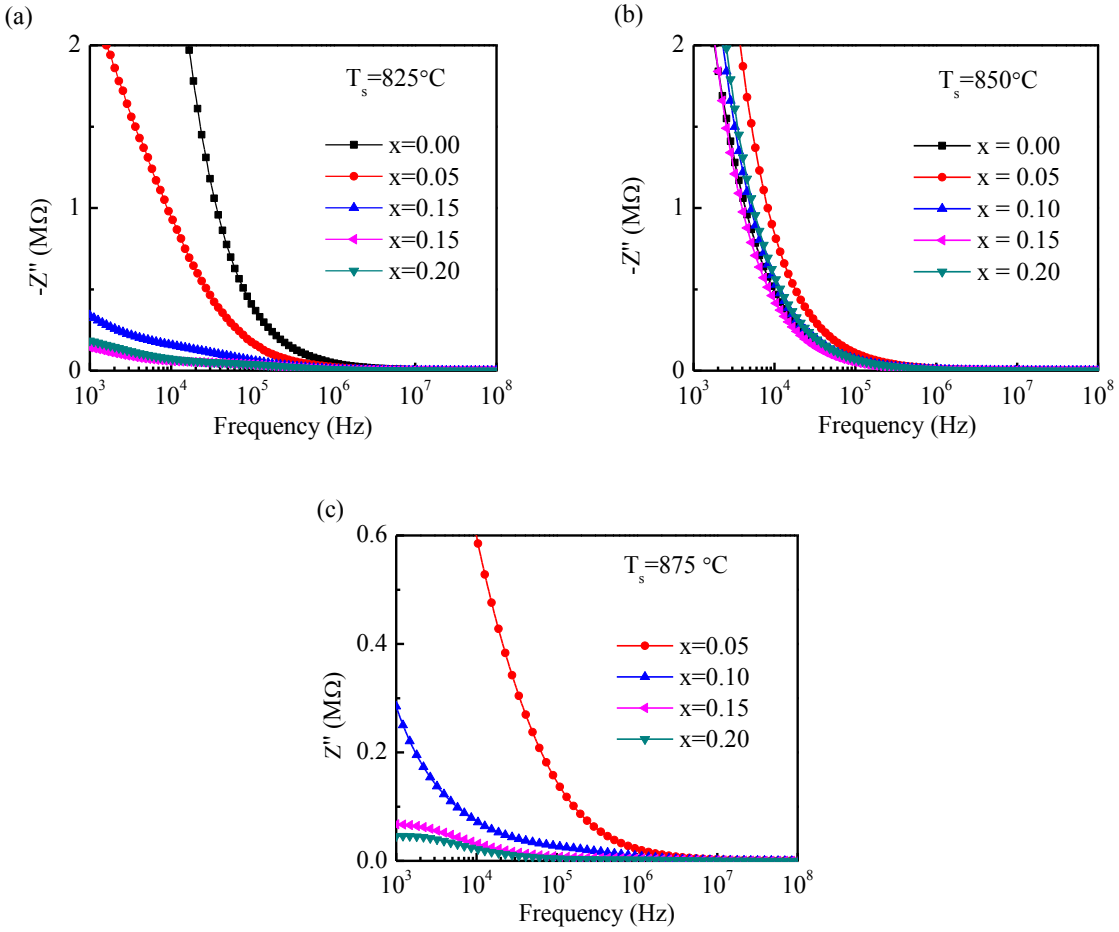

Fig. 4.16 Variation of the imaginary part (Z'') of complex impedance with frequency of $Bi_{1-x}Gd_xFe_{0.9}Cr_{0.1}O_3$ sintered at (a) 825, (b) 850 and (c) 875 °C for 4 h.

4.6.3 Cole-Cole plot analysis

Fig. 4.17 shows the Nyquist plot (Z'' vs Z') over a wide range of frequency (20 Hz – 120 MHz) of $Bi_{1-x}Gd_xFe_{0.9}Cr_{0.1}O_3$ compositions at room temperature to distinguish between the grain and grain boundary effects to the total resistance. In practice experimental data are only rarely found to yield a full semicircle with its center on the real axis of the complex plane. The perturbations which may still lead to at least part of a semicircular arc in the

complex plane are [17]: (i) The arc does not pass through the origin either because there are other arcs appearing at higher frequency and/or because resistance is greater than zero, (ii) The center of experimental arc is frequently displayed below the real axis because of the presence of distributed elements in the material-electrode system. The relaxation time τ is then not single valued but is distributed continuously or discretely around a mean, $\tau_m = \omega_m^{-1}$ and (iii) Arcs can be substantially distorted by other relaxations whose mean time constants are within two orders of magnitude or less of that for the arc under consideration. The semicircle in the high frequency side represents the bulk resistance and that in the low frequency side represents the grain boundary resistance. The third semicircle or a spike in the low frequency region is also observed in some materials which is attributed to the effect of electrodes [18]. This behavior can be explained by an equivalent circuit consisting of two sub-circuits connected in series as shown in Fig. 4.17(a). According to the equivalent circuit, the overall impedance can be expressed as:

$$Z = R_g - \frac{1}{j\omega C_g} + R_{gb} - \frac{1}{j\omega C_{gb}} \qquad (4.5)$$

Where R_g is the grain/bulk resistance, C_g is the bulk capacitance, R_{gb} is the grain boundary resistance and C_{gb} is the grain boundary capacitance. The low and high frequency semicircular arcs correspond to the $R_{gb}C_{gb}$ and R_gC_g responses, respectively. Depressed semicircular arcs are observed for all the samples both in the high and low frequency regions (shown in Fig. 4.17) which indicate that non Debye-type of relaxation exists in the present samples. The diameters of the high frequency region semicircular arcs are very small than those of low frequency region semicircular arcs indicating the dominant of grain boundary contribution to the total resistance. The variation of R_g and R_{gb} as a function of Gd content is shown in Fig. 2.18 The R_g and R_{gb} decreases with the Gd content in the compositions may be due to the conducting behavior of Gd.

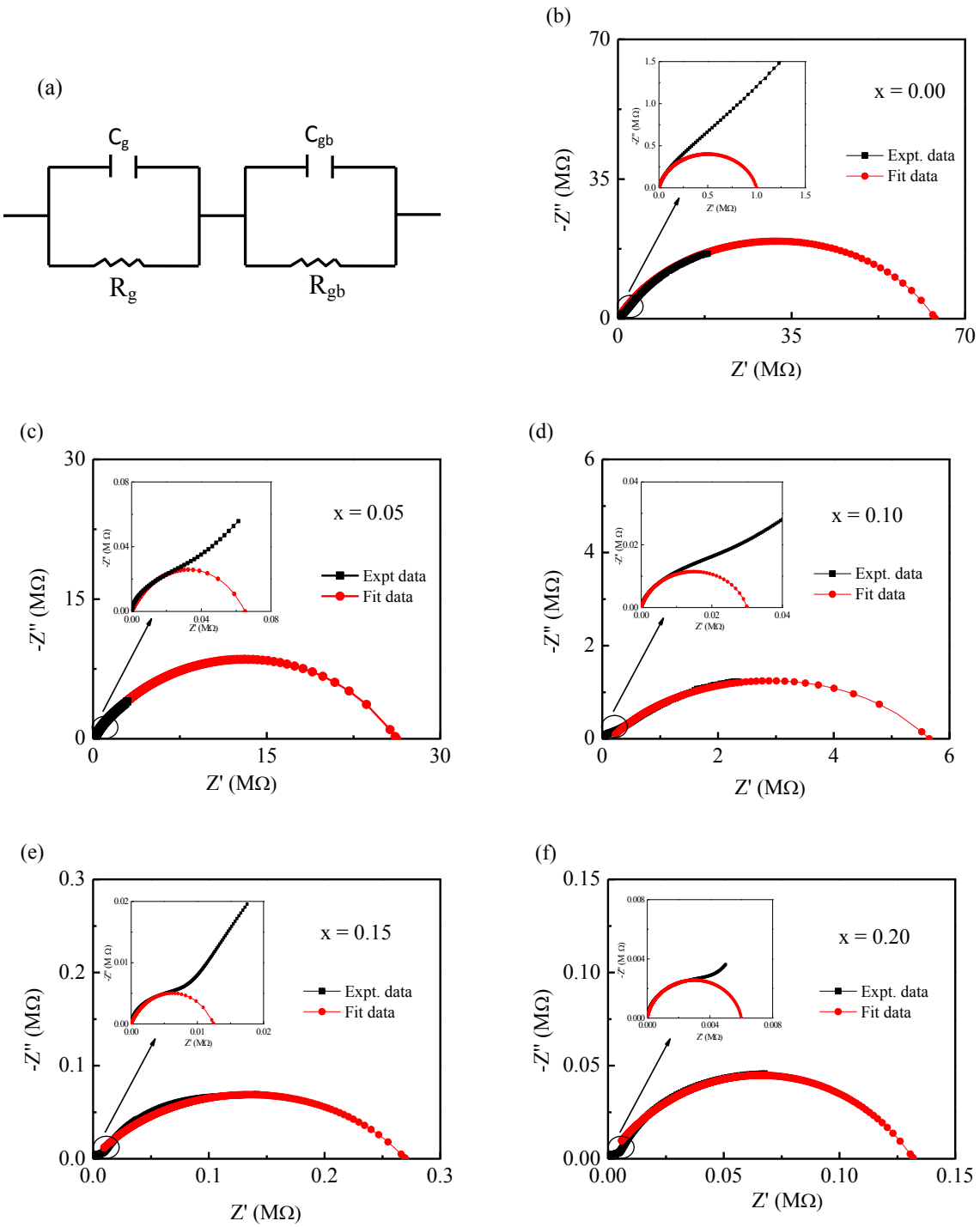

Fig. 4.17 (a) Electrical equivalent circuit; (b-f) Nyquist plot of various $Bi_{1-x}Gd_xFe_{0.9}Cr_{0.1}O_3$ compositions: (b) x = 0.00, (c) x = 0.05, (d) x = 0.10, (e) x = 0.15 and (f) x = 0.20.

Table 4.12: Grain and grain boundary resistance of various $Bi_{1-x}Gd_xFe_{0.9}Cr_{0.1}O_3$ compositions.

Compositions	x = 0.00	x = 0.05	x = 0.10	x = 0.15	x = 0.20
R_g (kΩ)	999.99	65.11	29.99	12.41	5.99
R_{gb} (kΩ)	64000	26228	5650	270	131

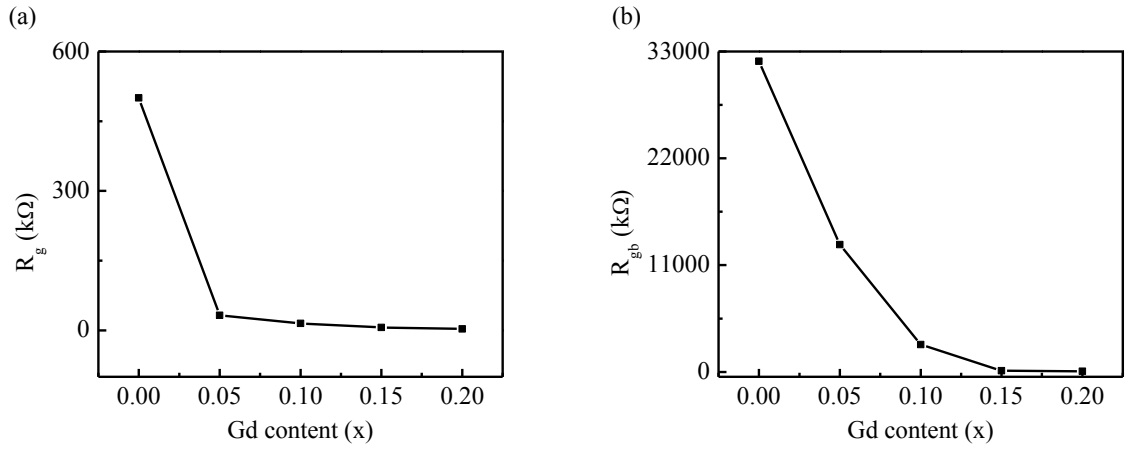

Fig. 4.18 Variation of (a) grain and (b) Grain boundary resistances with Gd content.

4.7 Complex modulus analysis

The electric modulus has been extensively used by many researchers to analyze and interpret electrical relaxation data in a wide variety of materials. This formalism provides wider insights on charge transport processes such as conductivity relaxation mechanism and ion dynamics as a function of frequency and temperature. In the modulus formalism [19], an electric modulus M* is defined as the inverse of the complex dielectric permittivity ε*:

$$M^* = \frac{1}{\varepsilon^*} \qquad (4.6)$$

4.7.1 Real part of complex modulus

Fig. 4.19(a), (b) and (c) show the variation of real part of modulus (M′) with frequency. The value of M′ at lower frequency is very small and it increases with increase in frequency. This continuous dispersion on increasing frequency may be due to the conduction phenomenon due to short range mobility of charge carriers. It is related to the lack of restoring force leading the mobility of the charge carriers under the action of an induced electric field [20]. Low value of M′ in the lower frequency side supports the conduction

phenomena due to long range mobility of charge carriers as well as that the electrode polarization makes a negligible contribution in the material [21].

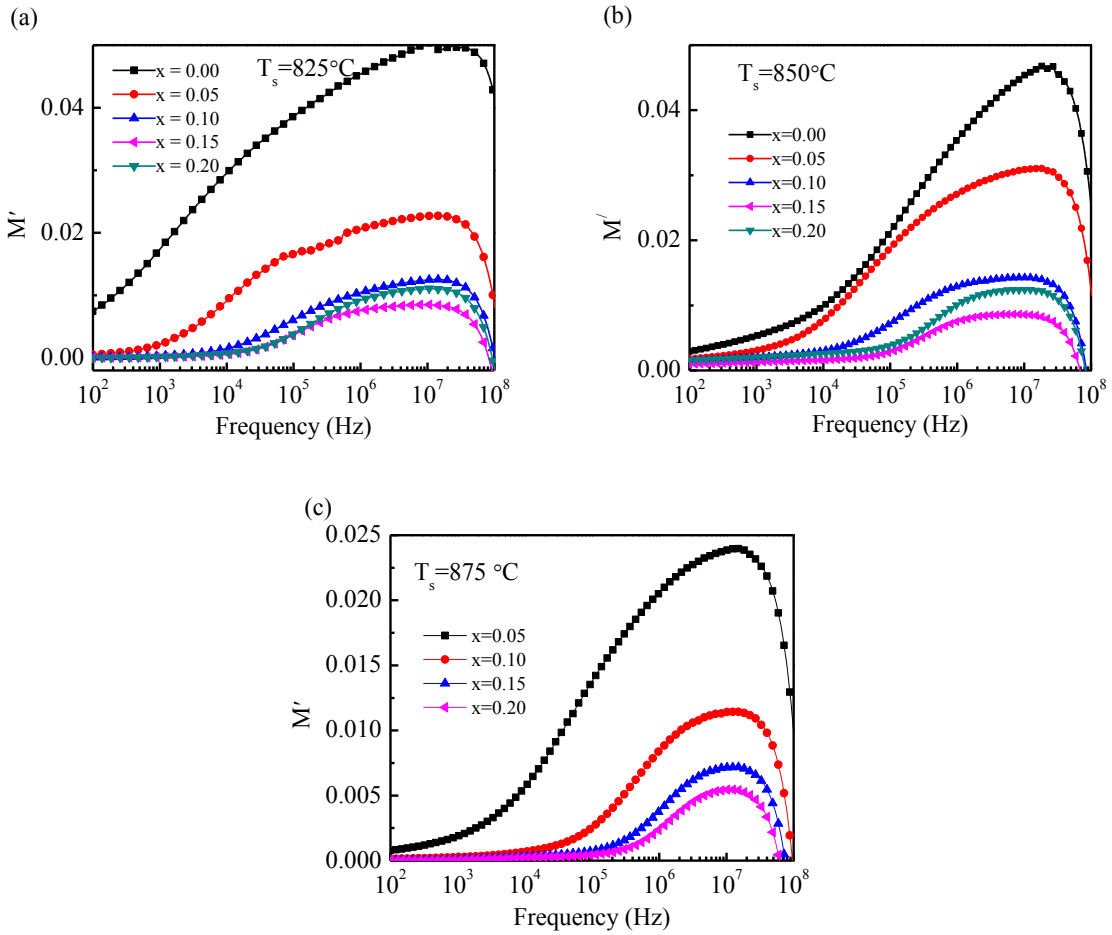

Fig. 4.19 Variation of Real part of complex dielectric modulus of various $Bi_{1-x}Gd_xFe_{0.9}Cr_{0.1}O_3$ with frequency sintered at various temperatures.

4.7.2 Imaginary part of complex modulus

The frequency dependence of imaginary part of dielectric modulus (M″) at various sintering temperatures is shown in Fig.4.20. All the samples show a relaxation peak at higher frequency which is associated with grain effects. The frequency region below the peak represents the range in which the charge carriers are mobile over long distances, whereas the frequency region above the peak determines the range in which the charge carriers are confined to their potential wells, and thus could make localized motions inside the well [22].

The high frequency peak in the M″ curves is found to be asymmetric, implying a non-exponential behavior of the bulk conductivity relaxation. This type of behavior suggests the possibility that the ion migration takes place via hopping accompanied by a consequential time-dependent mobility of other charge carriers of the same type in their vicinity [23]. The characteristic frequency, at which M″ is maximum, corresponds to relaxation frequency.

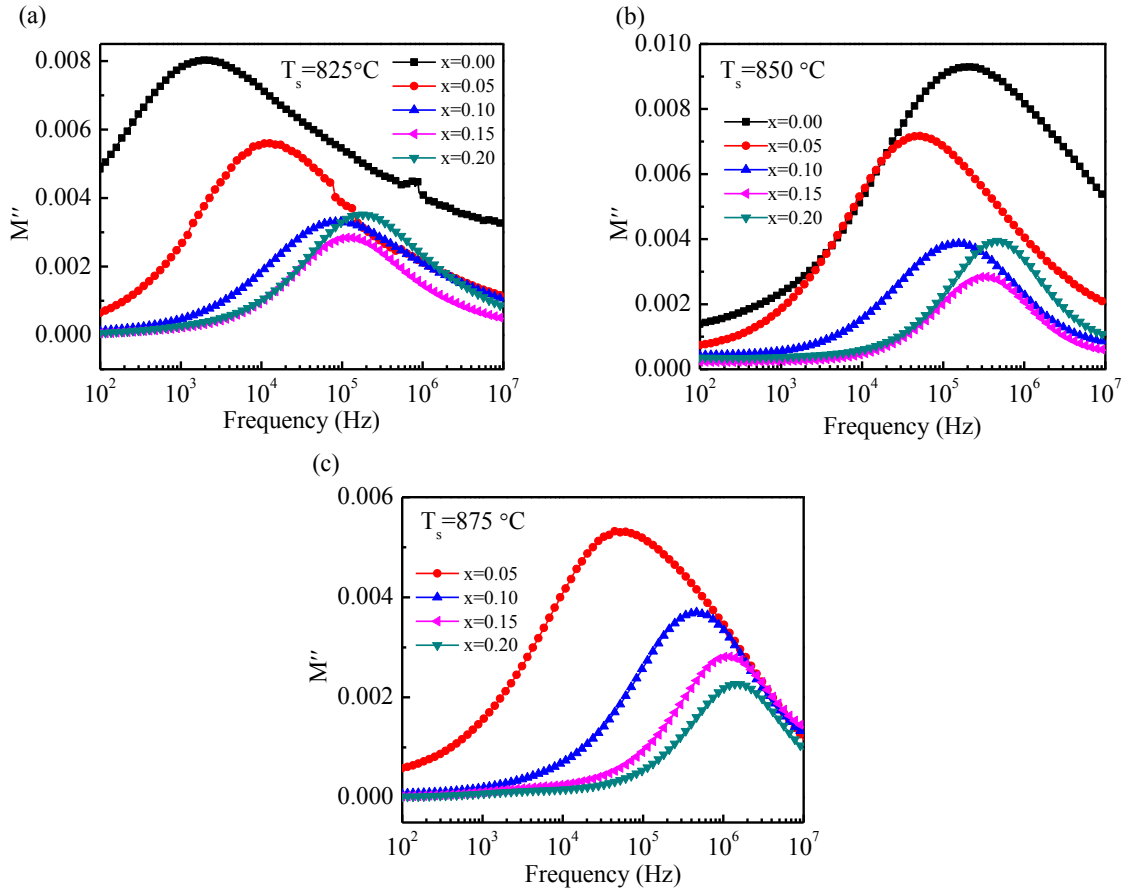

Fig. 4.20 Variation of imaginary part of complex dielectric modulus of various $Bi_{1-x}Gd_xFe_{0.9}Cr_{0.1}O_3$ with frequency sintered at various temperatures.

4.8 AC conductivity

In the research of materials science conductivity is an important issue. Conductivity plays a crucial role in BFO [24]. BFO is one of the most extensively studied multiferoic compound which exhibits electric as well magnetic properties at room temperature. Fig.4.21 shows the variation of AC conductivity ($_{AC}$) with frequency of various $Bi_{1-x}Gd_xFe_{0.9}Cr_{0.1}O_3$ sintered at (a) 825, (b) 850 and (c) 875 °C. At lower frequency, which corresponds to DC

conductivity ($_{DC}$), the conductivity is almost independent of frequency. On the other hand, at higher frequency, which is known as hopping region; the AC conductivity increases faster than that of DC conductivity. At high frequency the conductive grains become more active and hence increases hopping of charge carriers and contribute to rise in conductivity. The frequency dependent AC conductivity of $Bi_{1-x}Gd_xFe_{0.9}Cr_{0.1}O_3$ relaxors obey the Jonscher's power law [14].

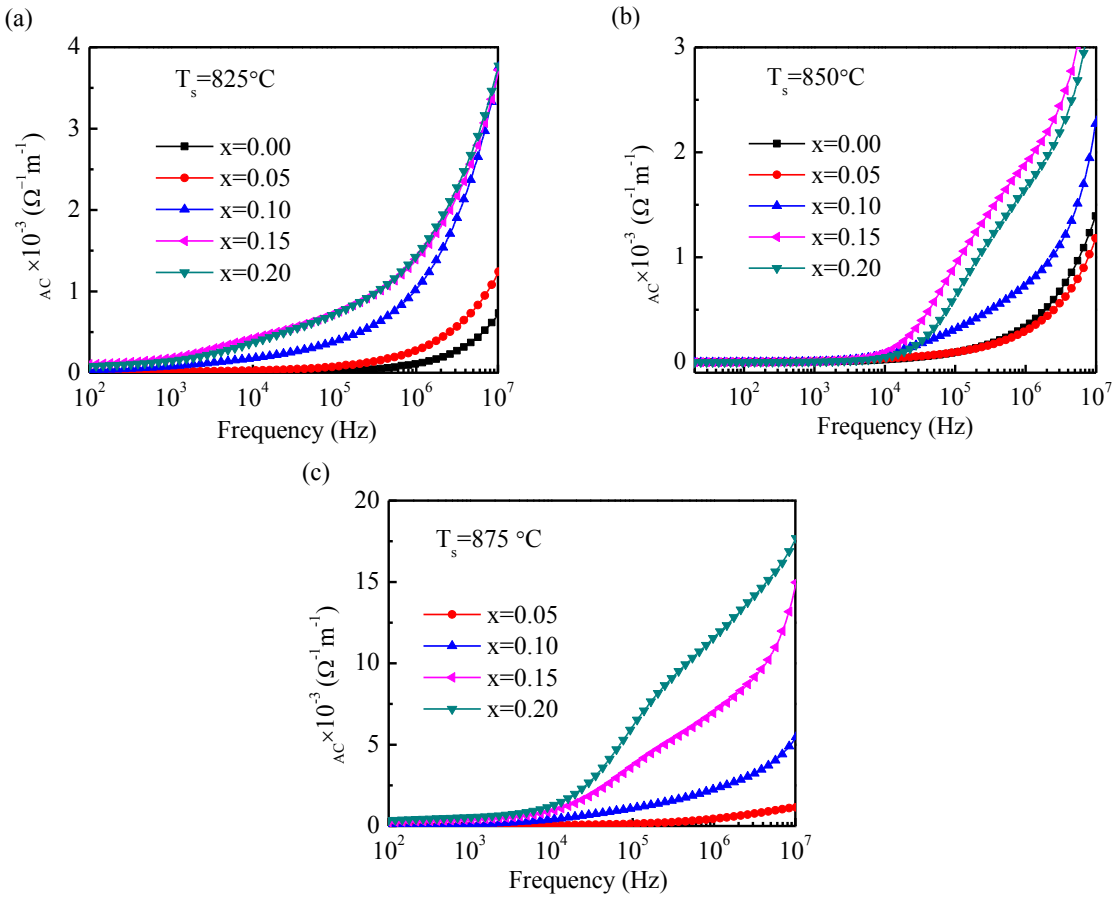

Fig. 4.21 Variation of AC conductivity ($_{AC}$) with frequency at various sintering temperatures.

The conductivity can also be explained on the basis of polaron hopping mechanism. In small polaron hopping $_{AC}$ increases with the increase in frequency while in large polaron hopping $_{AC}$ decreases with the increase in frequency [25]. In the present study, all compositions exhibit an increase in conductivity with frequency as shown in Fig.4.21 which indicates that small polaron hopping is present in the conduction mechanism of the studied

compositions. From Fig. 4.21, it is seen that the value of AC conductivity ($_{AC}$) increases with the increase in Gd content i.e, Gd helps to enhance the number of charge carriers in BFO which contribute to increase $_{AC}$.

Fig. 4.22 shows the log($_{AC}$) vs log(ω^2) plot of various $Bi_{1-x}Gd_xFe_{0.9}Cr_{0.1}O_3$ (x = 0.00, 0.05, 0.10, 0.15 and 0.20) ceramics. Samples, sintered at 825 and 875 °C show one region and samples, sintered at 850 °C shows three distinct regions in the conductivity spectra. In conductivity spectra the first region is low frequency dispersive region, second region is intermediate frequency plateau region and third region is high frequency dispersive region. The variation of $_{AC}$ with frequency can be explained on the basis of modified Jonscher's law known as double power law [26]:

$$_{AC}(\omega) = \ (0) + A_1\omega^{n_1} + A_2\omega^{n_2} \qquad (4.7)$$

where $_{AC}$ is the total conductivity, (0) is the frequency independent conductivity i.e, dc conductivity. The coefficient A_1 and A_2 and exponents n_1, n_2 are temperature and materials' intrinsic properties dependent. The second term $A_1\omega^{n_1}$ is assigned to region I; the exponent n_1 ($0<n_1<1$) characterizes the low frequency dispersion and corresponds to the long range hopping associated with grain boundaries [27]. The last term $A_2\omega^{n_2}$ is assigned to region III (in Fig. 4.22 (b)) and region II (in Fig. 4.22(a and c)); the exponent n_2 ($0<n_2<2$) corresponds to the short range hopping within the grain [27]. Thus the conduction process in the low frequency dispersive region is mainly due to long range hopping and that in the high frequency dispersive region is due to reorientational i.e, short range hopping motion. Hopping mechanism is favored in ionic lattices in which the same kind of cation is found in two different oxidation states. Thus, in the conduction process, the hopping of 3d electrons between Fe^{2+} and Fe^{3+} might play an important role. Hopping mechanism is very useful for analyzing the conduction process in materials, for determining the activation energy and the nature of electron-phonon coupling [28].

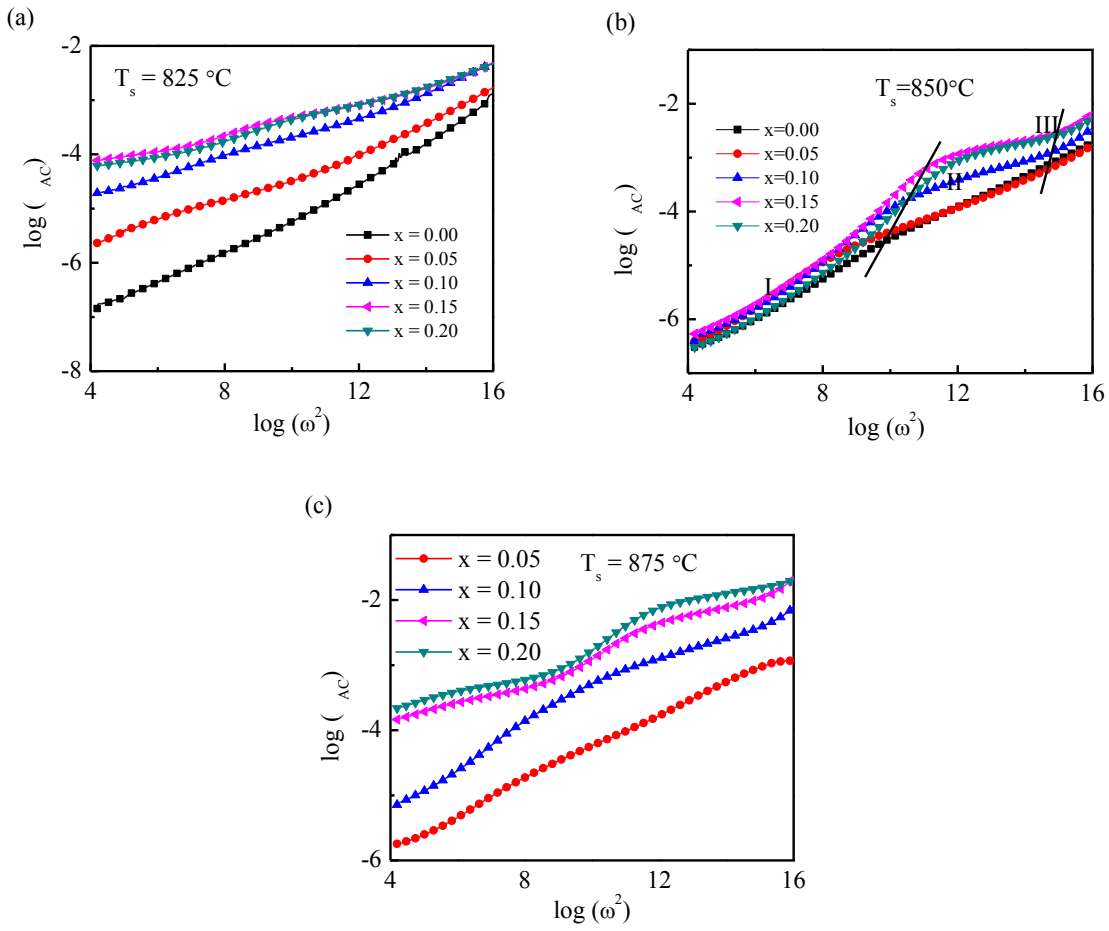

Fig. 4.22 log($_{AC}$) vs log(ω^2) plot of various $Bi_{1-x}Gd_xFe_{0.9}Cr_{0.1}O_3$ ceramics.

4.9 Complex initial permeability

4.9.1 Real part of complex permeability

Fig. 4.23 shows the variation of real part of complex initial permeability (μ_i') with frequency for various $Bi_{1-x}Gd_xFe_{0.9}Cr_{0.1}O_3$ compositions within the frequency range of 100 KHz-100MHz measured at room temperature. From figure, it is seen that the value of real part of complex permeability for all compositions remains approximately constant upto a certain frequency and then decreases with increasing frequency. It is also observed that the value of real part of complex permeability of $Bi_{1-x}Gd_xFe_{0.9}Cr_{0.1}O_3$ is highest which is sintered at 875 °C. The maximum value of real part of permeability is found 30.52 at 100 KHz. Initial permeability in a material originates because of the spin rotation and domain wall motion.

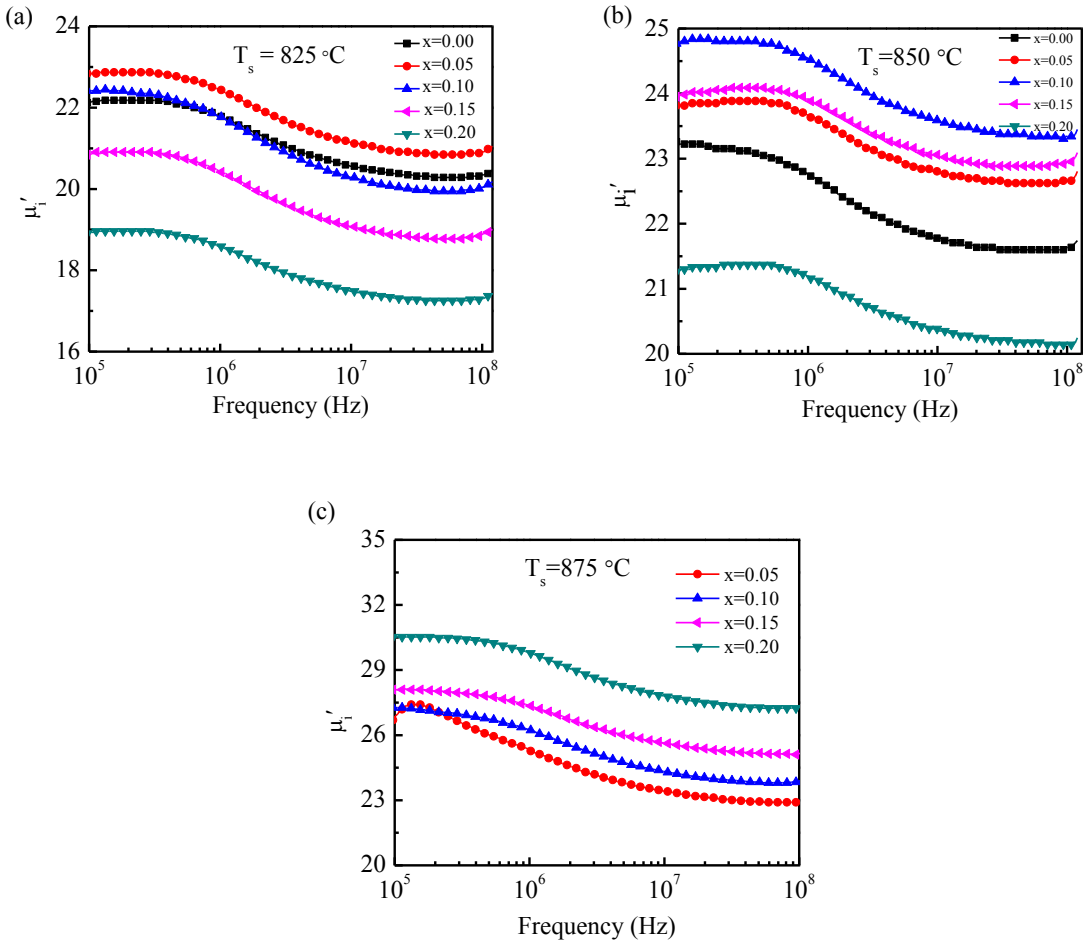

Fig. 4.23 Variation of real part of complex initial permeability with frequency of various $Bi_{1-x}Gd_xFe_{0.9}Cr_{0.1}O_3$ sintered at (a) 825 (b) 850 and (c) 875 °C.

The μ_i' decreases with frequency which is due to the fact that at higher frequencies pinning points are found to be originated at the surface of the samples from the impurities of grains and intragranulars pores. This phenomenon in turn obstructs the motion of spin and domain walls and the contribution of their motion towards the increment of permeability decreases [29]. Actually it is difficult to explain compositional dependence of μ_i' for the case of polycrystalline materials because μ_i' depends on many factors such as stoichiometry, composition, average grain size, spin rotation, porosity, impurity, coercivity etc.

In BFO, oxygen vacancies create due to the reduction of Fe^{3+} and volatilization of Bi^{3+} during sintering process. The oxygen vacancies may affect domain wall motion by the

formation of mechanical barrier against the domain wall [30]. All the compositions (except $Bi_{0.85}Gd_{0.15}Fe_{0.9}Cr_{0.1}O_3$) with Gd doped, sintered at 850 °C and all the compositions sintered at 875 °C show large value of permeability than the undoped $BiFe_{0.9}Cr_{0.1}O_3$. This may be due to the decreasing of oxygen vacancy. Permeability also depends on homogeneity of grains of a material. The material with homogeneous grains shows higher values of permeability than material with inhomogeneous grains.

4.9.2 Imaginary part of complex permeability

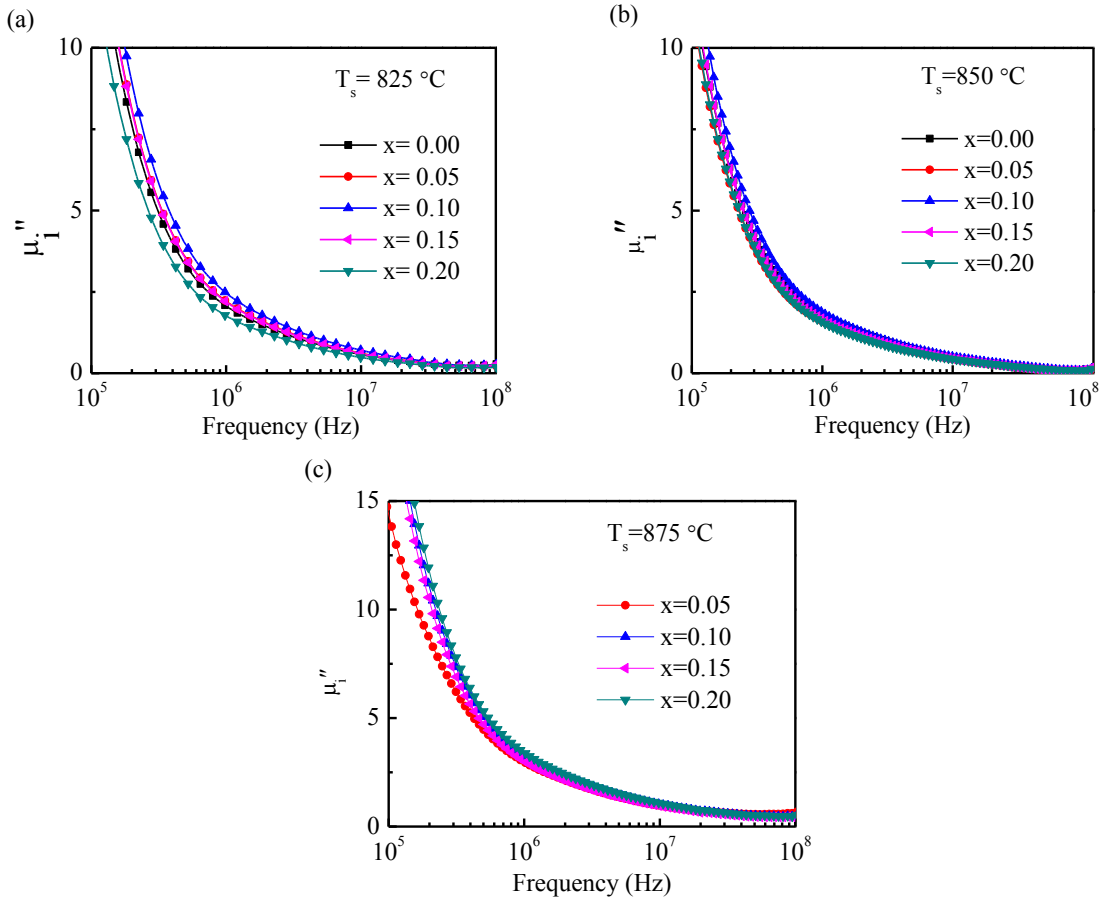

Fig. 4.24 Variation of imaginary part of complex initial permeability with frequency of various $Bi_{1-x}Gd_xFe_{0.9}Cr_{0.1}O_3$ sintered at (a) 825 (b) 850 and (c) 875 °C.

The frequency dependent of the imaginary part of complex permeability (μ′′) of the compositions measured at room temperature over the frequency range of 100 kHz-100 MHz

sintered at 825, 850 and 875 °C is shown in Fig. 4.24. In the low frequency region, the imaginary part of μ″ shows dispersion behaviors which are attributed due to domain wall displacements. Here imaginary part of μ″ decreases with increasing frequency. At higher frequency μ″ is almost independent of frequency. The μ″ is frequency independent at higher frequency region shows that there is only spin rotation is effective.

4.10 Magnetic loss

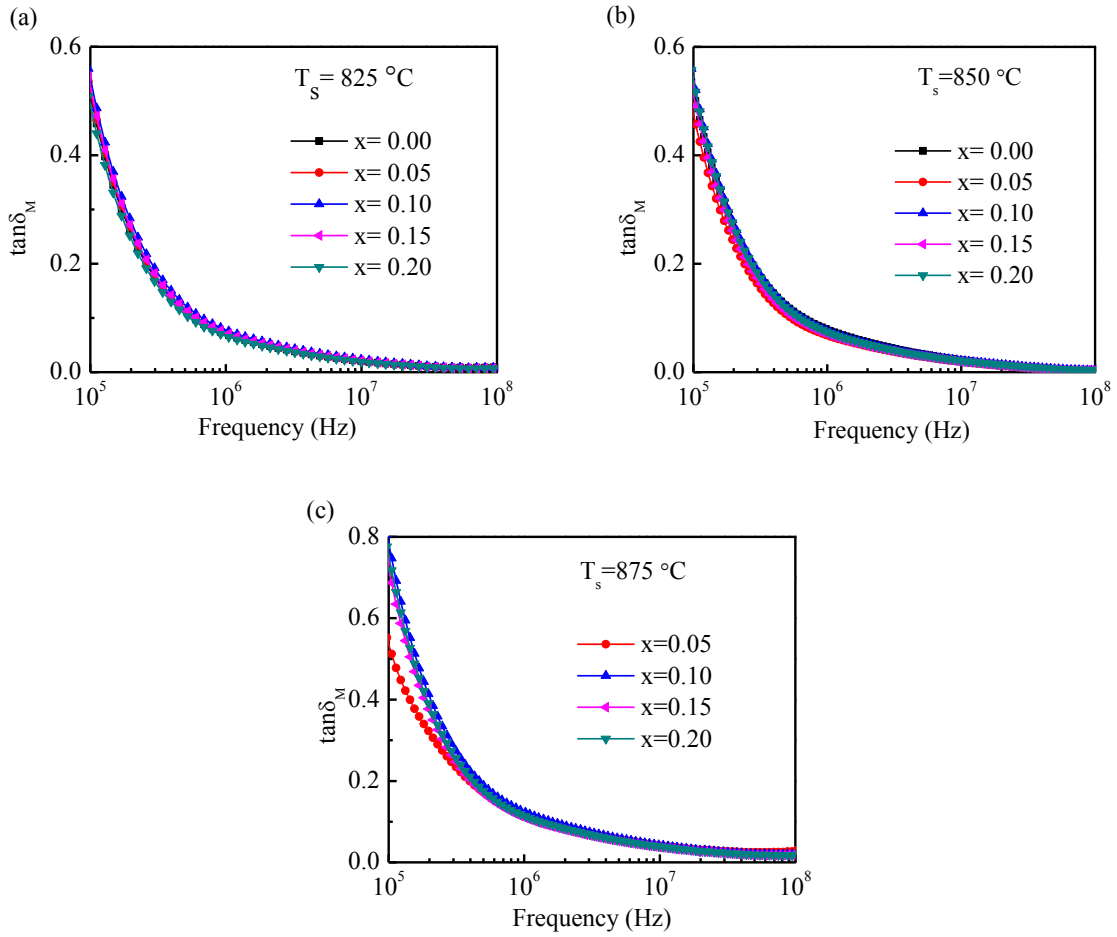

Fig. 4.25 Variation of magnetic loss (tan $_M$) with frequency of various $Bi_{1-x}Gd_xFe_{0.9}Cr_{0.1}O_3$ measured at room temperature.

Fig.4.25 shows the variation of magnetic loss of various $Bi_{1-x}Gd_xFe_{0.9}Cr_{0.1}O_3$ compositions with frequency sintered at (a) 825 (b) 850 and (c) 875 °C. It is seen that the value of tan $_M$ decreases exponentially with increasing frequency. The value of tan $_M$ remains almost

constant at higher frequency. The tan $_M$ arises due to the lag of domain wall motion with respect to applied field and creates imperfections in the lattice. The value of tan $_M$ decreases with the increase in Gd content due to the reduction of imperfections.

4.11 Relative quality factor

Fig.4.26 shows the variation of relative quality factor of various $Bi_{1-x}Gd_xFe_{0.9}Cr_{0.1}O_3$ samples sintered at (a) 825 (b) 850 and (c) 875 °C. The peak value of RQF is observed at about 80 MHZ and then decrease. It is also seen that the value of RQF increases with the increase in Gd content. Also it is noticed that the peak shifts toward the higher frequency. So the Gd doped $Bi_{1-x}Gd_xFe_{0.9}Cr_{0.1}O_3$ materials can be used in practical applications. At higher frequency RQF decreases due to ferromagnetic loss. This loss is mainly due to phase lag of domain wall motion with respect to the applied AC magnetic field.

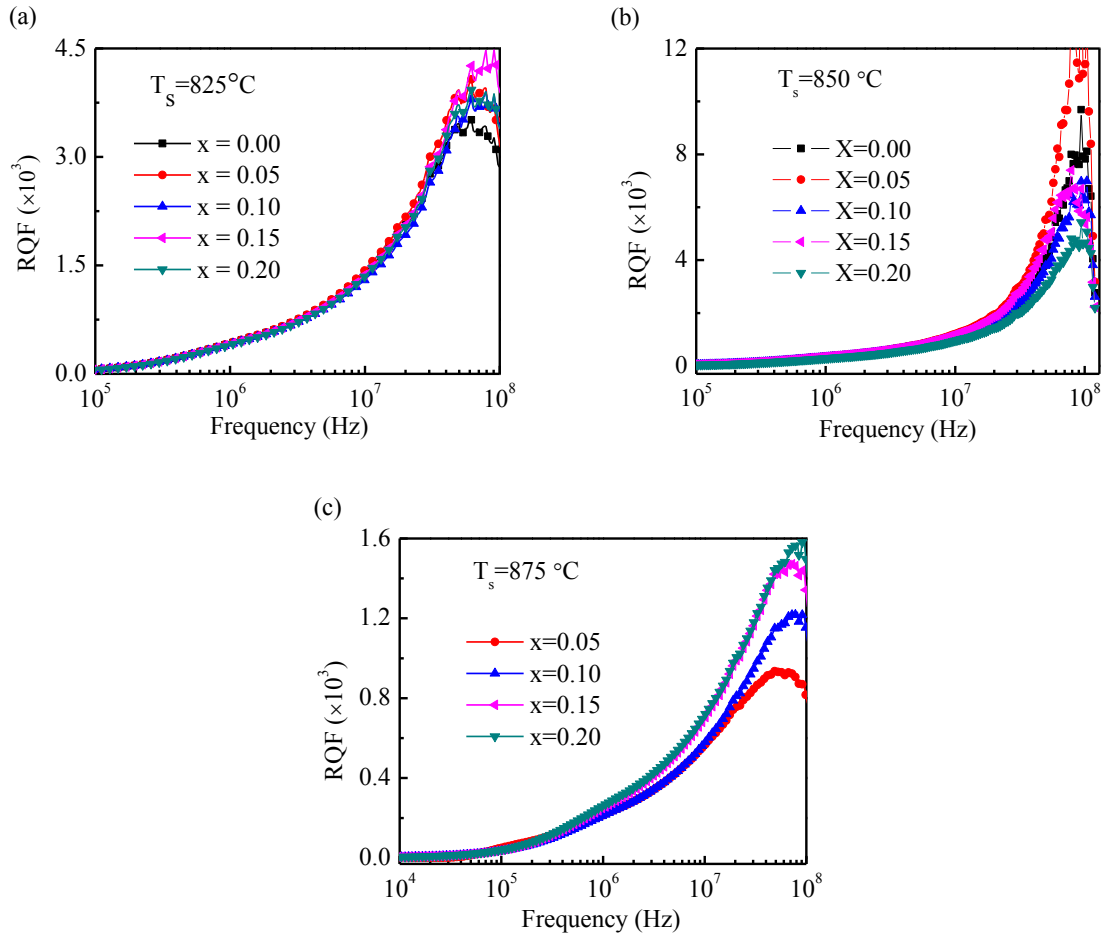

Fig. 4.26 Relative quality factor of various $Bi_{1-x}Gd_xFe_{0.9}Cr_{0.1}O_3$ measured at room temperature.

4.12 M-H hysteresis loops

The magnetic field dependent magnetization of various $Bi_{1-x}Gd_xFe_{0.9}Cr_{0.1}O_3$ samples sintered at 850 °C measured at room temperature is shown in Fig. 4.27. From figure, it is clear that all samples show unsaturated magnetization. Enlarged view of $Bi_{1-x}Gd_xFe_{0.9}Cr_{0.1}O_3$ are shown in Fig. 4.28((a) x = 0.00, (b) x = 0.05, (c) x = 0.10 (d) x = 0.15 and (e) x = 0.20). In BiFeO3, Fe magnetic moments are coupled ferromagnetically within the pseudocubic (111) plane and antiferromagnetically between adjacent planes. There is canting of antiferromagnetic sublattices resulting in a macroscopic magnetization. Superimposed on antiferromagnetic ordering, there is a spiral spin structure which leads to cancellation of macroscopic magnetization. Magnetization is induced in the sample whenever this spiral structure is suppressed [31]. Enhanced magnetization is found in $BiFe_{0.9}Cr_{0.1}O_3$ due to the breaking of the cycloidal spin structure [32].

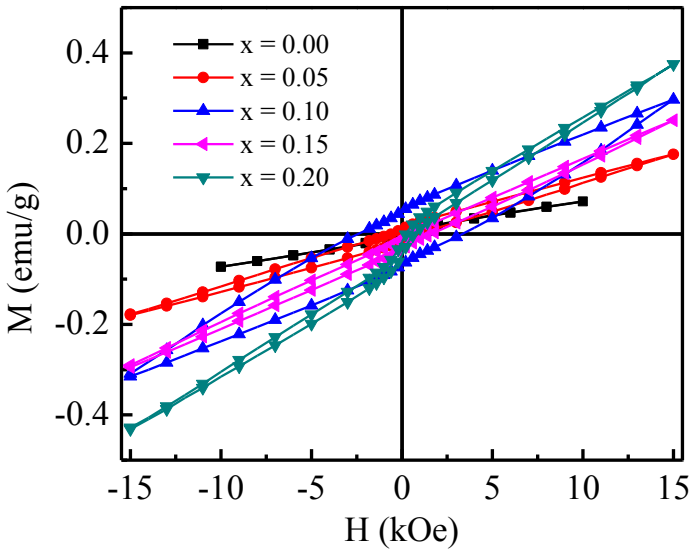

Fig. 4.27 M – H hysteresis loops of various $Bi_{1-x}Gd_xFe_{0.9}Cr_{0.1}O_3$ measured at room temperature.

All the samples show unsaturated magnetization loops which confirm the basic antiferromagnetic nature of the compound. The magnetization increases with the increase in content of Gd. The magnetization is almost four times greater when the concentration of Gd

is increased from 0.00 to 0.20. This could be due to the structural distortion in the perovskite with change in Fe–O–Fe bond angle. This structural distortion could lead to suppression of the spin spiral and hence enhance the magnetization in the system.

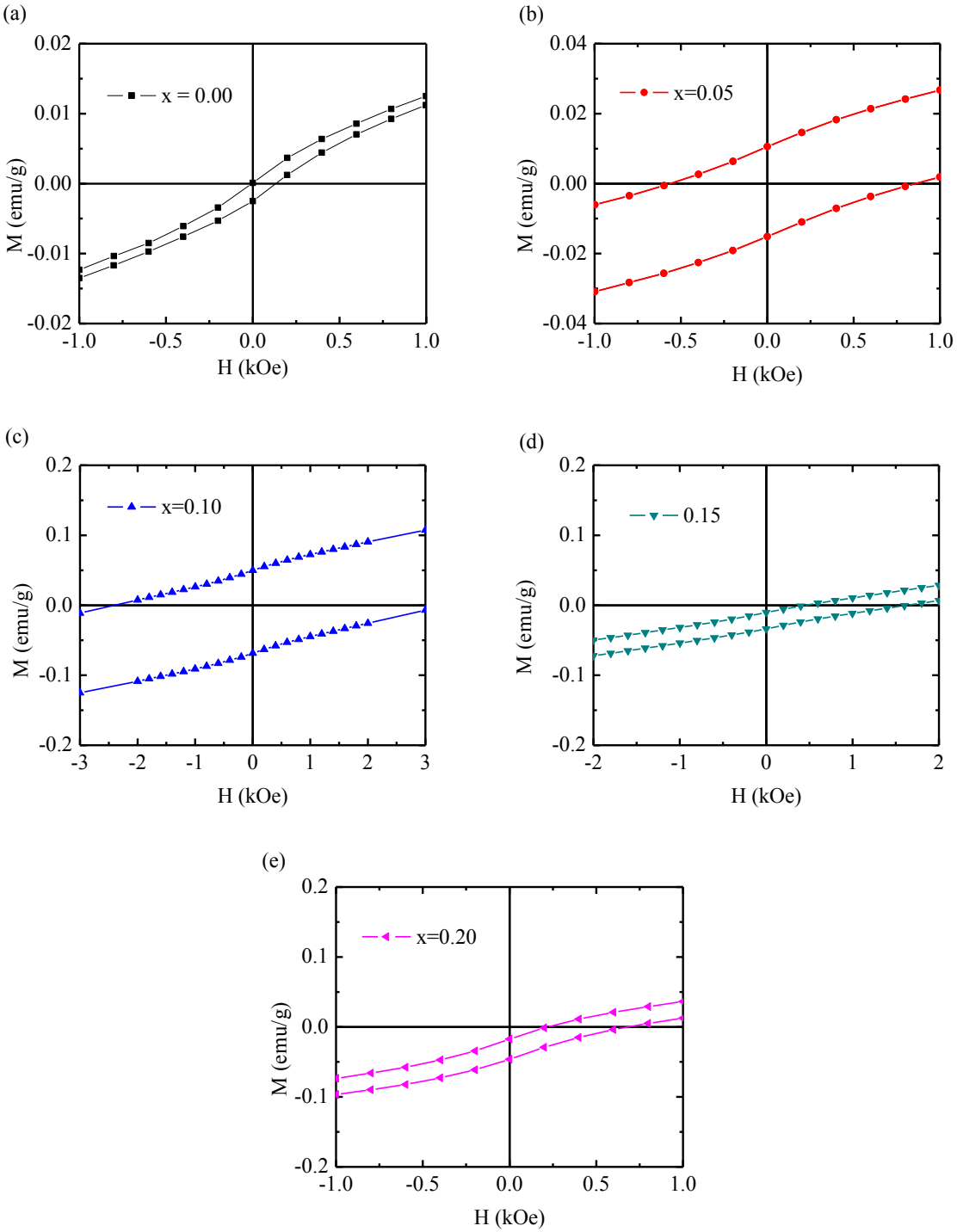

Fig. 4.28 Enlarge view of the low field M – H hysteresis loops of $Bi_{1-x}Gd_xFe_{0.9}Cr_{0.1}O_3$ (a) x = 0.05, (b) x = 0.10, (c) x = 0.15 and (d) x = 0.20.

From the M – H hysteresis loops, the remanent magnetization (M_r) was calculated using the equation:

$$M_r = \frac{M_{r_1} - M_{r_2}}{2} \quad (4.8)$$

Where, M_{r_1} and M_{r_1} are the magnetization with upper and lower points of intersection with H = 0 respectively [33].

The coerceive field (H_c) was calculated using the equation:

$$H_c = \frac{H_{c_1} - H_{c_2}}{2} \quad (4.9)$$

Where, H_{c_1} and H_{c_2} are the left and right coerceive field [34]. Calculated values of $M_r$and H_c are shown in Table 4.12 and M_r and H_c are plotted in Fig.4.29 (a) and (b) respectively.

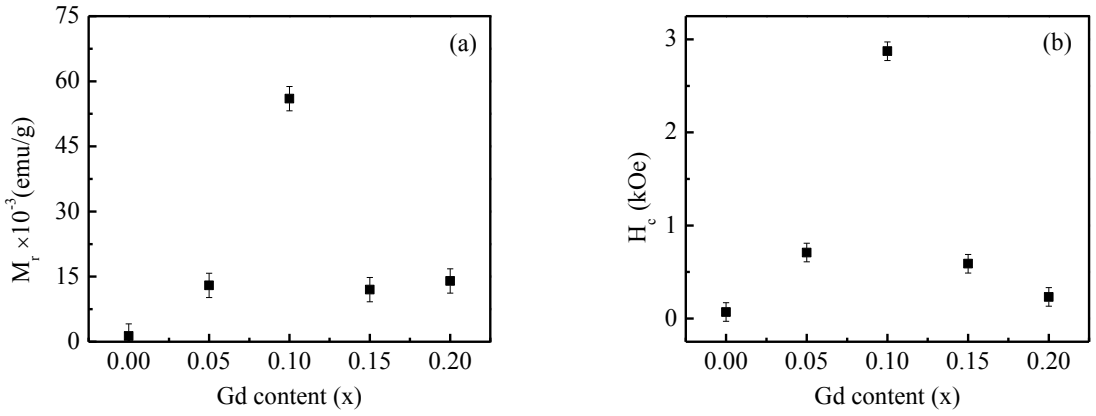

Fig. 4.29 Variation of (a) remanent magnetization and (b) coerceive field at RT in $Bi_{1-x}Gd_xFe_{0.9}Cr_{0.1}O_3$ ceramics with Gd content.

Table 4.13: Remanent magnetization and coercive field of various $Bi_{1-x}Gd_xFe_{0.9}Cr_{0.1}O_3$ samples measured at room temperature.

Gd content (x)	M_r (emu/g)	H_c (Oe)
0.00	0.0013	69
0.05	0.013	709
0.10	0.056	2873
0.15	0.012	589
0.20	0.014	232

4.13 Magnetoelectric coefficient

The variation of magnetoelectric coefficient ($_{ME}$) with applied DC magnetic field measured at room temperature is shown in Fig. 4.30. Generally, in ME measurement, the strain induced in sample by the application of magnetic field generates an electric field on the ferroelectric domain resulting in an increase in polarization [35]. ME is calculated from the observed voltages and plotted against applied DC bias magnetic field, $_{ME}$ vs H_{DC} (Fig. 4.30). As DC magnetic field increases, all the samples show similar characteristics. It could be seen that $_{ME}$ slightly increased with the increase in magnetic field.

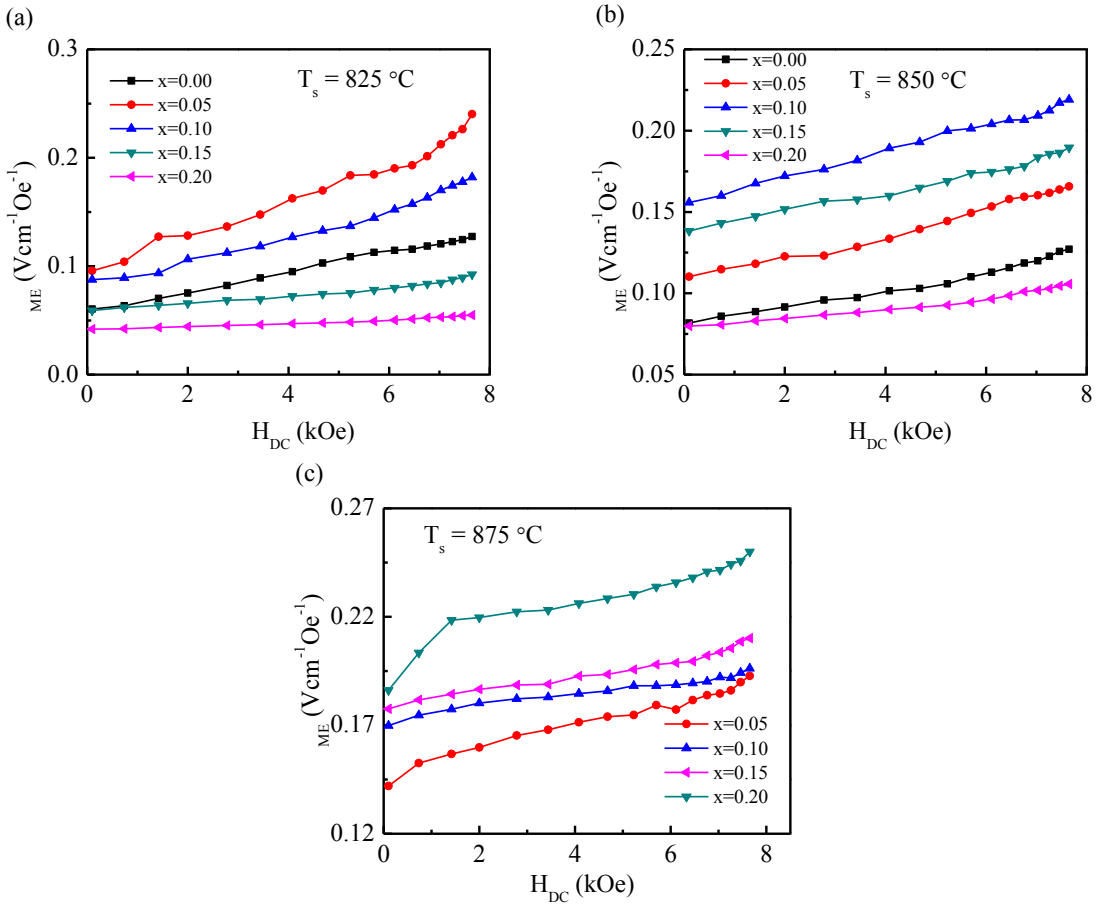

Fig. 4.30 Variation of $_{ME}$ of $Bi_{1-x}Gd_xFe_{0.9}Cr_{0.1}O_3$ with applied DC magnetic field.

The pure BFO exibits a poor $_{ME}$ (0.32 mV/cmOe) [36] and the value of $_{ME}$measured by S.V. Vijayasundaram et al. for the pure BFO sample is about 1.38 mV/cm

Oe [37]. Also S.V. Vijayasundaram et al. found considerably no change of $_{ME}$with 5 % and 10 % Gd content [37]. But with Cr, and both Gd as well as Cr doped BFO shows enhanced $_{ME}$. The ME effect in multiferroic materials arises due to the interaction of the magnetic and ferroelectric domains [38]. Applied magnetic field induces large strain in magnetic domains of the samples due to the presence of Gd^{3+}, because Gd^{3+} create more distortion as it is ferromagnetic and the ionic radius of Gd^{3+} and $Bi^{3+}$are dissimilar. This causes strong ME coupling in the material. It is observed that the value of $_{ME}$ increases with the increase in sintering temperature.

References

[1] Chang, F., Zhang, N., Yang, F., Wang, S and Song, G, "Effect of Cr substitution on the structure and electrical properties of $BiFeO_3$ ceramics", *J. Phys. D: Appl. Phys.*, Vol. 40, pp. 7799–7803, 2007.

[2] Uniyal, P. and Yadav K. L., "Study of dielectric, magnetic and ferroelectric properties in $Bi_{1-x}Gd_xFeO_3$", *Mater. Lett.*, Vol. 62, pp. 2858-2861, 2008.

[3] Miao, J. H., Chung, H. Y., Yang, C. W. and Fang, T. T., "Effect of La Doping on the Phase Conversion, Microstructure Change,and Electrical Properties of $Bi_2Fe_4O_9$ Ceramics", *J. Am. Ceram. Soc*., Vol. 92, pp. 2762-2764, 2009.

[4] Tsai, C. J., Yang, C. Y., Liao, Y. C and Chueh, Y. L., "Hydrothermally grown bismuth ferrites: controllable phases and morphologies in a mixed KOH/NaOH mineralizer", *J. Mater.* Chem., Vol. 22, pp. 17432, 2012.

[5] Khomchenko, V. A., Kiselev, D. A., Bdikin, I. K., . Shvartsman, V. V., Borisov, P., Kleemann, W., Vieira, J. M. and Kholkin, A. L., "Crystal structure and multiferroic properties of Gd-substituted $BiFeO_3$", *Appl. Phys. Lett.*, Vol. 93, pp. 262905, 2008.

[6] Weiwei, H., Chen, Y., Yuan, H., Li, G., Qiao, Y., Qin, Y. and Feng, S., "Structure, Magnetic, and Ferroelectric Properties of $Bi_{1-x}Gd_xFeO_3$ Nanoparticles", *J. Phys. Chem. C*, Vol. 115, pp. 8869–8875, 2011.

[7] Sattar, A. A., El-Sayed, H. M., El-Shookrofy, K. M. and El-Tabey, M. M., "Improvement of the magnetic properties of Mn-Ni-Zn ferrite by the non-magnetic Al-ion substitution", *J. Appl. Sci.*, Vol. 5, pp. 162-168, 2005.

[8] Lotey, G. S. and Verma, N. K., "Structural, magnetic, and electrical properties of Gd-doped BiFeO3 nanoparticles with reduced particle size", *J. Nanopart. Res.*, Vol. 14, pp. 742, 2012.

[9] Case, E. D., Smyth, J. R. and Monthei, V., "Grain size determinations", *J. Am. Ceram. Soc.*, Vol. 64, pp. C24-C25, 1981.

[10] Fiebig, M., Lottermoser, T.h., Fröhlich, D., Goltsev, A.V. and Pisarev, R.V., "Observation of coupled magnetic and electric domains", *Nature*, Vol. 419, pp. 818–820, 2002.

[11] Maxwell, J. C., *Electric and Magnetism*, Oxford University Press, New York, p. 828, 1973.

[12] Koops, C. G., "On the Dispersion of Resistivity and Dielectric Constant of Some Semiconductors at Audio frequencies", *Phys. Rev.*, Vol. 83, pp. 121–124, 1951.

[13] Rezlescu, N. and Rezlescu, E., "Dielectric properties of copper containing ferrites", *Phys. Stat. Sol. A*, Vol. 23, pp. 575–582, 1974.

[14] Jonscher, A. K., "The universal dielectric response", *Nature*, Vol. 267, pp. 673-679, 1977.

[15] Fouskova, A. and Cross, L. E., "Dielectric Properties of Bismuth Titanate", *J. Appl. Phys.*, Vol. 41, pp. 2834, 1970.

[16] Bauerle, E., "Study of solid electrolyte polarization by a complex admittance method", *J. Phys. Chem.*, Vol. 30, pp. 2657–2670, 1969.

[17] Kumar, M. M., Srinivas, A. and Suryanarayana, S. V., "Structure property relations in $BiFeO_3/BaTiO_3$ solid solutions", *J. Appl. Phys.*, Vol. 87, pp. 855-862, 2000.

[18] Pattanayak, S., Choudhary, R. N. P., Das, P. R. and Shannigrahi, S. R., "Effect of Dy-substitution on structural, electrical and magnetic propertiesof multiferroic $BiFeO_3$ ceramics", *Ceram. Int.*, Vol. 40, pp. 7983-7991, 2014.

[19] Macedo, P.B., Moynihan, C.T. and Laberge, N.L., "The Debye-Falkenhagen theory of electrical relaxation in glass", *Phys. Chem. Glasses*, Vol. 14, pp. 122, 1973.

[20] Macedo, P.B., Moynihan, C. T. and Bose, R., "The conductivity of the super ionic glass samples increases after irradiation and conductors", *Phys. Chem. Glasses*, Vol. 13, pp. 171-179, 1972.

[21] Chowdari, B. V. R. and Gopalkrishnnan, R, "AC conductivity analysis of glassy silver iodomolybdate system", *Solid State Ionics*, Vol. 23, pp. 225–233, 1987.

[22] Punia, R., Kundu, R.S., Dult, M., Murugavel, S. and Kishore, N., "Temperature and frequency dependent conductivity of bismuth zinc vanadate semiconducting glassy system", *J. Appl. Phys.*, Vol. 112, pp. 083701, 2012.

[23] Padmasree, K. P., Kanchan, D. K. and Kulkarni, A. R., "Impedance and modulus studies of the solid electrolyte system $20CdI_280[xAg_2O\text{-}y(0.7V_2O_5\text{-}0.3B_2O_3)]$, where $1 \leq x/y \leq 3$", *Solid State Ionics*, Vol. 177, pp. 475-482, 2006.

[24] Catalan, G., "On the link between octahedral rotayions and conductivity in the domain walls of $BiFeO_3$", *Ferroelectrics*, Vol. 433, pp. 65-73, 2012.

[25] Khander, M. S., Kambale, R. C., Patil, J. Y., Kolekar, Y. D. and Suryavanshi, S. S., "Effect of calcinations temperature on the structural and electrical properties of cobalt ferrite synthesized by combustion method", *J. Alloys. Compd.*, Vol. 509, pp. 1861-1865, 2011.

[26] Pattanayak, S., Parida, B. N., Das, P. R. and Choudhary, R. N. P., "Impedance spectroscopy of Gd doped BiFeO3 multiferroics", Appl. Phys. A, Vol. 112, pp. 387-395, 2013.

[27] Barsoukov, E. and Macdonald, J. R., *Impedance spectroscopy: Theory, experiment and applications*, John Wiley & Sons, Inc., New Jersey, 2005.

[28] Funke, K., "Jump relaxation in solid electrolytes", *Progr. Solid State Chem.*, Vol. 22, pp. 111-195, 1993.

[29] Globus, A., Duplex, P. and Guyot, M., "Determination of initial magnetization curve from crystallites size and effective anisotropy field", *IEEE trans. Magn.*, Vol. 7, pp. 617-622, 1971.

[30] Das, S. R., Choudhury, R. N. P., Bhattacharya, P., Katiyar, R. S., Dutta, P., Manivannam, A. and Seehra, M. S., " Structural and multiferroic properties of La-modified $BiFeO_3$ ceramics", *J. Appl. Phys.*, Vol. 101, pp. 034104:1-4, 2007.

[31] Ederer, C. and Spaldin, N. A., "Weak ferromagnetism and magnetoelectric coupling in bismuth ferrite", *Phys. Rev.*, Vol. B71, pp. 060401(R)-060404(R), 2005.

[32] Das, R., Khan, G. G. and Mandal, K., "Enhanced ferroelectric, magnetoelectric, and magnetic properties in Pr and Cr co-doped $BiFeO_3$ nanotubes fabricated by template assisted route", *J. Appl. Phys.*, Vol. 111, pp. 104115, 2012.

[33] Anjum, G., Kumar, R., Mollah, S., Shukla, D. K., Kumar, S. and Lee, C. G., "Structural, dielectric and magnetic properties of $La_{0.8}Bi_{0.2}Fe_{1-x}Mn_xO_3$ ($0.0 \leq x \leq 0.4$) multiferroics", *J. Appl. Phys.*, Vol. 107, pp. 103916, 2010.

[34] Muthu, S. E., Singh, S., Thiyagarajan, R., Selvan, G. K., Rao, N. V. R., Raja, M. M. and Arumugam, S., "Influence of Si substitution on the structure, magnetism, exchange bias and negative magnetoresistance in $Ni_{48}Mn_{39}Sn_{13}$ Heusler alloys", *J. Phys. D: Appl. Phys.*, Vol. 46, pp. 205001, 2013.

[35] Palkar, V.R., John, J. and Pinto, R., "Observation of saturated polarization and dielectric anomaly in magnetoelectric $BiFeO_3$ thin films", *Appl. Phys. Lett.*, Vol. 80, pp. 1628, 2002.

[36] Arya, G., Kotnala, R. K. and Negi, N. S., "A Novel Approach to Improve Properties of $BiFeO_3$ Nanomultiferroics", *J. Am. Ceram. Soc.*, Vol. 97, pp. 1475-1480, 2014.

[37] Vijayasundaram, S.V., Suresh, G., Mondal, R.A. and Kanagadurai, R., "Composition-driven enhanced magnetic properties and magnetoelectric coupling in Gd substituted $BiFeO_3$ nanoparticles", *J. Magn. Magn. Mater.*, Vol. 418, pp. 30-36, 2016.

[38] Palkar, V. R., Kundaliya, D. C. and Malik, S. K., "Magnetoelectricity at room temperature in the $Bi_{0.9-x}Tb_xLa_{0.1}FeO_3$ system", Phys. Rev. B, Vol. 69, pp. 212102(1-3), 2004.

CHAPTER 5

CONCLUSIONS

5.1 Conclusions

Polycrystalline $Bi_{1-x}Gd_xFe_{0.9}Cr_{0.1}O_3$ (where x= 0.00, 0.05, 0.10, 0.15 and 0.20) ceramics were synthesized by the solid state reaction technique and prepared samples were sintered at different temperatures (825, 850 and 875 °C). The present research work mainly deals with investigation of structural, electrical and magnetic properties of rare earth substituted polycrystalline $Bi_{1-x}Gd_xFe_{0.9}Cr_{0.1}O_3$. This chapter presents a summary on the results and discussion presented in the previous chapters and also suggestions for the scope of future work.

The X-ray diffraction result indicates that first two (in which x = 0.00 and 0.05) samples show single phase distorted rhombohedral perovskite structure and last three (in which x = 0.10, 0.15 and 0.20) samples show single phase orthorhombic perovskite structure. Some impurities were detected in the parent sample and amount of impurity gradually decreased with the addition of Gd content. For x = 0.15 and x = 0.20, there is only one impurity peak in $Bi_{1-x}Gd_xFe_{0.9}Cr_{0.1}O_3$ compositions. The theoretical density and bulk density increased with the increase in Gd content. The bulk density is found highest (when x = 0.05-0.20) for 875 °C sintering temperature (T_s). For parent sample density is found highest at T_s = 850 °C. The surface morphology of the samples was observed by Field Emission Scanning Electronic Microscope. The average grain size decreases with the increase in Gd content but increases with T_s. The average grain size is found between 0.92 – 2.07 μm. Energy Dispersive X-ray spectroscopy of the samples confirms the Gd content doping in the compositions and revels that there is no foreign materials in the samples. The variation of dielectric constant (ε′) with frequency measured at room temperature. The value of ε′ is found

to be increasing with increasing Gd content. At low frequencies higher value of ε′ is observed due to the contribution of all type of polarizations. The value of ε′ decreases with the increase in frequency and at high frequencies it is almost constant. This phenomenon can be explained by the Koops theory, based on Maxwell-Wagner model. The dielectric loss is found very low with respect to dielectric constant. Complex impedance studies implies that in some samples, only grain's contribution is dominating in the conduction mechanism and both grain's as well as grain boundaries contributions are dominating in the conduction mechanism in other samples. The electric modulus analysis suggests that the relaxation process occur in the material. The AC conductivity ($_{AC}$) increased with the increase in frequency due to the hopping of charge carriers. The $_{AC}$ also found to be increasing with the Gd content. The real part of complex permeability (μ_i') is found to be high in some samples due to spin rotation, domain wall motion and homogeneous grain growth. From the magnetization investigation it is seen that all samples show unsaturation i.e, all studied samples shows antiferromagnetic behavior at room temperature. The maximum value of ME voltage coefficient is found to be 0.196 $Vcm^{-1}Oe^{-1}$ for the sample with x = 0.20 at T_s = 875 °C. The results imply that the composition $Bi_{1-x}Gd_xFe_{0.9}Cr_{0.1}O_3$ (for x = 0.20 sintered at 875 °C) may have potential applications as multiferroic materials.

5.2 Suggestions for future work

Further studies on different aspects are possible for fundamental interest of the studied materials.

- Ferroelectric, piezoelectric and pyroelectric characterization may be studied for the samples.
- Leakage current density may be taken for proper understanding of oxygen vacancy.

● X-ray photoelectron spectroscopy studies may be carried out to measure the oxidation states of the doping elements.

● FTIR and Raman spectroscopy of the composition may be studied.

● Other preparation techniques (e.g. sol-gel, auto-combustion and co-precipitation etc.) may be used to prepare the samples for comparing the results of the present study.